Spring 2010

Sediment budget closure during runoff-generated high flow events in the South Amana sub-watershed, Ia

Kevin Daniel Denn
University of Iowa

SEDIMENT BUDGET CLOSURE DURING RUNOFF-GENERATED HIGH FLOW EVENTS IN THE SOUTH AMANA SUB-WATERSHED, IA

by

Kevin Daniel Denn

A thesis submitted in partial fulfillment
of the requirements for the
Master of Science degree in
Civil and Environmental Engineering (Hydraulics)
in the Graduate College of
The University of Iowa

May 2010

Thesis Supervisor: Professor Athanasios N. Papanicolaou

Graduate College
The University of Iowa
Iowa City, Iowa

CERTIFICATE OF APPROVAL

_____

MASTER'S THESIS

_____

This is to certify that the Master's thesis of

Kevin Daniel Denn

has been approved by the Examining Committee for the thesis requirement for the Master of Science degree in Civil and Environmental Engineering (Hydraulics) at the May 2010 graduation.

Thesis Committee: _____

Athanasios N. Papanicolaou, Thesis Supervisor

_____

A. Jacob Odgaard

_____

A. Allen Bradley

The future starts today, not tomorrow.

-Pope John Paul II

ACKNOWLEDGEMENTS

I would like to thank Dr. Thanos Papanicolaou for his extensive support and assistance in completing this project. Dr. Chris Wilson and Dr. Mohamed Elhakeem also dedicated large amounts of time to help me succeed; for this, I am grateful. I have developed as an engineer thanks in no small part to the myriad of challenges each of the aforementioned individuals presented to me. Thank also to my committee members, A. Jacob Odgaard and A. Allen Bradley. Their critique of my thesis has improved its content and clarity. I would also like to thank my family and friends. Their support during my time at the University of Iowa has been invaluable. Last, but certainly not least, I would like to express thanks to God for the gifts and abilities He has provided. I realize everything that I have achieved is because of Him and His grace; without Him, I would be nothing.

TABLE OF CONTENTS

LIST OF TABLES

LIST OF FIGURES

LIST OF NOMENCLATURE

A	Einstein approach coefficient
a	power trend line coefficient
AR	cross-sectional area
A_{sm}	SediMeter calibration coefficient
B_A	background activity
B_C	bank contribution
B_R	branching ratio
B_{sm}	SediMeter calibration coefficient
C	emission rate
CB_C	channel bed contribution
CN	runoff curve number
C_S	suspended sediment concentration
C_{sm}	SediMeter calibration coefficient
D	atmospheric radionuclide influx
d	soil grain diameter
d_{50}	soil grain diameter for which 50 percent of the material is finer
d_{65}	soil grain diameter for which 65 percent of the material is finer
D_{sm}	SediMeter calibration coefficient
E	efficiency
e_A	activity error
e_B	background error
e_C	emission rate error

e_F correction error

F Einstein approach variable

FBU formazin backscatter units

F_C self-absorption correction factor

g gravitational acceleration

H flow depth

I unattenuated photon emission through an empty sample container

I_1 Einstein approach variable

I_2 Einstein approach variable

K_{sm} SediMeter calibration coefficient

L stream reach length

L_a active layer depth

m sample mass

M_M mixture mass

M_S sediment mass

P precipitation depth

q power trend line coefficient

q_b bed load discharge per unit width

Q_S total sediment flux through the study reach outlet

$Q_{S,i}$ flux of sediment into the study reach from the i^{th} sub-watershed

Q_W water flow rate

R_A radionuclide activity

R_D runoff depth

RAW	SediMeter measurement after internal reflections and background light correction
S	storage parameter
SG_S	sediment specific gravity
T	attenuated photon emission through an empty sample container
t	time
T_b	turbidity of solution used to determine K_{sm}
U*	shear velocity
U_{adj}	adjusted voltage
U_{amb}	voltage added by ambient light
U_C	upland contribution
U_{dark}	value of voltage returned to sensor in darkness
U_F	particle fall velocity
U_{off}	SediMeter measurement when NIR is not emitted
U_{on}	SediMeter measurement when NIR is emitted
V_{bank}	bank material volume
V_M	mixture volume
X	logarithmic velocity distribution correction factor
z*	Einstein approach variable
z_f	arbitrary flow depth
γ_s	soil unit weight
Δ	Einstein approach variable
η	Einstein approach coefficient
κ	von Karman constant

λ	decay rate
μ	water viscosity
v	kinematic viscosity of water
ρ_s	soil density
ρ_w	water density
τ^*	Shields stress

CHAPTER 1 INTRODUCTION

1.1 Study Rationale

Soil erosion has annually been estimated to cause over $44 billion in damages to highway infrastructure and agricultural fields in the United States (Pimentel et al. 1995). In conjunction, the United States Department of Agriculture - Natural Resources Conservation Service, NRCS, has estimated that Iowa loses 128.6 million tons of highly productive top soil per year due to erosion triggered by precipitation, runoff, and intense agriculture activities (2003).

However, implementation of certain land management practices (known interchangeably as conservation practices) can reduce erosion in upland hills and floodplains (referred together hereafter as uplands) and its harmful effects on water quality and ecosystem health. For example, grassed water ways have been found to effectively reduce runoff/sediment conveyance and gully formation by slowing water flow, increasing infiltration rates, and maintaining dense grass roots that hold soil particles in place (Al-Kaisi and Yin 2003; Bracmort et al. 2004; Fiener and Auerswald 2006). Furthermore, Abaci and Papanicolaou (2009) have shown that selection of suitable management practices can reduce soil erosion by over 400% relative to other practices.

Developing sound management strategies to reduce soil loss requires an understanding of soil particle movement within a watershed and the delivery mechanisms involved in the transfer of soil from the landscape to the stream. Evaluating watershed erosion processes begins in the uplands where soil is mobilized by rainfall-generated runoff. However, a large proportion of the mobilized sediment does not leave the field in

a single runoff event (Ghadiri et al. 2001). The sediment deposits along the flow paths when the runoff transport capacity is exceeded (Huang et al. 1999) and is stored on toe slopes, floodplains, or bars until another runoff event remobilizes it. Thus, eroded soil particles move through the landscape in a complex series of steps, whose temporal and spatial characteristics are not well known (Bonniwell et al. 1999).

Once upland sediment reaches the stream, it is transported either in suspension or carried along the streambed through bed load or saltation. Additional sediments are either entrained in the flow through mining of the stream bed (i.e., pick up and resuspension) or washed from the bank toes particle-by-particle (i.e., fluvial erosion). Fluvial erosion eventually leads to slumping and collapse of stream banks, adding even more sediment to the mixture moving downstream (Papanicolaou et al. 2007). However, just as in the uplands, sediment is deposited as flow decreases, allowing coarser particles to settle and transport capacities to decrease (Huang et al. 1999). The transit times and travel distances of the entrained sediment are site- and event-specific, making sediment flux prediction difficult.

1.2 Critical Literature Review

1.2.1 Sediment Budgets in a Watershed

Numerous studies have been completed in an attempt to predict the fluxes of sediment from a watershed more accurately. The methods used by researchers to quantify the contributions from different source areas to a stream segment vary but generally result in an overarching budget of sediment fluxes. Some studies have simply determined the net sediment flux from the entire watershed with a “black box” approach, i.e., without examining the source areas of sediment (Allmendinger et al. 2007; Visser et

al. 2007). Other studies have divided the focus area into subwatersheds and measured the inputs from each subwatershed through intense monitoring (Stubblefield et al. 2009). In these studies, the following simple expression was used to essentially "close" the sediment budget averaged over multiple events within a watershed:

$$Q_S = \sum_{i=1}^{n} Q_{S,i} \qquad 1.1$$

where Q_S is the total sediment flux through the study reach outlet and $Q_{S,i}$ is the flux of sediment into the study reach from the number of sub-watersheds (n) in the study area.

The above expression can be useful in quantification of an overall sediment budget; however, it is limited in differentiating contributions from multiple source areas (i.e., uplands, stream banks, channel bed). Specifically, the approach described above cannot explicitly distinguish the contributions of the upland to the total sediment load in the stream. Determining upland contributions is difficult because they can vary in space and time, especially in intense agricultural watersheds (Soulsby et al. 2003; Walling et al. 2002). Identifying the areas where significant sediment production occurs is vital to help watershed managers maximize their resources to achieve their site-specific goals in terms of sediment reduction and non-point source pollution (Mabit et al. 1999; Nyssen et al. 2009; Wasson et al. 2002).

Another limitation to the budget approach identified in Equation 1.1 is that the budgets are often determined over extended periods, which average both runoff events and low flow conditions. Most of the existing approaches do not provide event based estimates of sediment budgets and fall short in isolating the events that contribute the most to sediment delivery. Available but sparse field data reveal that the majority of sediment delivery in a year occurs during a relatively few number of high magnitude

events. For example, Markus and Demissie (2006) have recently reported that the four largest events transported 68% of the total load for the year; Lenzi et al. (2003) reported that *two events* transported 38% of the total load for a *16-year period*.

Only a few sediment budgets have been completed focusing on these intense events (Alexandrov et al. 2007; Gray and Gartner 2009; Lenzi and Marchi 2000; Ortega and Heydt 2009) due to their inherent rareness. Nonetheless, closing the sediment budget during these intense events is of paramount importance for quantifying the contributions of different sources within a watershed and for gaining a better understanding of the interaction between flow and sediment (Collins et al. 1998; Papanicolaou et al. 2003; Valero-Garces et al. 1999; Vanden Bygaart and Protz 2001; Walling and Amos 1999).

1.2.2 Transport Mode of Sediment

During almost all events the dominant mode of transport for the finer fraction (particles with diameters less than 63 μm) of the total available sediment is suspension (Baca 2008; Lefrancois et al. 2007; Lenzi et al. 2003; Mano et al. 2009; Salant et al. 2008; Smith et al. 2003; Steegen et al. 2000). In most sediment budget approaches, suspended sediment transport has traditionally been quantified using a sediment rating curve. A sediment rating curve assumes a power-law relationship between suspended sediment concentration (C_S) and water flow (Q_W) rates. However, the relationship between C_S and Q_W is not as straightforward as the power-law relationship implies. During an event, the largest suspended sediment concentration does not always occur at the peak of a hydrograph due to the non-linear relation between flow and sediment and dominant sediment source availability, which collectively lead to the phenomenon of hysteresis (i.e., the lagging of an effect behind its cause) between sediment and flow

(Klein 1984). Williams (1989), among others, outlined three primary classes of the C_S versus Q_W relationship, along with their potential causes (Table 1.1). For example, a clockwise hysteresis is considered to occur when sediment is derived from the bed and banks of the channel or areas adjacent to the channel, whereas a count-clockwise hysteresis occurs when the upper part of the slopes is the sediment source area. These relationships can be visualized by plotting C_S versus Q_W and then connecting the points chronologically (an example of such a relationship is displayed in Figure 1.1). Numerous previous studies (e.g., Ahanger et al. 2008; Alexandrov et al. 2007; Baca 2008; Doomen et al. 2008; Smith and Dragovich 2009) have identified the relationships outlined by Williams (1989). Because of the complex C_S and Q_W relationship, a power-law relationship is not an adequate tool with which to estimate sediment budgets when inter- and intra-event data of different magnitudes are limited. Analysis of the flow-sediment hysteresis may assist in determining event-based sediment budgets more accurately. However, the utility of the hysteresis in sediment budget approaches has not been fully explored due to limited inter- and intra-event data of different magnitudes.

To account for the complicated C_S versus Q_W relationship and increase the accuracy of sediment flux predictions, suspended sediment data must be collected more frequently with increased spatial density (Gray 2003). Currently, capturing suspended sediment data for high flow events often requires user interaction throughout the event, which is costly and often times dangerous. The level of increase in funding and labor required to meet the aforementioned need is not feasible; thus, a new sensor with the ability to collect automated suspended sediment data while minimizing user interaction is required. Durable automated sensors (e.g., infrared sensors) can provide, with some

limitations, unique insight for the C_S versus Q_W relationship without endangering sampling crews. However, even if continuous suspended sediment data are collected successfully, the C_S versus Q_W measurements must be accompanied with sediment tracing techniques to conclusively differentiate the sources of the transported sediment.

1.2.3 Limitations of Sediment Budget Approaches

In summary, the critical review in Sections 1.2.1 and 1.2.2 reveals that sediment budget approaches are plagued by several significant problems: i) a lack of knowledge regarding sediment budget partitioning that can distinguish source contributions and indicate the correct remedial actions, ii) in most approaches sediment budgets are averaged over an extended period of time, limiting our ability to determine the critical events contributing the most to sediment, iii) a lack of data between discharge and sediment concentrations for high magnitude events, iv) the inability to account for hysteresis in sediment budget approaches due to limited inter- and intra-event data of different magnitudes, and v) the limited availability of durable "smart" automated samplers that record data at near continuous intervals in digital form before transferring it remotely to the user.

1.3 Future Directions

Future research and sediment monitoring programs must the key limitations outlined in Section 1.2.3. In this study, we will focus on identifying sediment sources to the suspended load of individual runoff events within a representative agricultural watershed. We will do that by coupling sediment budget approaches (discussed in Section 1.2) with state-of-the-art tracing techniques, while collecting high-frequency, event-based suspended sediment data with the use of automated samplers.

Over the last decade, much emphasis has been placed on the development of a smart sensor network that can facilitate high-frequency and spatially dense measurements [e.g., the WATer Environmental Research Systems (WATERS) Network]. While this emphasis on sensor technology is addressing some of the knowledge gaps identified in Section 1.2, few studies have focused on sediment source partitioning.

A key component of source partitioning is the availability of conservative tracers to track sediment from its source to the watershed outlet. Some of the most notable tracer methods incorporate the use of elemental ratios (Fox and Papanicolaou 2008; Leithold and Blair 2001; Papanicolaou et al. 2003), rare earth elements (Polyakov et al. 2004), radionuclides (Martz and Dejong 1991; Walling et al. 2002; Wasson et al. 2002), heavy metals (van der Perk and Jetten 2006), and infrared spectroscopy (Poulenard et al. 2009). These tracers have provided valuable information regarding sediment provenance over longer periods (e.g., several hydrologic cycles or during crop rotations) but they have limited uses for identifying the origin of mobilized sediments solely associated with a single event.

One particular method has been developed to address specifically sediment mobilized during a single event (Blake et al. 2002; Bonniwell et al. 1999; Matisoff et al. 2002; Wallbrink and Murray 1996; Wilson et al. 2008). This powerful tracing method utilizes two naturally occurring radionuclides: Beryllium-7 (^{7}Be), which has a half-life of 53 days, and excess Lead-210 ($^{210}Pb_{xs}$), which has a half-life of 22 years. ^{7}Be is produced in the atmosphere through the cosmic ray spallation of nitrogen and oxygen nuclei. ^{210}Pb is produced as a daughter-product of the Uranium-238 (^{238}U, $t_{1/2}=4.46 \times 10^{9}$ years) decay series. ^{238}U decays through a series of daughters to produce the short-lived, gaseous

Radon-222 (^{222}Rn, $t_{1/2}$=3.8 days). A portion of the ^{222}Rn diffuses out of the soil into the atmosphere while the remainder of the ^{222}Rn remains in the soil. In both cases, the ^{222}Rn decays to ^{210}Pb. The ^{210}Pb in the atmosphere is termed as excess and denoted as $^{210}Pb_{xs}$. Both ^{7}Be and $^{210}Pb_{xs}$ attach to aerosol particles in the atmosphere and are delivered to the landscape primarily during precipitation events (Todd et al. 1989), where they quickly and strongly adsorb to surficial soils (Olsen et al. 1986).

Because ^{7}Be has a relatively short half-life of only 53 days, it has a short residence time in the soil column before decaying to indistinguishable levels. Thus, a strong relationship exists between a single erosion event and high activities of ^{7}Be in the eroded surficial soils (e.g., sediments derived from uplands). Additionally, ^{7}Be signatures are normalized by $^{210}Pb_{xs}$ because of their similar delivery patterns, thus accounting for spatially variable delivery within the precipitation.

Concentrations of both radionuclides are highest at the surface of a soil profile and decrease exponentially with depth (Wallbrink and Murray 1996). ^{7}Be is limited to the top few centimeters in the soil profile due to the strong bonding with surface soils and the short 53-day half-life; conversely, $^{210}Pb_{xs}$ extends deeper in the profile because it does not readily decay before migrating downward or is mixed by bioturbation and tillage (Blake et al. 1999; Bonniwell et al. 1999; Wallbrink et al. 1999).

These vertical distributions of ^{7}Be and $^{210}Pb_{xs}$ are integral in differentiation of upland and channel source sediments when related to the differing modes of erosion within each source area. The limited erosion depth resulting from rainsplash, interrill, and rill erosion processes in the uplands ensures that eroded soils will have relatively high radionuclide activities (Kuhnle et al. 2008; Wilson et al. 2008). Conversely, channel

bank sediments have relatively low activities (Kuhnle et al. 2008; Wilson et al. 2008) because during bank collapse, any high activity soils at the bank surface will be diluted by a much larger volume of low-activity subsurface soils. Additionally, steep banks have limited exposure to precipitation (and the associated radionuclides), minimizing the activity of fluvially-eroded bank sediments. Channel bed material contributed to the suspended load likely will have been in residence of the bed for an extended period, allowing for extensive radionuclide decay (Kuhnle et al. 2008; Wilson et al. 2008). Additionally, particles eroded from a channel bed comprised of sand-sized (or larger) particles will have minimal radionuclide activity due to the low probability of radionuclide attachment to these particles (He and Walling 1996).

Figure 1.2 provides a generalization of the activities of suspended sediment sources. The relative proportions of ^{7}Be and $^{210}Pb_{xs}$ contributed from each of the sources are denoted by the font size (larger font = higher radionuclide activity). Suspended sediment is a mixture of material originating from the sources. Thus, the suspended sediment activity will be the weighted average of the source activities, based on the amount of material contributed from each source (upland and channel). This unique radionuclide tracing method has been proven in a limited number of previous studies to have the ability to differentiate upland sediments from channel (bank and bed) sediments (e.g., Kuhnle et al. 2008; Wilson et al. 2008).

The description of the partitioning of sources in Figure 1.2 can be mathematically expressed by the following equation:

$$C_s = \int U_C + \int B_C + \int CB_C \qquad 1.2$$

where U_C denotes the sediment contribution from upland areas, B_C is the sediment contribution from the channel banks, and CB_C is the sediment contribution from the channel bed. The subscript c in the terms of Equation 1.2 implies contribution.

The differences between Equation 1.2 and the much more commonly used Equation 1.1 are significant. **Equation 1.1** uses a simple "black-box" approach in which the **net flux** of material through a watershed outlet is the only consideration. While knowledge of the net flux is important, a key component is missing from Equation 1.1: it does not identify sediment provenance. However, solving **Equation 1.2** can quantify **source-specific fluxes.** Source identification is a key component in assisting watershed managers in the development and employment of effective land management practices.

1.4 Summary

The development of land management strategies by watershed managers is complicated to varying degrees by a lack of multiple key pieces of information. Previous sediment budget studies have been completed in an attempt to address the knowledge deficiency. However, these studies have been unable to address the knowledge gaps fully, in part due to the lack of source identification at an event-based time scale. Furthermore, the accurate quantification of sediment from these sources during critical high-magnitude events has been hindered due to the inability to develop statistically significant relationships between discharge and sediment concentrations resulting from the hysteresis phenomenon and the limited availability of "smart" samplers.

To meet these challenges, future sediment budget studies must utilize event-based sediment tracing techniques (e.g., the coupling of ^{7}Be and $^{210}Pb_{xs}$) in parallel with smart sensor networks. Successful implementation will allow watershed managers to

understand better the erosional processes in their watershed. This, in turn, will facilitate the maximization of oftentimes limited resources to minimize the costly effects of erosion.

Table 1.1. Suspended sediment concentration versus flow rate classifications

Class	C_S-Q_W Relationship	Potential Cause
I	Single-valued line	Uninterrupted sediment supply from source(s)
II	Clockwise loop	Source exhaustion, bed paving
III	Counter-clockwise loop	High source soil erodibility in conjunction with prolonged erosion, seasonal variability

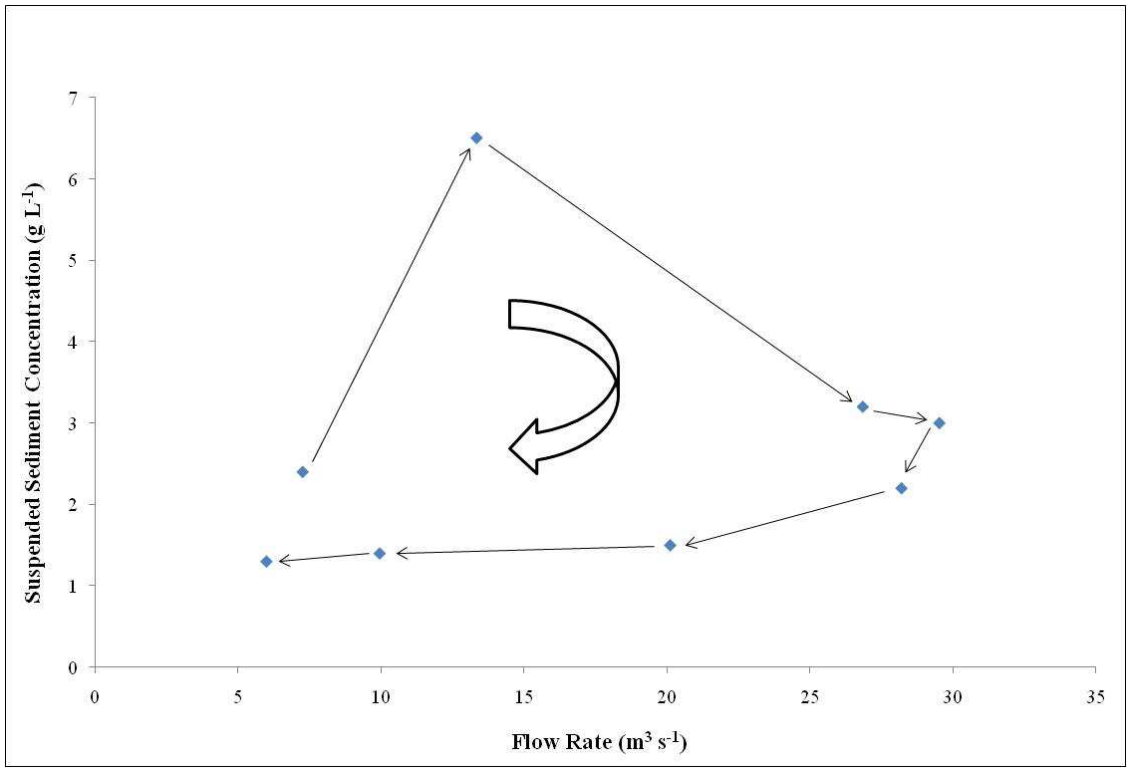

Figure 1.1. Example of C_S-Q_W relationship

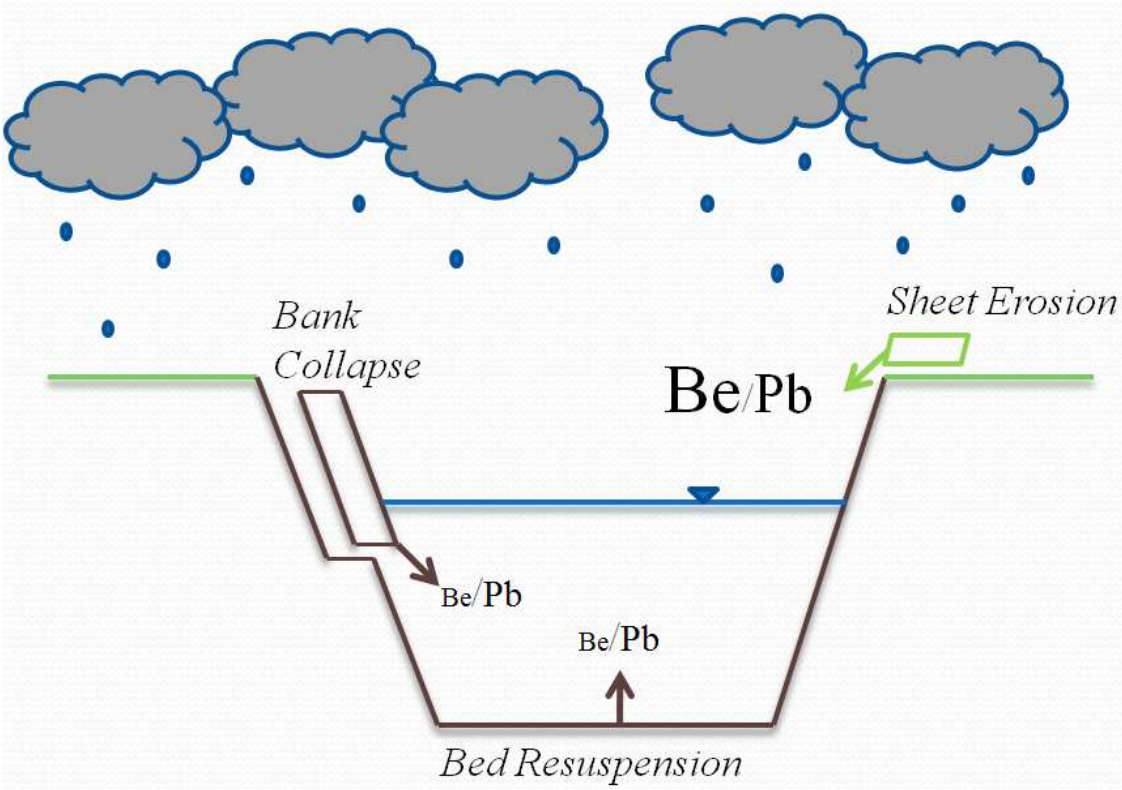

Figure 1.2. Suspended sediment contribution processes, after Wilson and Kuhnle (2006)

CHAPTER 2 OBJECTIVES

The primary objective of this study is to close the sediment budgets within a small agriculture watershed, the South Amana Sub-Watershed (SASW) in Iowa, during different magnitude events occurring on June 16, 18, and 19, 2009. Past research at the site (Abaci and Papanicolaou 2009) has shown that the May and June events are the critical events for sediment mobilization. Contemporary sediment budget closure requires the quantification of suspended sediment flux at the outlet and the identification of suspended sediment provenance. Flow and complementary suspended sediment data collected with traditional and "smart" instrumentation that had been installed at the SASW outlet will be combined with laboratory sediment analysis to undertake the following specific sub-objectives: 1) examine the relationship between flow and suspended sediment concentration to distinguish trends including hysteresis; 2) identify provenance of the collected suspended sediment with a sediment tracing study; this tracing study will utilize the naturally derived radionuclides ^{7}Be and $^{210}Pb_{xs}$ to determine suspended sediment provenance; 3) close the sediment budget for the June events by utilizing the results of the field and tracer studies; these results will be qualitatively compared against a simulated sediment budget.

CHAPTER 3 SITE DESCRIPTION

3.1 South Amana Subwatershed

The 260-km^2 Clear Creek Watershed (CCW) is a Hydrologic Unit Code-10 watershed in southeastern Iowa (Figure 3.1). Anthropogenic activities, including intensive agriculture and urbanization, have strongly influenced flow and sediment processes within the watershed. The current land cover in the watershed is 60% row crops (i.e., corn-soybean rotations), 27% grasslands, 8% forests, and 5% urban areas. The intensive agriculture, in conjunction with highly erodible soils and steep slopes, has produced some of the highest rates of erosion and non-point source pollution in the state of Iowa. According to the Natural Resources Conservation Service (NRCS) 2003 National Resources Inventory, Iowa has the second highest average annual erosion rate in the United States. Stream destabilization as a result of widespread channelization and drainage system construction has further increased sediment loadings to the stream (Rayburn and Schulte 2006). This has exacerbated damage resulting from recent system-impacting floods, prompting concern among local residents.

The current study focuses in the headwaters of the CCW, namely the South Amana Sub-Watershed (SASW; Figure 3.2). The SASW has an area of 26 km^2 and is dominated by agricultural practices, with 85% of the land supporting corn/soybean fields and the remaining 15% under grassed pastures. Hillslopes in the SASW have an average gradient of 4% (range = 1% to 10%) and contain silty clay loams of the Tama-Downs soil series. Average annual erosion rates are approximately 11 Mt ha^{-1} yr^{-1} (Abaci and Papanicolaou 2009). Most of this erosion occurs during the early summer months when

high-intensity rainfalls impact bare soil surfaces in the newly planted agricultural fields (Figure 3.3).

The SASW stream network consists of two 1st-order streams with lengths of approximately 6 river km and slopes of 0.16%. The floodplain and channel bank soils consist of the poorly drained Colo and Ely soil series. The bed of Clear Creek is dominated by sand-sized particles having a median size of 0.31 mm (Ellis 2009). The banks of Clear Creek in the SASW range from gradually sloping with a 0.5 m height in the headwaters to nearly vertical with a 3 m height at the outlet.

The outlet of the SASW was defined as a 76-m straight reach of Clear Creek downstream of the 190th Street bridge (see inset picture on Figure 3.2). The entire reach was surveyed regularly to determine changes in the channel morphology. The average water discharge and sediment loading is 5.9 x 10^6 m^3 yr^{-1} and 5.0 x 10^3 tons yr^{-1}, respectively (Abaci and Papanicolaou 2009).

3.2 Climate

The general climate of the CCW is typical of other mid-continental locations: hot summers, cold winters, and wet springs are the prevailing trends (Ruhe 1956). Summer months are influenced by warm, humid air masses from the Gulf of Mexico. Winter months are influenced by dry Canadian air. The average daily temperature is approximately 10 °C, the average July maximum is roughly 29 °C, and the average January minimum is about -13 °C. An average growing season in southeast Iowa lasts approximately 180 days. Average annual precipitation is 889 ± 220 mm yr^{-1} with convective thunderstorms prominent in the summer and snowfall in the winter.

This study focused on a specific series of rain events in mid June 2009. Total precipitation (water equivalent snowfall + rain) during the winter months prior to the study period (November 2008 to February 2009) was 156 mm, which was near the annual average of 144 mm. Total precipitation during the three months prior to the study period (March 2009 to May 2009) was 309 mm, which was above the annual average of 257 mm. This above average precipitation led to relatively higher soil moisture levels in the region.

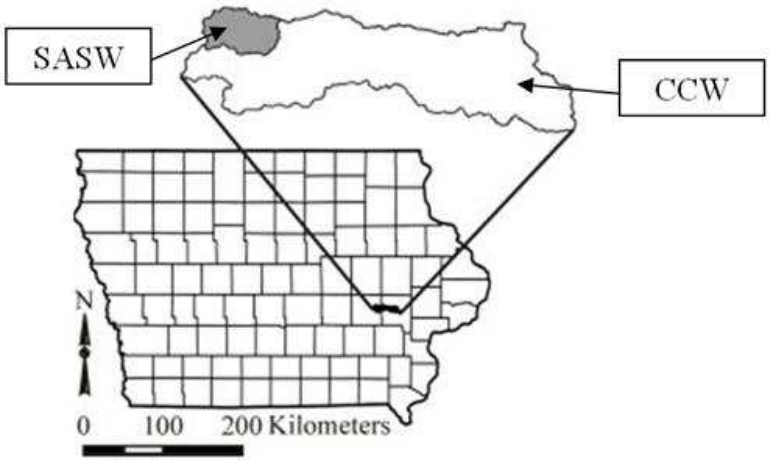

Figure 3.1. Location of the SASW in the CCW (Abaci and Papanicolaou 2009)

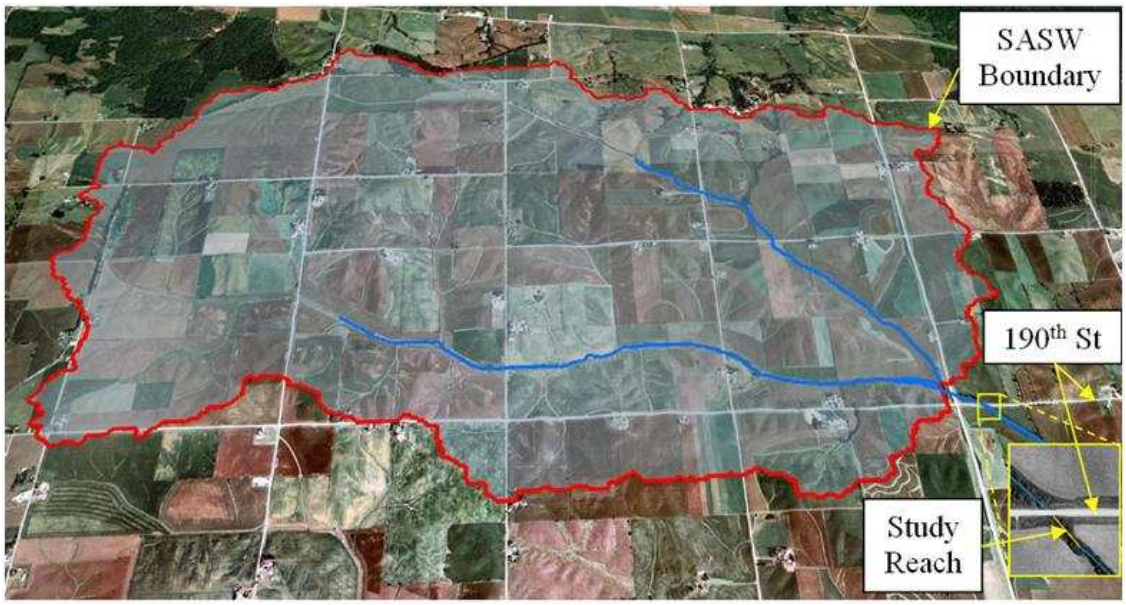

Figure 3.2. Aerial view of the SASW

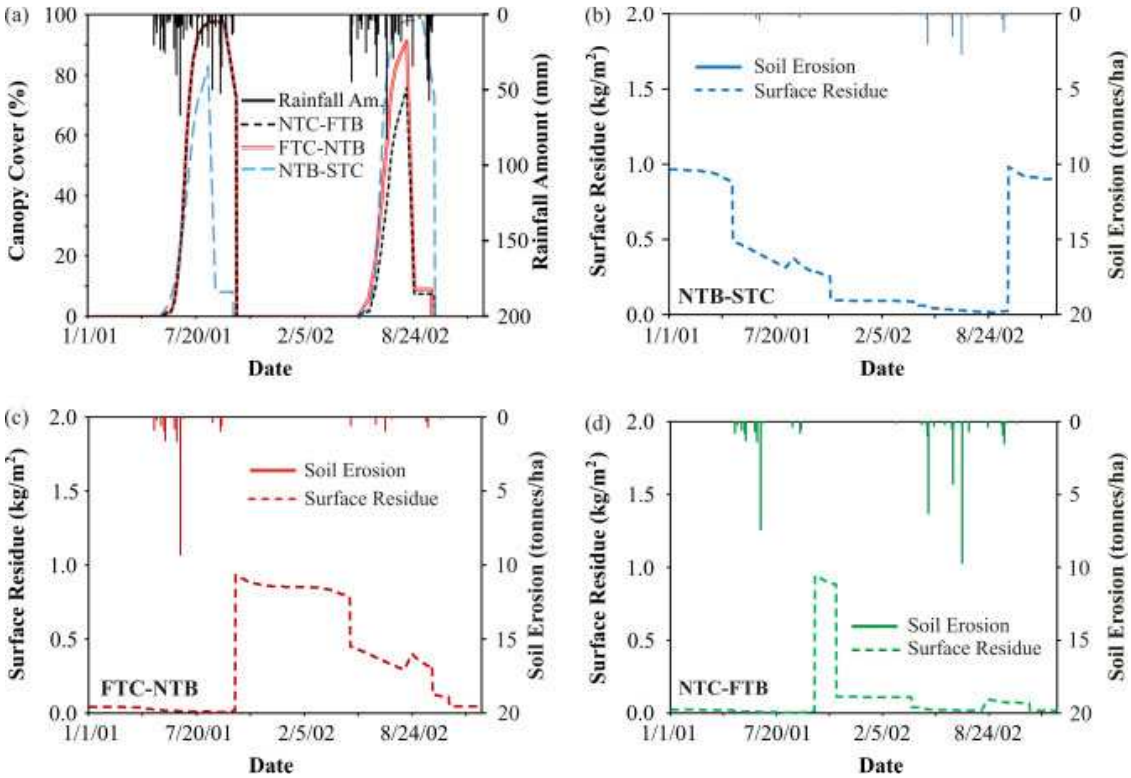

Figure 3.3. Daily variation of canopy cover, rainfall amount, surface residue, and soil erosion during a 2 years crop rotation period [courtesy of Abaci and Papanicolaou (2009)]

CHAPTER 4 METHODOLOGY

4.1 Introduction

The primary objective of this study was to close the sediment budgets for the events of June 2009 in the South Amana Sub-Watershed (SASW) of Clear Creek, Iowa. Volumetric stream flow (Q_W), which is partly a function of the delivered precipitation to the watershed, and the suspended sediment concentration (C_S) were measured during the events to determine the sediment fluxes. The sampling methods for these variables are presented herein.

The upland (U_C), channel bank (B_C), and channel bed (CB_C) contributions to the suspended load were differentiated using a two end member unmixing model that incorporates the activities of ^{7}Be and $^{210}Pb_{xs}$ for the upland surface soils, as well as the channel bank and bed sediments. The methods below also address each of these components individually.

4.1.1 Runoff Generation

The primary factors controlling runoff in small agricultural watersheds are precipitation and antecedent soil moisture. For this study, precipitation measurements were obtained from a wireless, dual tipping bucket, rain-monitoring station located near the center of the SASW. The tipping bucket rain gauge is an effective and reliable tool for capturing direct “point measurements” of rainfall. The device consisted of two tipping buckets. The second tipping bucket provided increased reliability for valid measurements and identified possible failure situations (Ciach 2003). The dual tipping bucket rain gauge platform remotely sent real-time data to a server maintained by the

University of Iowa. Each tip was equal to 0.254 mm of rainfall and the cumulative rainfall data were available in 5-minute, 15-minute, 60-minute, and 24-hour intervals.

Soil moisture measurements were obtained using an ECH_20 dielectric aquameter made by Decagon Devices, Inc. The probe measures the dielectric permittivity, which is directly related to the water content, of the surrounding soil. The accuracy of the probe was listed as ± 3% by the manufacturer. Probes were installed at four locations bordering the study reach. The soil moisture contents presented in this thesis are the average of the four values. The probes recorded the soil moisture in 5-minute intervals.

Runoff depths were determined using the Soil Conservation Method (Soil Conservation Service 1972). The equation used to determine the depth of runoff (R_D)

$$R_D = \frac{(P-0.2S)^2}{(P+0.8S)} \qquad 4.1$$

where P is the depth of precipitation and S is the storage parameter and is defined by Equation 4.2:

$$S = \frac{25400}{CN} - 254 \qquad 4.2$$

where CN is the runoff curve number, which is a function of land use, soil type, and antecedent soil moisture.

4.1.2 Stream Flow (Q_W)

The volumetric flow rate was determined using a stage-discharge relationship developed by Abaci and Papanicolaou (2009) for the SASW outlet (Figure 4.1). The rating curve was developed using established U.S. Geological Survey methods (Kennedy 1984) at the end of the straight 76-m outlet reach, which was well downstream of the bridge constriction.

For this study, the stage was measured at 15-minute intervals using a Submersible Global Water WL16 Water Level Logger. The logger consists of a vented pressure transducer and an enclosed data logger. The pressure transducer was installed within a stilling well (Figure 4.2) to minimize the effects of waves and water current on the measurements (Abaci and Papanicolaou 2009). The pressure transducer has a ±0.2% accuracy over the 1.4 to 21.1 °C temperature range (Global Water Instrumentation 2009).

4.1.3 Suspended Sediment Concentrations (C_S)

Suspended sediment concentrations (C_S) were determined using multiple methods, which included discrete sampling and continuous monitoring. These methods were used to monitor the sediment flux during the sampled events in order to quantify the sediment budgets.

Discrete samples of suspended sediment were collected from grab sampling. Buckets were lowered into the center of the flow from the 190th Street Bridge, which is at the beginning of the outlet reach. The 20-L buckets were filled with the water and wash load, pulled back up to the bridge, and capped for transport back to the University of Iowa. Grab samples were collected only during runoff events.

Discrete suspended sediment samples were also collected at defined intervals using automated Hach Sigma 900 MAX Portable Samplers. The Sigma sampler is a stand-alone unit in a molded plastic outer case (Figure 4.3) that consists of a computer, pumping unit, and 24 1000-mL collection bottles that are positioned under a rotating nozzle. Sampling tubes extend from the Sigmas, which are positioned atop the channel banks, to inlet nozzles located in the flow.

Water and suspended sediment samples were collected at user-defined intervals by pumping water through the inlet to the bottles in the Sigma housing. For this study, the Sigmas were programmed to collect 800-mL samples daily during baseflow conditions and hourly during runoff events. These sampling intervals were recommended by Edwards and Glysson (1999).

Four Sigma samplers were installed at the outlet reach for this study. Two Sigmas were installed immediately downstream of the 190th Street bridge atop of the western bank. Inlet tubes for both of the Sigmas were oriented in the downstream direction and attached to a metal post driven into the stream bed. The inlet tube for one of the samplers was installed 10 cm above the stream bed to ensure that this inlet was constantly submerged. The inlet tube for the other sampler was installed 70 cm above the stream bed to capture samples during high flow events. The two remaining Sigmas were installed at the pre-defined outlet of the SASW atop the western bank. The inlet tubes for these Sigmas were installed in the same manner as the upstream Sigmas. The suspended sediment concentrations reported in this thesis are the average values of the four samplers for each time interval.

The suspended sediment concentrations (C_S) were determined for the grab and Sigma samples in the University of Iowa Sediment Laboratory using the following equation:

$$C_S = \frac{M_S}{V_M} \qquad 4.3$$

where M_S is the dried sediment mass and V_M is the sample volume. Initially, the combined weight of the water/sediment mixture was recorded upon arrival at the laboratory. One hundred thirty mL of aluminum sulfate in a 30.22 mg L^{-1} solution was

then added to the mixture to facilitate flocculation and settling of the suspended particles. The mixture was dewatered first by siphoning the overlying water and then by oven drying at 60 °C until only sediment remained. The mass of the dried sample, M_S, was recorded. The sample volume was determined using the following equation:

$$V_M = \frac{M_M - M_S}{\rho_w} + \frac{M_S}{SG_S * \rho_w} \qquad 4.4$$

where M_M is the mixture mass, ρ_w is water density, and SG_S is the sediment specific gravity.

Continuous suspended sediment measurements concentrations were determined via optical backscatter measurements at 15-minute intervals using a Lindorm SediMeter (Figure 4.4). The SediMeter consists of 36 sensors, spaced at 10-mm intervals, along a vertical rod (Figure 4.5). The 510-mm long rod is protected by a clear acrylic tube. The bottom of the tube is threaded, which allows for the securing of the SediMeter to an anchor installed in the stream bed (Figure 4.6).

The optical backscatterance technique works in the following manner. The SediMeter emits a pulse of near infrared light from each of the 36 sensors into the flow. Each pulse is emitted milliseconds apart instead of simultaneously to ensure light emitted from one sensor is not recorded by another sensor. The light is reflected back to each sensor by sediment particles in suspension. Higher reflectance indicates higher turbidity, which can be related to suspended sediment concentrations (Pruitt 2003). The accuracy of this measurement technique, as defined by the SediMeter manufacturer, is ± 0.8 g L^{-1} (Lindorm 2009b). Most of the inaccuracy stems from reflections created by the beam of near-infrared light passing through the protective acrylic tubing.

The SediMeter was calibrated using the guidelines set forth in the SediMeter user manual (Lindorm 2009b) to convert the reflectance units (i.e., turbidity) into concentration values. Calibration of the SediMeter is a two-step process, which involves i) determining the appropriate coefficients to convert the reflectance (in volts) to a turbidity value (Formazin Backscatter Units, FBU) and ii) converting turbidity to suspended sediment concentrations. The SediMeter calibration process is detailed in Appendix A.

Suspended sediment concentrations were calculated for each of the 36 sensors; however, the suspended sediment concentrations reported in this thesis are the median values of the 36 measurements for each interval. The median value is reported because it is not influenced by outliers and is recommended by the SediMeter manufacturer.

4.2 Sediment Sources: Upland (U_C), Channel Bank (B_C) and Channel Bed (CB_C)

The sediment contributions from the uplands (U_C), channel banks (B_C), and channel bed (CB_C) were determined using the methods established in Wilson et al. (2008). The method uses activities of the naturally produced radionuclides, $^{210}Pb_{xs}$ and ^{7}Be, as tracers. Radionuclide activities were determined for samples of upland soils and channel bank/bed sediment (i.e., source sediments), as well as precipitation and suspended sediment collected from the SASW.

Collection of the source samples (upland soils and channel sediments) as close to the runoff event as possible is important for ensuring a strong relationship between source samples and the eroded material captured during runoff events. This is due to the relatively short half-life of ^{7}Be, 53 days. The existing ^{7}Be will decay to undistinguishable

levels as time increases between collection of the source samples and the suspended sediment sampling during the next sufficient runoff event. Moreover, minor runoff events and biomixing can redistribute the radionuclide profile.

4.2.1 Source Sediment Sampling

For this study, upland samples were collected on June 11, 2009 and channel samples were collected on June 15, 2009 with all sampled runoff occurring within the following week. Thus, a strong relationship between collected suspended sediment material and the source materials was maintained.

The upland samples were collected from four representative agricultural fields in the SASW (Figure 4.7). In each field, sampling was conducted at three locations along a downslope transect: the shoulder, back slope, and toe. At each of the 12 locations, high-resolution soil profiles were used to establish the distribution of ^{7}Be and $^{210}Pb_{xs}$ in the soil column, per the technique outlined in Wilson et al. (2003).

A three-sided frame (Figure 4.8) that samples a surficial area of $232 \cdot 8$ cm^2 was driven into the open face of a 1-m^3 soil pit. The sampler was then extracted from the pit and the extraneous soil was carefully removed until a block of soil was enclosed within the sample frame (Figure 4.9). A blade was inserted into a series of equally spaced notches at 0.5-cm intervals on the sides of the sample frame to a total depth of 3 cm. A sampling depth of 3 cm is sufficient because of the limited penetration of radionuclides (Blake et al. 1999; Bonniwell et al. 1999; Wallbrink et al. 1999). A uniform volume of 116.4 cm^3 was collected for each sampled interval.

Bank samples were collected on June 15, 2009 from the study reach near the outlet. Deeper cores from stream banks are required because bank failures remove larger

volumes of sediment. The large volume of sediment contributed to the suspended load during bank collapse also eliminates the need for the fine resolution and large surface areas necessitated by the surficial samples (Wilson and Kuhnle 2006). Thus, vertical cores of approximately 1-m length and a surface area of 5.07 cm^2 were deemed sufficient. The cores were extracted in 33-cm intervals; however, the three intervals were pooled prior to analysis. Samples were collected from three locations on the western bank of the study reach. The cores were collected approximately 40 m apart (Figure 4.7).

The Clear Creek bed is comprised primarily of sand-sized particles (Ellis 2009). Samples for radionuclide analysis were not collected from the Clear Creek bed due to the low probability of radionuclide attachment to these particles (He and Walling 1996).

4.2.2 Precipitation Sampling

Atmospheric influxes of the radionuclides used as tracers in this study (^{7}Be and $^{210}Pb_{xs}$) were collected in three 20-L buckets with an opening of 630 cm^2 at sites near the soil sampling locations. Prior to installation, each 20-L bucket was rinsed with 10% hydrochloric acid (HCl) to remove any adsorbed radionuclides (Olsen et al. 1986). The precipitation sampling sites were established immediately following the source sampling. Buckets were exchanged after each runoff event.

4.2.3 Suspended Sediment Sampling

Suspended sediment, which is the downstream mixture of all source sediment contributions, was collected for partitioning of the sediment load. Suspended sediment samples collected via grab sampling were used for radionuclide analysis (see Section 4.1.3).

4.2.4 Source Preparation Procedures

Soil and sediment samples were prepared for radionuclide analysis by isolating the clay fraction of each sample due to the affinity of radionuclides to attach to fine soil particles (He and Walling 1996). Initially, each sample was oven-dried for 48 hours at 60 °C then lightly crushed with a rolling pin. Larger particles were removed from the sample using a 2-mm sieve. A sodium hexametaphosphate deflocculating agent was added to the filtrate in a 1 mL of deflocculating agent to 1 g of sample ratio in order to disaggregate the soil particles further. After addition of the deflocculating agent, the samples were shaken overnight at 225 rpm to complete the disaggregation process. Samples were flushed through a 63-µm sieve to remove sand-sized particles. The filtrate was added to a 7.5-L bucket and diluted with deionized water to a volume of 6 L, which corresponds with a water column height of 15.2 cm in the bucket. Mixing of the water column for two minutes yielded a homogenous solution. The mixture was allowed to settle for 7.67 hr so that only clay-sized particles remained in suspension in the water column above the 5.1 cm level. The settling velocity was computed in accordance with Stokes' Law:

$$U_F = \frac{\rho_s - \rho_w}{18\mu} g d^2 \qquad 4.5$$

where U_F is particle fall velocity, ρ_s is soil density, μ is water viscosity, g is gravitational acceleration, and d is soil grain diameter. Dividing the fall distance by the settling velocity yielded the necessary settling time for the particles. Using Stokes' Law, an equation developed for spherical particles, provided a degree of safety in determining the settling velocity for the non-spherical clay-sized particles. Settling velocity equations for clay-sized particles developed by Gibbs (1985) provided settling velocities that were

faster than those velocities calculated using Stokes' Law. The faster settling velocity calculated using the equations developed by Gibbs (1985) decreased the time necessary for the particles to fall past the 5.1-cm level of the water column. This ensured that all silt-sized particles were removed from the solution above the 5.1-cm level.

The volume of solution above the 5.1-cm level was siphoned after settling using a small, 0.3-cm inside diameter tube, which minimized the siphoning of particles from below the established point. The mixing, settling, and siphoning process was completed three times to ensure the capture of a majority of the clay-sized particles. The three clay/water mixtures resulting from each process were pooled and aluminum sulfate was added to the mixture to facilitate flocculation and settling of the clay particles. The solution was dewatered and dried in an oven at 60 °C until all water was removed. The dried clay-sized particles were transferred from the glass jars to a Petri dish as the final preparatory step.

4.2.5 Precipitation Preparation Procedures

The radionuclides in the atmospheric influx were co-precipitated on an iron floc (Olsen et al. 1986) in order to be analyzed for this study. Initially, the pH of the sample was lowered to ~2 by adding 50 mL of 10% HCl, which prevents radionuclide sorption to the container or any particulate matter in the bucket. The sample was then passed through a coarse sieve to remove any large particulates. Ten mL of a 10% $FeCl_3$ solution were added to the sample. The pH of the sample was then raised to 8.2 with NaOH, which precipitated $Fe(OH)_3$ and the attached radionuclides. The resulting floc was allowed to settle overnight to ensure maximum sorption. Excess water was siphoned

from the sample and the remaining flocculent was collected in a 120 mL polyethylene specimen cup.

4.2.6 Gamma Spectroscopy

The radionuclide activities of the source sediments, suspended sediment, and precipitation samples were measured using gamma spectroscopy, which is a simple and non-destructive method of analyzing sample radioactivity. The radionuclides of interest in this study, which are measured using gamma spectroscopy, include ^{7}Be, ^{210}Pb, and Bismuth-214 (^{214}Bi, $t_{1/2}$=19.7 minutes). The production mechanisms of the radionuclides present in these samples is as follows. ^{7}Be is produced in the atmosphere through the cosmic ray spallation of nitrogen and oxygen nuclei. ^{210}Pb is produced as a daughter-product of the Uranium-238 (^{238}U, $t_{1/2}$=4.46 x 10^{9} years) decay series. ^{238}U decays through a series of daughters to produce the short-lived, gaseous Radon-222 (^{222}Rn, $t_{1/2}$=3.8 days). A portion of the ^{222}Rn diffuses out of the soil into the atmosphere while the remainder of the ^{222}Rn remains in the soil. In both cases, the ^{222}Rn decays to ^{210}Pb. The ^{210}Pb in the atmosphere is termed as excess and denoted as $^{210}Pb_{xs}$; ^{210}Pb in the soil is termed as supported and denoted as $^{210}Pb_{sup}$. The sum of $^{210}Pb_{xs}$ and $^{210}Pb_{sup}$ is identified as total ^{210}Pb. $^{210}Pb_{sup}$ is in equilibrium with the surrogate parent nuclide ^{214}Bi; thus, subtracting the activity of ^{214}Bi from the activity of ^{210}Pb yields the activity of $^{210}Pb_{xs}$ (Matisoff et al. 2005).

During gamma decay, the radionuclides emit electromagnetic radiation (i.e., gamma rays) at unique energy levels for each radionuclide. The emission at each of these discrete energy levels is a statistically constant fraction of the total number of decays (i.e., the branching ratio). Thus, the activity at any one of these discrete energies can be

utilized to determine the total activity of the isotope. For this study, the energy level of 477.6 keV was used for activities of ^{7}Be. At this energy, 10.5% of the total gamma emissions for ^{7}Be are emitted. The activity of $^{210}Pb_{xs}$ was determined as the difference between total ^{210}Pb and $^{210}Pb_{sup}$. Total ^{210}Pb was determined using the 46.54 keV energy level, where 4.25% of the gamma emissions are produced. ^{214}Bi and thus, $^{210}Pb_{sup}$, was determined at the 609 keV energy level where 46% of the ^{214}Bi emissions are released. The samples were counted three weeks after being sealed to allow secular equilibrium ingrowth of gaseous ^{222}Rn ($t_{1/2}$ = 3.82 days) from the decay of its ^{226}Ra ($t_{1/2}$ = 1600 years) parent (Matisoff et al. 2005).

For this study, an Ortec High Purity Germanium (HPGe) detector was used to count gamma ray emissions from each sample. The detector consists of a germanium crystal housed inside a protective casing. The crystal has a diameter of 70 mm and a length of 27.9 mm; it is spaced 4-mm from the outer casing. The protective casing is 0.761-mm thick and consists of a 0.76-mm thick carbon fiber layer on top of a 0.001-mm thick inactive germanium layer.

The detector measures the occurrence of gamma rays striking the HPGe crystal, which has a high-voltage applied across it. The energy of the gamma rays as it strikes the crystal is converted into a voltage. The voltages are converted to a digital signal using a DSPEC Jr. 2.0 integrated gamma spectrometer. The digital signals are related to the number of counts (i.e., number of gamma rays striking the crystal) per second (cps) using the GammaVision software program supplied by Ortec.

The efficiency at which the crystal detects gamma ray emissions is based on several factors including the sample material and geometry, as well as the dimensions and

properties of the crystal. Therefore, the detector must be calibrated against known standards with a wide range of photon energies. The calibration procedure for the Ortec detector is detailed in Appendix B.

The efficiencies determined through the detector calibration were applied to the output of the detector (cps) to determine the absolute activities of the samples. In addition, the branching ratio and mass of the sample were used in the absolute activity calculations.

The amount of energy emitted during decay of a radionuclide is a function of the amount of the radionuclide present in the sample. Thus, higher radionuclide activities indicate higher concentrations. The equation used to determine the activities, R_A, of ^{7}Be and ^{214}Bi, decay-corrected back to the day of collection, was calculated as:

$$R_A = \frac{(C-B_A)e^{\lambda t}}{mEB_R} \qquad 4.6$$

where C is emission rate (cps), B_A is background activity (cps), λ is the decay rate, t is the difference between collection date and counting date, m is the sample mass, E is the efficiency, and B_R is the branching ratio. The error of the activity (e_A) determined in Equation 4.7 was calculated from the propagation of error described in Taylor (1997) and is:

$$e_A = R_A\sqrt{\frac{(e_C)^2+(e_B)^2}{(C-B_A)^2}} \qquad 4.7$$

where e_C is the error of the emission rate and e_B is the error of the background. The activity for total ^{210}Pb was calculated as:

$$R_A = \frac{(C-B_A)F_C e^{\lambda t}}{mEB_R} \qquad 4.8$$

where F_C is the self-absorption correction factor, which is calculated using the following equation (Cutshall et al. 1983):

$$F_C = \frac{ln\left(\frac{T}{I}\right)}{\frac{T}{I}-1} \qquad 4.9$$

where T is the attenuated photon emission and I is the unattenuated photon emission through an empty sample container. The error of the activity was determined based on the propagation of error described in Taylor (1997) and is:

$$e_A = R_A \sqrt{\frac{(e_C)^2+(e_B)^2}{(C-B_A)^2+\left(\frac{e_F}{F_C}\right)^2}} \qquad 4.10$$

where e_F is the error of the correction factor.

Each sample was analyzed for 82800 s to obtain an acceptable analytical precision of less than ±10% at the 95% confidence level (Mabit et al. 2008). The accuracy of the gamma spectrometer used in this study is listed as < ±3% of the reference peak from 0 to 50000 cps (Ametek 2008).

4.3 Sediment Budget Verification

Verification of each component (U_C, B_C, CB_C) in Equation 1.2 was completed using a variety of methods unique to each component. The contribution of sediment to the total load resulting from each source (as represented by the suspended sediment concentration) was determined to allow for comparison to collected field data. U_C was established using the Water Erosion Prediction Project (WEPP) model. B_C was determined using cross-sectional surveys. CB_C was computed using the Einstein approach (Einstein 1950).

4.3.1 Upland Contribution (U_C)

Upland contributions to the study reach, U_C, were determined by simulating the June 19, 2009 event with a previously calibrated WEPP model (Abaci and Papanicolaou 2009). WEPP is a physically based, distributed parameter computer simulation model designed to predict erosion from agricultural fields and the resulting delivery of sediment to the outlet of small watersheds (Ascough et al. 1997). The model divides the landscape into individual hillslopes less than 2.6 km^2. WEPP can incorporate spatial and temporal variabilities of topography, land use, and soil characteristics into these hillslopes (Ascough et al. 1997). Inputs into the model also include crop characteristics, as well as both management and conservation practices. Certain climate variables are also needed. Hydrology components in the model are based on the daily water balance and focus on Hortonian flow and infiltration, which are calculated using a kinematic wave model and the Green-Ampt equation (Flanagan and Nearing 1995). Hillslope erosion processes, namely rill and inter-rill erosion, are calculated separately using a steady state sediment continuity equation (Nearing et al. 1989). Rill erosion is a function of the critical shear stress and inter-rill erosion relates to the rainfall intensity (Aksoy and Kavvas 2005). WEPP is capable of analyzing continuous simulations of several years or individual runoff events. However, WEPP does not incorporate overbank flow into its simulation, nor does it account for sediment source availability if operating in single-storm mode.

The WEPP simulation for this study was completed using only the fields bordering the stream reach. The calibrated/validated values for the land management practices (Figure 4.10) and soil characteristics (Figure 4.11) from Abaci and Papanicolaou (2009), as well as Light Detection And Ranging (LiDAR)-derived

elevation data were incorporated as the necessary data inputs. The precipitation characteristics of the June 19, 2009 event were entered as displayed in Figure 4.12.

The upland contribution was determined using the sediment yield and runoff volume output generated by a single storm simulation of WEPP for the June 19, 2009 event. The amount of sediment contributed by the uplands to the suspended load was computed by dividing the sediment yield by the runoff volume, yielding an average mass rate at which upland material was contributed to the suspended sediment load.

4.3.2 Bank Contribution (B_C)

The amount of sediment contributed during the June 19, 2009 event by the channel banks in the study reach, B_C, was determined by comparing pre-event and post-event cross-sectional surveys. Six cross-sections of the study reach were surveyed before and after the event using a Leica Total Station.

Sediment loss was determined at the three upstream cross-sections, which exhibited significant bank retreat. The three downstream cross-sections exhibited only minimal changes in cross-section geometry; therefore, the changes in cross-sectional areas were not calculated for these locations. The bank retreat at each of the three upstream cross-sections was determined by overlaying the pre- and post-event cross-sections, then digitizing the change in area.

Bank retreat was converted to a volume of sediment (V_{bank}) by averaging the area lost between each cross-section and multiplying by the length between the cross-sections, as displayed in Equation 4.11.

$$V_{bank} = \left(\frac{AR_i + AR_{i+1}}{2}\right)(L_{i+1} - L_i) \qquad 4.11$$

where AR is the cross-sectional loss of area and L is the downstream distance from the furthest upstream point of the study reach. The sediment volume lost was converted to a mass of sediment by multiplying by the soil density. The total sediment mass lost (g) was divided by the cumulative volume of flow passing through the reach over the course of the event (L) to obtain an average concentration (g L^{-1}) of bank material in the suspended load.

4.3.3 Channel Bed Contribution (CB_C)

Channel bed contributions (CB_C) were determined using the approach detailed in Einstein (1950). The Einstein approach assumes that the source of the suspended load is the active layer of the bed, typically defined as twice the soil grain diameter for which 50 percent of the material is finer (d_{50}) (Chang 2002), and is calculated as following:

$$C_s = 1000 \frac{q_b}{SG_S \rho_w Q_W} \left[2.303 \, log \left(\frac{30.2H}{\Delta} \right) I_1 + I_2 \right] \qquad 4.12$$

where q_b is the bed load discharge per unit width (see Equation 4.13), H is the flow depth, and Δ, I_1, and I_2 are defined by Equations 4.14, 4.15, and 4.16, respectively.

The bed load discharge per unit width, q_b, is defined using the following equation:

$$q_b = 40(\tau *)^3 \gamma_s F [g(SG_s - 1) d_{50}^3]^{1/2} \qquad 4.13$$

where τ* is the Shields stress, γ_s is the unit weight of the soil, and F is defined by Equation 4.14.

$$F = \left[\frac{2}{3} + \frac{36\nu^2}{g d_{50}^3 (SG_s - 1)} \right]^{1/2} - \left[\frac{36\nu^2}{g d_{50}^3 (SG_s - 1)} \right]^{1/2} \qquad 4.14$$

where ν is the kinematic viscosity of water.

$$\Delta = \frac{d_{65}}{X} \qquad 4.15$$

where d_{65} is the grain diameter for which 65 percent of the material is finer, as determined by Ellis (2009), and X is the correction factor in the logarithmic velocity distribution.

$$I_1 = 0.216 \frac{A^{z*-1}}{(1-A)^{z*}} \int_A^1 \left(\frac{1-\eta}{\eta}\right)^{z*} d\eta \qquad 4.16$$

where A is defined by 4.18, z* is defined by 4.19, and η is defined by 4.20.

$$I_2 = 0.216 \frac{A^{z*-1}}{(1-A)^{z*}} \int_A^1 \left(\frac{1-\eta}{\eta}\right)^{z*} ln(\eta)\, d\eta \qquad 4.17$$

$$A = \frac{L_a}{H} \qquad 4.18$$

where L_a is the depth of the active layer.

$$z* = \frac{U_F}{\kappa U*} \qquad 4.19$$

where U_F is the particle fall velocity at flow depth $z_f = L_a$, κ is the von Karman constant, and U* is the shear velocity.

$$\eta = \frac{z_f}{H} \qquad 4.20$$

Once Equations 4.12 through 4.20 have been solved, the mass flux per unit volume (g L^{-1}) from the active layer of the bed can be determined.

In summary, the inputs to Equation 1.2 were determined using two different sets of methods. The first set of methods incorporated field measurements, data collection, and subsequent radionuclide analysis. Suspended sediment concentrations and stream flow rates were determined through field measurements. Upland, bank, and bed contributions to the suspended load were determined through the radionuclide tracing technique, which required the collection of suspended sediment, source, and precipitation samples. All samples were analyzed after preparation using gamma spectroscopy. A

second set of methods used to verify the first set of methods used a combination of modeling (WEPP, Einstein approach) and observational (bank retreat) analysis.

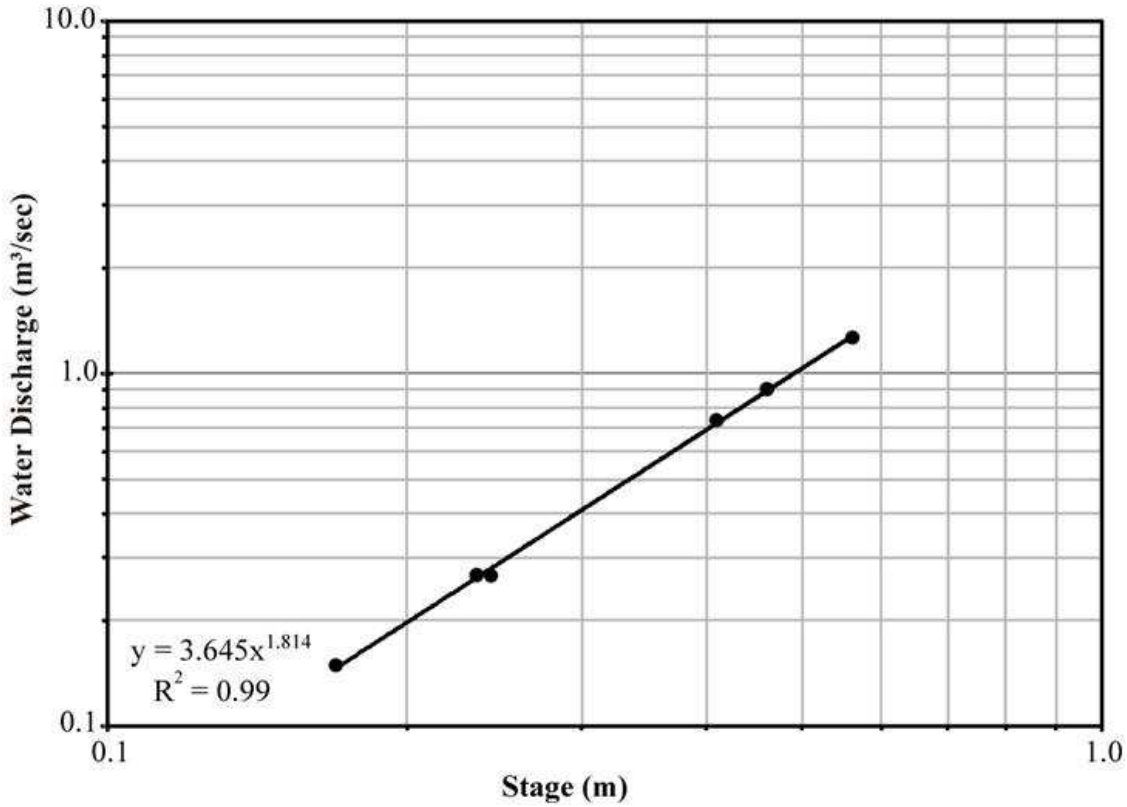

Figure 4.1. Stage-Discharge relationship (Abaci and Papanicolaou 2009)

Figure 4.2. Installed pressure transducer

Figure 4.3. Sigma sampler: the computer and pump are displayed in the top of the picture while the bottles used to store the samples are on the bottom

Figure 4.4. Example of SediMeter installation (Lindorm 2009a)

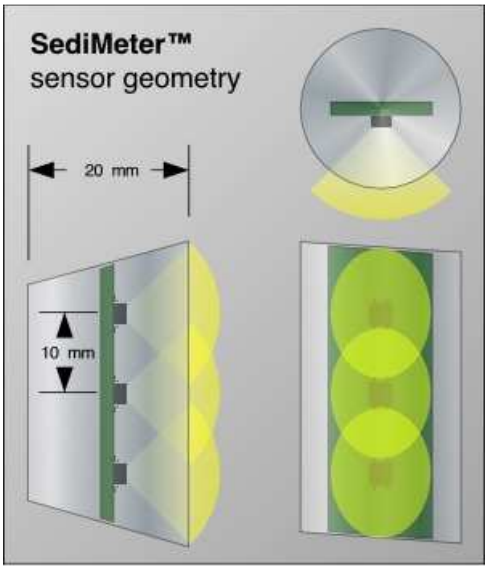

Figure 4.5. SediMeter sensor geometry (Lindorm 2009a)

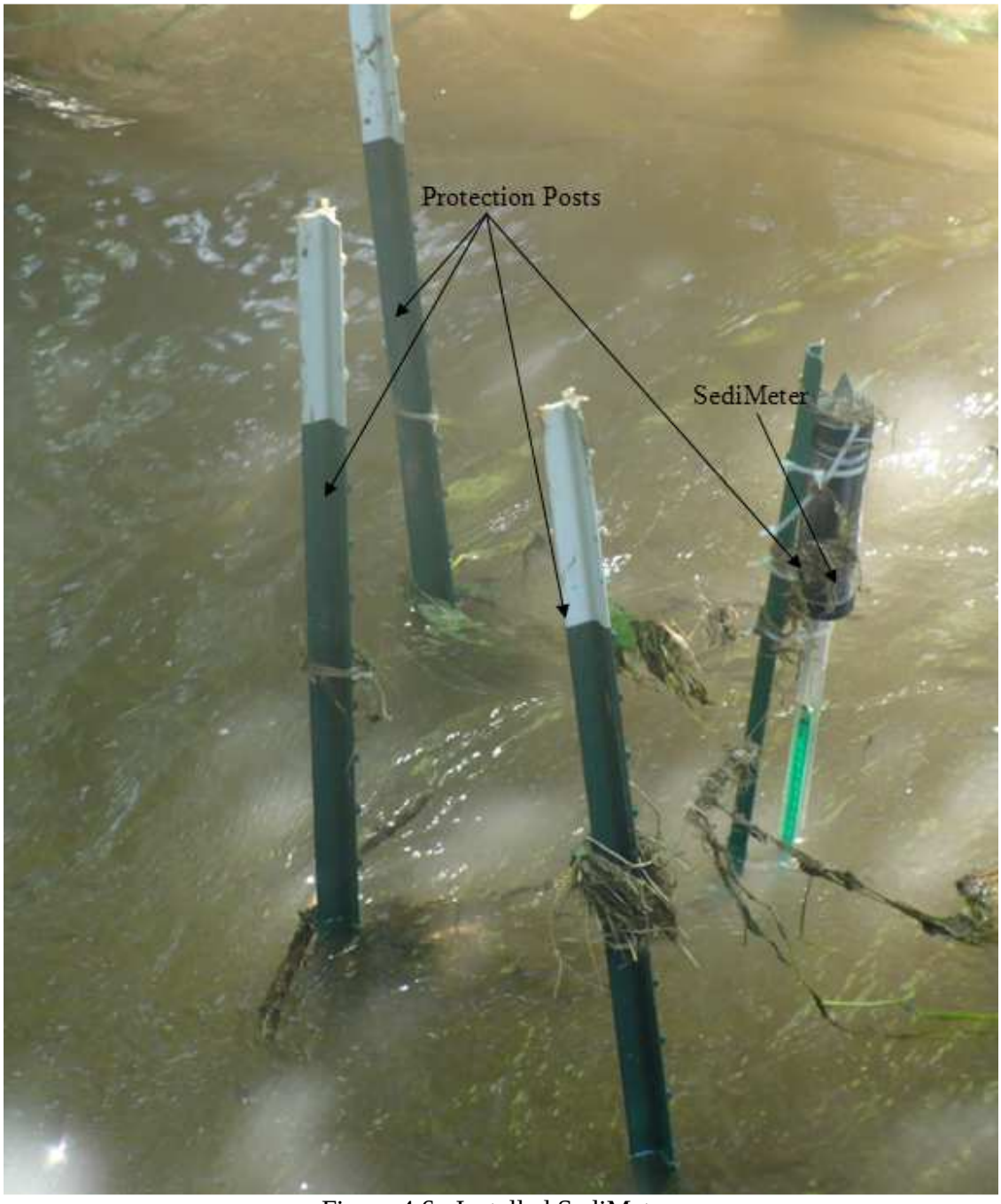

Figure 4.6. Installed SediMeter

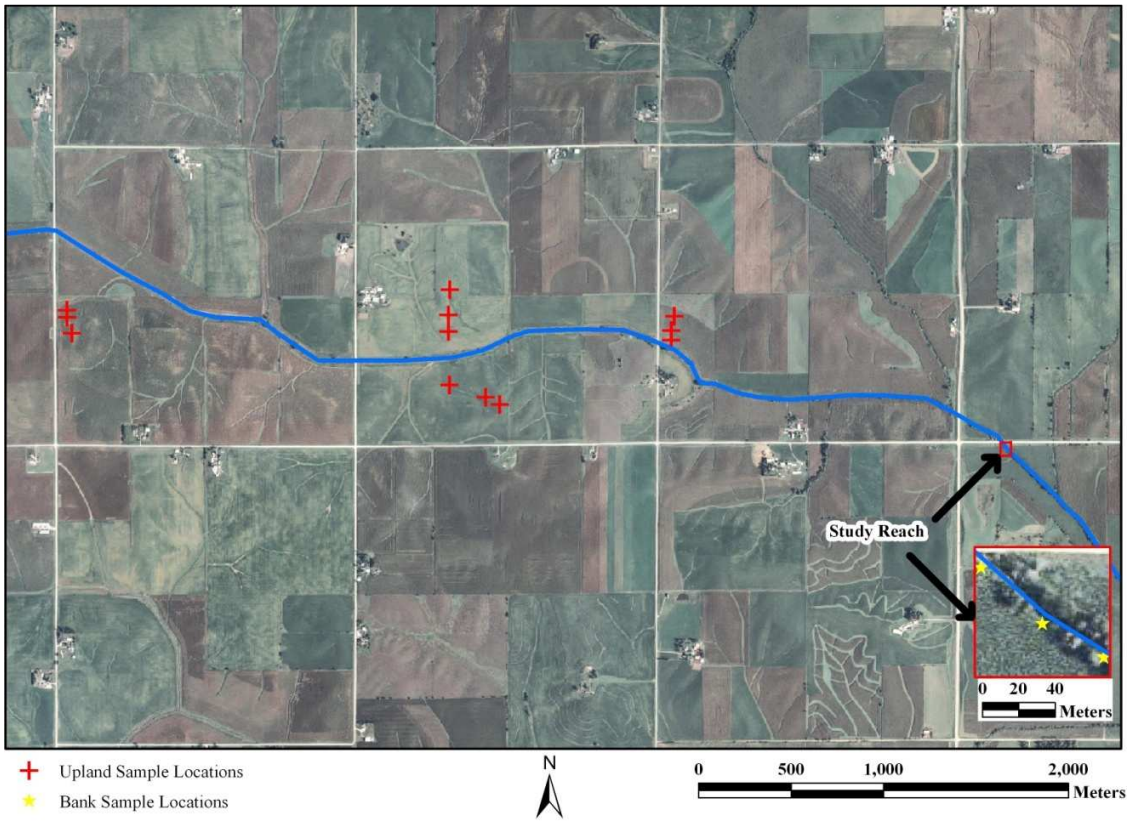

Figure 4.7. Sampling locations

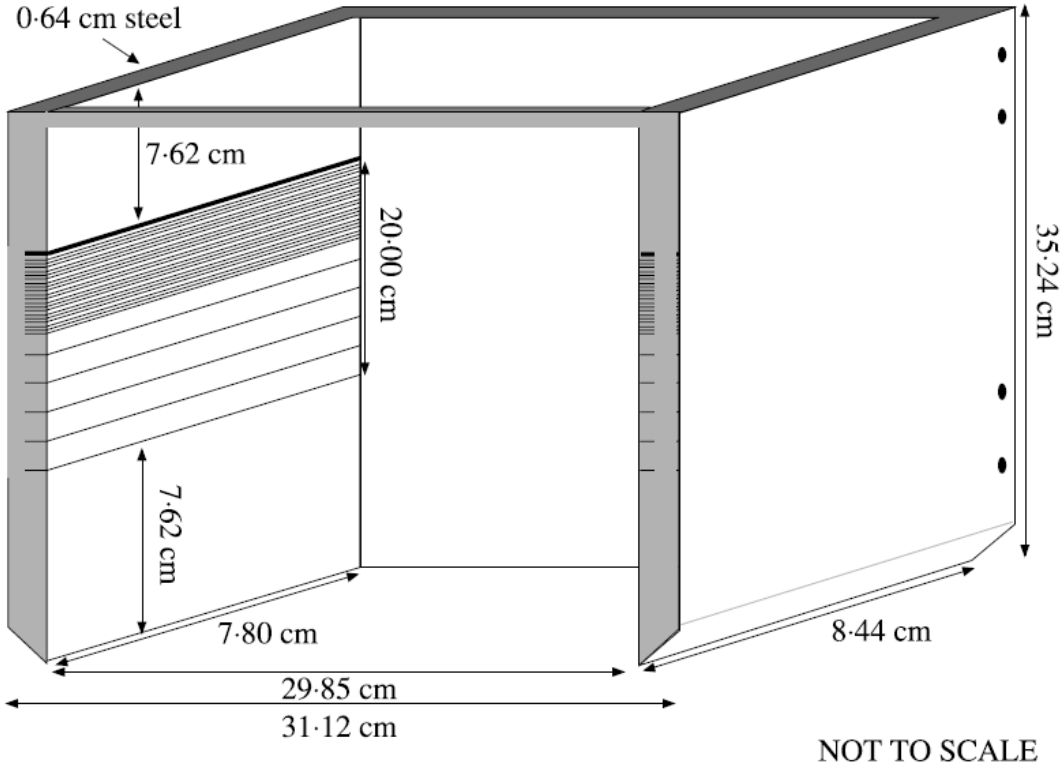

Figure 4.8. High-resolution profile sampler depiction

Figure 4.9. Upland source sample prepared for division into 5-cm increments

Operation Type	Name	Comments
Initial Conditions	FTC-NTB_EVENT01	
Tillage	CC_Field cultivator, secondary tillage, sweeps 12-2	Depth: 5.08 cm; Type: Sec
Tillage	CC_Planter, double disk openers	Depth: 5.08 cm; Type: Sec
Plant - Annual	CC_Corn_High Ferilization level	Row Width: 76.20 cm
Harvest - Annu	CC_Corn_High Ferilization level	
Tillage	CC_Planter with ripple coulter	Depth: 5.08 cm; Type: Sec
Tillage	CC_Planter, double disk openers	Depth: 5.08 cm; Type: Sec
Plant - Annual	CC_Soybeans - High Fertilization Level	Row Width: 38.10 cm
Harvest - Annu	CC_Soybeans - High Fertilization Level	
Tillage	CC_Chisel plow, straight with spike pts	Depth: 30.48 cm; Type: Pri
Tillage	CC_Anhydrous applicator with closing disks	Depth: 7.62 cm; Type: Sec

Figure 4.10. WEPP land management practices input

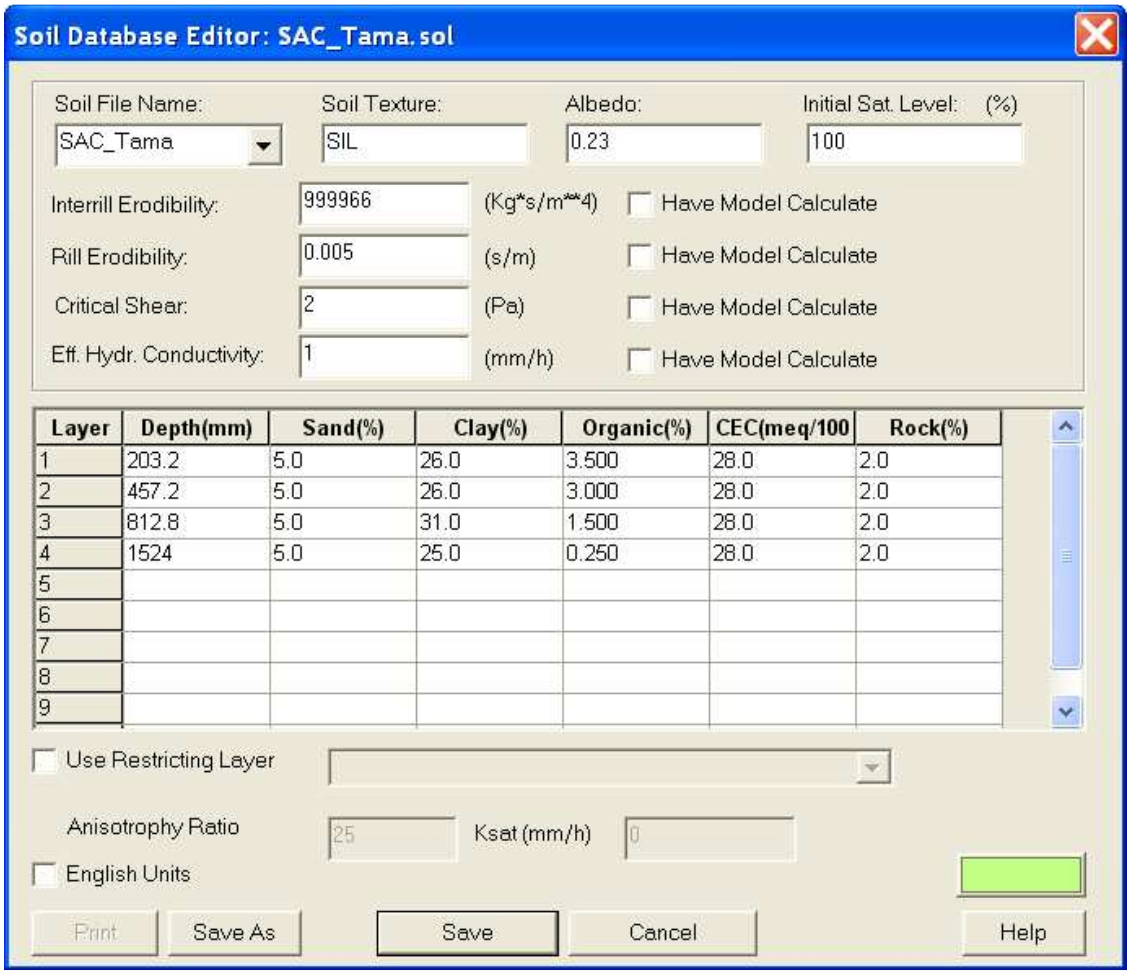

Layer	Depth(mm)	Sand(%)	Clay(%)	Organic(%)	CEC(meq/100	Rock(%)
1	203.2	5.0	26.0	3.500	28.0	2.0
2	457.2	5.0	26.0	3.000	28.0	2.0
3	812.8	5.0	31.0	1.500	28.0	2.0
4	1524	5.0	25.0	0.250	28.0	2.0
5						
6						
7						
8						
9						

Figure 4.11. WEPP soil type input

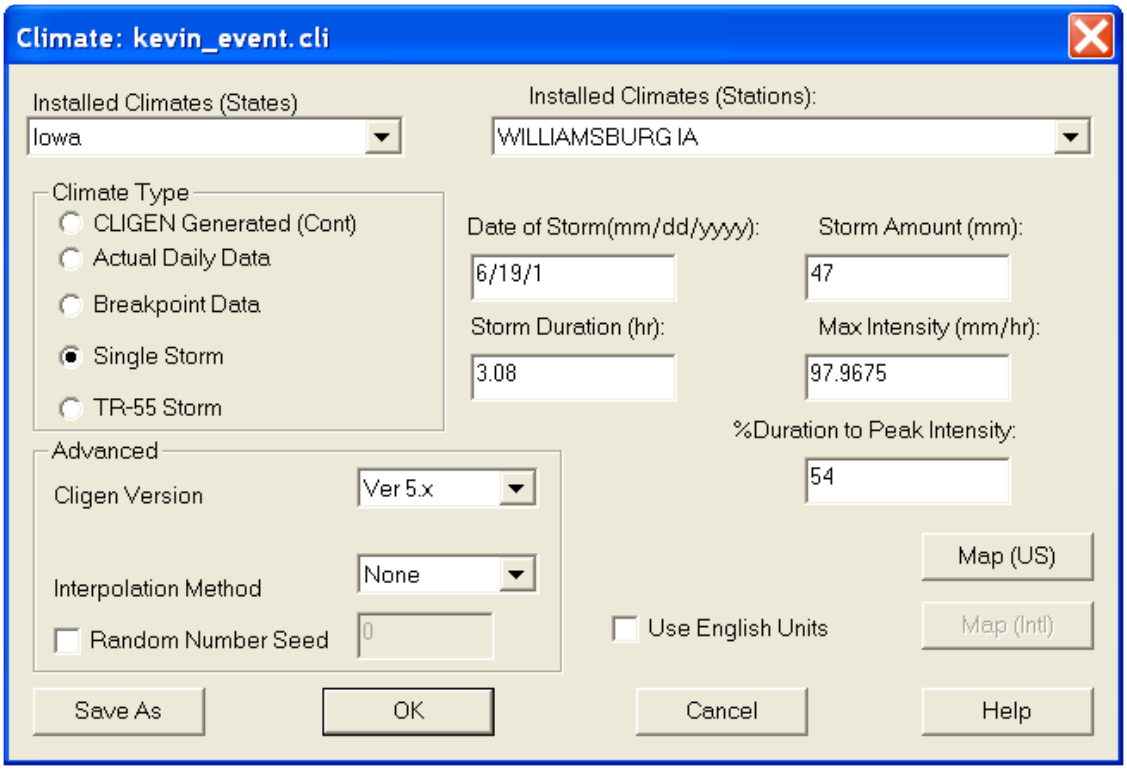

Figure 4.12. WEPP precipitation inputs

CHAPTER 5 RESULTS AND DISCUSSION

The results of this thesis are organized as follows. First, the hydrograph and sedigraph data are presented for the high flow events of June 16, 18, and 19, 2009 in the SASW; the hysteresis phenomenon occurring in these events is then discussed. Second, the suspended sediment loads are partitioned for the June 16 and 19, 2009 into relative contributions from the uplands and the channel are provided at sampled instants. Third, the results from the hysteresis analysis and the partitioning study are used in conjunction to close the sediment budget for the June 16 and 19 events. The results from the latter event are qualitatively compared against a combined prediction using the WEPP upland erosion model, an observation of bank retreat, and a calculation for bed resuspension. Finally, a discussion on potential sources of error in the data collection and analysis techniques are presented.

5.1 Hydrograph and Sedigraph Analysis

The relationships between 5-minute precipitation intensities, cumulative precipitations, and the resulting hydrographs for the sampled runoff events of June 16, 18, and 19, 2009 are presented in Figure 5.1, Figure 5.2, and Figure 5.3, respectively. An important point to note when comparing these Figures is the change in scale of the precipitation and flow rates. The maximum 5-minute precipitation rate for Event 1 (June 16, 2009) was 38 mm hr^{-1}. Precipitation intensities for this Event were bimodally distributed. Cumulative precipitation for Event 1 totaled 20 mm. Event 2 (June 18, 2009) was of higher intensity and magnitude than Event 1 with a maximum 5-minute precipitation rate of 52 mm hr^{-1} and a cumulative precipitation of 25 mm. The precipitation intensity of Event 2 was approximately unimodally distributed. Several

comparatively smaller peaks followed the maximum intensity; however, these subsequent peaks did not affect the modality of the distribution. Figure 5.3 presents the precipitation intensities for Event 3 (June 19, 2009); this Event produced extreme flash flooding of Clear Creek in the SASW. The cumulative rainfall for Event 3 (47 mm) was slightly above average (63rd percentile). However, the precipitation intensities for the Event were extreme as the storm produced the **sixth** highest 5-minute intensity (98 mm hr^{-1}) and the **second** highest 60-minute intensity (38 mm hr^{-1}) on record, dating back to the September 25, 2006 establishment of the tipping bucket site in Clear Creek (a span of approximately 1000 days).

The peak intensities and durations of the three rainfall Events produced distinctly different hydrograph shapes and magnitudes. The Event 1 hydrograph shows a wider deviation from the mean and a more gently sloping recessional limb compared to the hydrograph of Event 2. While the peak intensities and cumulative rainfall totals for Events 1 and 2 were similar, the total volumes of flow transported during the Events were distinctly different. Event 2 produced greater amounts of runoff because Event 1 increased the average saturation of the soil (see Figure 5.4), leading to reduced infiltration and increased amounts of overland flow in the subsequent event (Elhakeem and Papanicolaou 2009). Event 3 produced a hydrograph with a long period of an extremely high flow rate. This was the result of even higher antecedent moisture conditions, higher rainfall amounts, and extreme rainfall intensities.

The results of the SCS Method (Table 5.1) support the previous statements. The runoff depth for Events 1, 2, and 3 was determined to be 0.1 mm, 0.6 mm, and 13.0 mm, respectively. The percentage of precipitation produced as runoff also increased over the

course of the events, from 0.5% in Event 1 to 3.1% in Event 2 to 27.8% in Event 3. These results indicate that antecedent soil moisture had a large impact on the amount of runoff produced in each Event.

The varying rainfall intensities have been shown to affect suspended sediment concentrations significantly (Alexandrov et al. 2007; Smith et al. 2003). Thus, the hydrographs resulting from the differing rainfall intensities were plotted in relation to the sedigraphs in Figure 5.5, Figure 5.6, and Figure 5.7. These charts display the suspended sediment concentrations for the samples collected using the three different sampling techniques, namely grab sampling, the Sigma sampler, and the SediMeter. Additionally, one suspended sediment sample using a DH-48 hand-held depth-integrating sampler was collected by Zager (2009) during Event 3.

The suspended sediment concentrations measured by the three techniques agreed well despite the differences in operating principles (see Chapter 4). Specifically, the grab sampling technique provided a point measurement from the top of the water column, the Sigma sampling technique gave a point measurement near the bottom of the water column, and the SediMeter presented an integrated profile of concentration measurements (limited to the instrument height). The maximum percent difference between any of the two techniques for a single sample was only 19%. This deviation, which occurred at the first Sigma sampling of Event 2, was attributed to the inherent differences between point measurements (i.e., Sigma or grab samples) and integrated concentration measurements from the SediMeter.

The pros and cons of the various sampling techniques are shown in Figure 5.6 and Figure 5.7. Continuous measurements were not feasible with either the grab or Sigma

sampling techniques, prompting the need for fully automated measurements to capture more accurately intra-event variability in sediment fluxes. As shown in Figure 5.6, the SediMeter was able to provide unattended measurements during the peak of the hydrograph. However, during Event 3, the excessive debris (corn tassels, leaves, and other forms of residue; see Figure 5.8 for example of debris delivered during the event) wrapped around the SediMeter (i.e., biofouling), thereby causing erroneous suspended sediment measurements. Gradual, increasing trends of suspended sediment measurements resulting from biofouling has been observed in previous studies (e.g., Ridd and Larcombe 1994).

A simple experiment was completed to confirm that biofouling was the cause of the artificially high SediMeter measurements. Residue obtained from the study site was wrapped around the entire SediMeter. The residue-covered SediMeter was then placed in a large container full of water to simulate the stream environment. Measurements were recorded with the SediMeter in this condition. The outcome of this test showed that the complete covering of the instrument resulted in values similar to those recorded during Event 3 (Figure 5.9). Therefore, biofouling was considered to have triggered artificially high SediMeter readings once overbank flow commenced. For these reasons, the Event 3 SediMeter measurements after the first hydrograph peak were not considered in the sediment budget analysis (see Figure 5.10 for measurements considered valid).

In addition, the Sigma samples collected during the high flows of Event 3 were excluded from the sediment budget calculations for this Event because overbank flow flooded the sample containers and compromised all Sigma samples for the event. Due to the invalidation of a majority of the suspended sediment measurements for Event 3 (i.e.,

the SediMeter and the Sigma samples), an accurate estimation of the total sediment load could not be made. However, the total sediment flux (Q_S) was computed by multiplying the measured values of C_S and Q_W during Events 1 and 2 because sufficient measurements were collected over the courses of the Events. The start of each event was determined to be the time at which C_S increased above the average baseflow concentration of 0.5 g L^{-1}. The end of each event was likewise delineated as the time at which the concentration decreased back to the average baseflow C_S. Using these parameters, Q_S was equal to 20,000 kg for Event 1 and 200,400 kg for Event 2.

Sediment loads for the three events were also calculated using a sediment rating curve for the SASW Clear Creek outlet (Figure 5.11) developed by Zager (2009). Using this curve, the estimated Q_S was 9,600 kg for Event 1, 45,700 kg for Event 2, and 1,364,500 kg for Event 3. The flux for Event 1 was underestimated by the sediment rating curve by 52% while Event 2 was underestimated by 77%. Thus, traditional sediment rating curves, such as the one developed by Zager (2009), should be used with caution when attempting to predict total sediment yield during high flow events. This shortcoming is magnified because a majority of the annual sediment load is transported during high flow events (Lenzi et al. 2003; Markus and Demissie 2006).

One of the primary reasons that the sediment rating curve under-predicts the suspended sediment loading is that the sediment rating curve assumes a linear relationship between Q_S and water flow rate (Q_W) while the actual relationship between Q_S and Q_W during high flow events is non-linear. Figure 5.12, Figure 5.13, and Figure 5.14 illustrate the non-linear relationship between C_S and Q_W during Events 1, 2, and 3, respectively. In all events, a clockwise hysteresis is observed at the SASW outlet.

Clockwise hysteresis is often explained as resulting from source material exhaustion; several previous studies have shown such a relationship (e.g., Baca 2008; Doomen et al. 2008; Salant et al. 2008; Seeger et al. 2004; Smith and Dragovich 2009; Williams 1989). The triggering mechanism for the clockwise hysteresis shown in Events 1 and 2 is suggested to be the limited availability of loose fine material in the uplands. In this case, rainsplash and runoff are the two mechanisms of source supply from the uplands.

While Event 3 also produced a clockwise hysteresis, the discrepancy between the rising and falling limb C_S at the same Q_W is much less pronounced than for the previous two events (i.e., the hysteresis effect was dampened). The dampening of the clockwise hysteresis for Event 3 is suggested to be the result of overbank flow, which has the ability to provide an uninterrupted supply of easily-eroded sediment from inundated upland areas (i.e., floodplains) bordering the stream (Alexandrov et al. 2003). Thus, overbank flow contributed additional upland sediment throughout Event 3, reducing the discrepancy between the suspended sediment concentrations. While rainsplash and runoff over bare soils have been discussed extensively in the literature (Abaci and Papanicolaou 2009; Steegen et al. 2000; Vandaele and Poesen 1995), few studies provide data to support the role of overbank flow on the relationship between C_S and Q_W, making this finding unique.

In summary, analysis of Figure 5.1, Figure 5.2, and Figure 5.3 show that high precipitation intensities resulted in high rates of runoff. Figure 5.5, Figure 5.6, and Figure 5.7 offer a comparison amongst different measuring techniques, demonstrate the limitations of each measurement technique, and can be used to calculate suspended sediment flux. Figure 5.12, Figure 5.13, and Figure 5.14 show that flow lags behind

suspended sediment concentrations, forming a clockwise hysteresis pattern; however, the hysteresis for Event 3 was dampened due to entrainment of sediment by overland flow. The nature of the hysteresis processes for the events is viewed later in conjunction with the sediment load partitioning.

5.2 Sediment Load Partitioning

The second objective of this study was to partition the suspended sediment loads for Events 1 and 3 into relative contributions from the uplands and the channel using the activities of ^{7}Be and $^{210}Pb_{xs}$ (adequate samples for Event 2 were unable to be collected due to the abruptness and timing of the event). The first step in the load partitioning was to identify the activities of the two source areas: i) the eroded upland soil after the influx of radionuclides in precipitation and ii) the channel sediments in Clear Creek. Next, the suspended sediment activities during Events 1 and 3 were plotted in relation to the source activities to form a two end-member unmixing model. Finally, the relative contributions from the two sources to each suspended sediment sample were found using the unmixing model.

5.2.1 Upland Source (U_C) Activities

The radionuclide activities of the upland source (i.e., eroded surface soils) were determined using the pre-existing activity profiles of ^{7}Be and $^{210}Pb_{xs}$ in the soil and the atmospheric radionuclide influxes during the events. The pre-existing radionuclide activities of the uplands (Figure 5.15 and Figure 5.16) were determined by analyzing soil samples obtained using a high-resolution sampling technique (Wilson et al. 2003), which produced samples at incremental depths of 0.5 cm. One sample was analyzed at depth intervals greater than 1.5 cm simply to confirm that negligible radionuclide activities

(specifically ^{7}Be) existed at these depths. Figure 5.15 shows that the ^{7}Be activities can be considered essentially negligible when the analysis error is taken into account.

Large spatial variabilities were exhibited between sampling sites. The maximum coefficient of variation at each depth interval was 19% for the ^{7}Be activities and 68% for the $^{210}Pb_{xs}$ activities. Thus, the inventories of each depth interval were pooled to create average radionuclide profiles (Wilson et al. 2003). The average ^{7}Be and $^{210}Pb_{xs}$ pre-event profiles are displayed in Figure 5.17 and Figure 5.18.

Moreover, the atmospheric influxes of the radionuclides varied considerably between the three events. The influxes of the radionuclides from Event 3 were much smaller than the influxes from Events 1 and 2, even though Event 3 had more total rainfall than Events 1 and 2 combined. The reason for this is there was insufficient time to allow for the replenishment of radionuclides in the atmosphere after substantial amounts were removed during the previous two events. In line with the findings from this study, radionuclide concentrations in precipitation have been shown to decrease over the course of an event and over closely spaced events in past research (Dibb 1989; Ioannidou and Papastefanou 2006; Wallbrink and Murray 1994). Thus, the cause of the relatively small atmospheric influx of radionuclides during Event 3 is the scavenging (i.e., removal) of ^{7}Be and $^{210}Pb_{xs}$ in the atmosphere during Events 1 and 2.

The atmospheric influxes of the radionuclides have been shown to develop sharp exponential profiles in surface soils (Owens et al. 1996; Wilson et al. 2003) due to rapid and strong bonding to finer surface soil particles (Bonniwell et al. 1999; Olsen et al. 1986; Wallbrink and Murray 1996). Thus, the atmospheric radionuclide influx, D, was

distributed exponentially over the top 1.5 cm of the pre-existing radionuclide profiles using Equation 5.1:

$$R_A(z) = D(1 - e^{-4.297*depth}) \qquad 5.1$$

where R_A is the radionuclide activity at depth z (mBq cm^{-2}).

The profiles developed for the radionuclide distribution of ^{7}Be and $^{210}Pb_{xs}$ for Event 1 are shown in Figure 5.19 and Figure 5.20, respectively. The profiles for Event 3 are shown in Figure 5.21 and Figure 5.22. The pre-event profiles of Event 3 were higher than the pre-event profiles for Event 1 because of the atmospheric additions associated with Events 1 and 2.

The activity of the eroded upland soil was determined for each event by fitting an exponential curve to the post-precipitation profile (Wilson et al. 2003). The value of the exponential when the depth was equal to zero (thus, the activity at the surface) was used as the activity of the eroded upland soil. Figure 5.23 and Figure 5.24 show the activity of ^{7}Be and $^{210}Pb_{xs}$, respectively, at the upland surface for Event 1. Figure 5.25 and Figure 5.26 show the same for Event 3. The activities of all profiles decreased exponentially with depth, similar to numerous previous studies (Blake et al. 1999; Bonniwell et al. 1999; Owens et al. 1996; Wallbrink and Murray 1993; Walling et al. 1999).

5.2.2 Channel Source (B_C + CB_C) Activities

The source activities of the channel sediments were considered to be the integrated activities of the 1-m cores collected along the study reach. Radionuclide contributions from the bed were considered negligible because the bed was comprised mostly of sand particles (He and Walling 1996). The measured activities of $^{210}Pb_{xs}$ and ^{7}Be from the three 1-m cores collected along the study reach averaged 35.1 ± 6.5 mBq g^{-1}

and 2.3 ± 18.9 mBq g^{-1}, respectively. The activity of ^{7}Be was essentially zero when considering the error. The bank height in the sampling area was approximately 3 m; therefore, activities of $^{210}Pb_{xs}$ may have been closer to zero if the entire depth was sampled due to incorporation of more radioactively dead sediment.

5.2.3 Unmixing Model Creation

The relative contribution of each source (upland and channel) was determined for the suspended sediment collected by grab sampling during Events 1 and 3 using a two end-member unmixing model. The two source end members were considered to be the average activities of ^{7}Be and $^{210}Pb_{xs}$ for the eroded upland soils and channel sediment (Table 5.2). Plotting activities of ^{7}Be versus activities of $^{210}Pb_{xs}$ resulted in the two sources being plotted at different ends of a graph. This showed that the two activities used in relation to one another could provide a unique signature for each source material (Wilson et al. 2008).

Each event required the use of a separate two end-member unmixing model because the upland source activities for the events were different. The unmixing models for Events 1 and 3 are shown in Figure 5.27 and Figure 5.28, respectively. The activities of the suspended sediment captured during the Events were plotted on their corresponding unmixing model. A line was projected at right angles towards the unmixing line from each of the suspended sediment points. The position where this new line intersected the unmixing line dictated the relative percentage of each source type (Wilson et al. 2008).

The results from the two end-member unmixing model are represented in pie charts displayed over the event hydrographs (Figure 5.29 for Event 1 and Figure 5.30 for

Event 3). The proportion of blue in each pie represents the relative amount of eroded upland soil contributed to the suspended sediment load at the time of collection; likewise, the proportion of red in each pie chart represents the relative percentage from channel sources. The proportion of eroded upland soils was high in the beginning stages of Event 1, similar to the studies by Kuhnle et al. (2008) and Wilson et al. (2008).

The dominance of upland soils in the early stages of the event is due to rapid mobilization of fine loose particles by overland flow in the uplands. These easily entrained soils either were deposited during the previous runoff event (Ghadiri et al. 2001) or were loosened by rainsplash. Once the easily entrained soils were swept away by the "first flush" of overland flow, the amount of material available to be readily mobilized by overland flow was significantly reduced (Stutter et al. 2008). This allowed the channel to become the dominant contributor to the suspended load in the later stages of Event 1. Furthermore, sediment contributed to the flow by bank collapse typically occurs on the falling limb of the hydrograph (Springer et al. 1985; Thorne 1982), further increasing the proportion of sediments derived from the channel during this period. These results are again similar to the studies by Kuhnle et al. (2008) and Wilson et al. (2008), with the exception of one point. The last sample had a higher contribution from the uplands during this period than from the channel. No physical meaning behind this outlier can be advanced, especially when considering that overland flow (and thus upland contributions to the suspended load) had essentially ceased at this point.

Samples for radionuclide analysis were not collected for the beginning of Event 3; however, samples captured for the last half of the Event had higher relative channel

contributions than the upland source. This trend is important in the closure of the Event 3 sediment budget.

5.3 Sediment Budget Closure

The sediment budget for Events 1 and 3 are closed herein by combining the results of the hysteresis phenomenon with the results of the load partitioning. The results for Event 3 are then qualitatively compared with a sediment budget that was developed by incorporating results from the WEPP upland erosion model, observational analysis of bank retreat, and calculated bed resuspension.

5.3.1 Combination of Field-Based Results

The quantitative field measurements of flow and suspended sediment were used in conjunction with the load partitioning results to close the sediment budget for Event 1 using Equation 1.2. Suspended sediment transported during the rising limb of the hydrograph was primarily from the upland source, while the falling limb was dominated by channel sediment (Figure 5.29 and Figure 5.30). The primary reason for this change in the dominant sediment source was that the upland source quickly became exhausted, as shown with the clockwise hysteresis phenomenon (Klein 1984; Stutter et al. 2008).

Based on field measurements, the total sediment transported (Q_S) during Event 1 was 20,000 kg. Combining the quantitative suspended sediment measurements with the quantitative load partitioning analysis revealed that 61% (12,200 kg) of the total sediment transported during the Event was derived from the uplands (U_C). The channel banks contributed 39% (7,900 kg), with the majority of the channel sediment being transported during the falling limb of the hydrograph. Table 5.3 displays the contribution from each

source to the suspended load (Q_S) throughout the event. Equation 5.2 was used to determine total Q_S:

$$Q_{S,i} = \left(\frac{C_{S,i}+C_{S,i-1}}{2}\right)\left(\frac{Q_{W,i}+Q_{W,i-1}}{2}\right)(t_i - t_{i-1}) \qquad 5.2$$

The above quantitative analysis cannot be conducted for Event 3 because i) grab samples were not collected during the rising limb of the Event and ii) biofouling of the SediMeter produced erroneous results during the later portion of the hydrograph. However, a qualitative statement in regards to the suspended sediment load partitioning can be made by incorporating the results from Event 1 and other studies (e.g., Wilson et al. 2008) into the analysis.

The clockwise hysteresis phenomenon that occurred in Event 1 also occurred during Event 3. Because of the similarity in hysteresis phenomena, the trends revealed in Event 1 were assumed to repeat in Event 3. Moreover, similar studies have shown that upland contributions are dominant during the rising limb of the hydrograph (Stutter et al. 2008; Wilson et al. 2008). Thus, it was assumed that the upland was the dominant contributor to the suspended load during the rising limb of Event 3. Further supporting the conclusion that upland contributions remained significant during the later stages of the event was that the overbank flow provided additional upland sediment to the suspended load (Klein 1984), as exhibited by the dampened hysteresis phenomenon (Figure 5.14). While a quantitative closure of the sediment budget cannot be completed for Event 3 due to the limited number of suspended sediment samples, the budget can be qualitatively closed by suggesting that the upland source (U_C) was the dominant contributor to the suspended load during Event 3.

5.3.2 Sediment Budget Verification for Event 3

Verification of each component (U_C, B_C, CB_C) in Equation 1.2 was completed using a variety of methods unique to each component. The suspended sediment concentration resulting from each source was determined to allow for a qualitative comparison to the limited collected field data. U_C was established using the Water Erosion Prediction Project (WEPP) model. B_C was determined using cross-sectional surveys. CB_C was computed using the Einstein approach (Einstein 1950).

U_C for Event 3 was determined based on a WEPP simulation for fields bordering the study reach. Table 5.4 displays the results of the simulation. The uplands were calculated to contribute an average of 7.8 g L^{-1} to the suspended load over the course of Event 3.

The amount of material contributed during Event 3 by the channel banks in the study reach, B_C, was determined by comparing pre-event and post-event cross-sectional surveys. Figure 5.31 displays an example of the surveys. Figure 5.32 and Figure 5.33 show a photographic comparison between the pre- and post-event channel. Table 5.5 shows the results of the survey analysis. The banks contributed an average of 0.5 g L^{-1} to the suspended load over the course of Event 3. An important point to note is that the contribution from the banks in the study reach was likely higher there than in the more upstream sections due to the steeper bank slopes present near the outlet. Therefore, the average amount of material contributed from the banks was likely less than 0.5 g L^{-1}; however, this claim cannot be fully backed up due to a lack of bank retreat data in the upstream sections.

The channel bed contribution (CB_C) at the average stage and flow rate for Event 3 was determined using the Einstein approach (1950). The equations required to determine the contribution are outlined in Chapter 4; the values of the variables used in the equations are displayed in Table 5.6. Completion of the approach yielded an average bed contribution to the suspended load for Event 3 of 0.3 g L^{-1}.

Equation 1.2 was used to close the averaged simulated sediment budget. The average suspended sediment concentration of material eroding from the uplands was predicted to be 7.8 g L^{-1} by WEPP. The average bank contribution over the course of the Event was determined to be 0.5 g L^{-1}. Finally, the average bed contribution during the Event was calculated to be 0.3 g L^{-1}. The summation of these values in accordance with Equation 1.2 yields a total average suspended sediment concentration of 8.6 g L^{-1}. It is important to note that these values are simply averages from throughout the event and are thus difficult to compare against any specific field measurement. However, a qualitative analysis of the relative yield from each source is useful. Based on the above results, the uplands (U_C) contributed the vast majority of the sediment to the suspended load (91%). The channel sources (B_C and CB_C) contributed minimally to the total load. Qualitatively, this result agrees well with the result from the field study: the uplands were the dominant contributor to the suspended sediment load in the SASW.

5.4 Possible Errors

5.4.1 Sediment Load Calculation

One potential error in the sediment loading calculation is that the grab sampling technique is not conducive to accurately profiling the suspended sediment concentrations during high flow events. All grab samples are taken from the top of the water column;

this location has the lowest suspended sediment concentration in the water column (Winterwerp 2001). The maximum water stage in Event 3 was 3.9 m. Thus, the bucket (with a diameter of 0.14 m) only sampled about 4% of the total flow depth. In contrast, the stage only rose to a height of 0.55 m during the sampling of Events 1 and 2. In these cases, the bucket sampled about 25% of the total flow depth. Therefore, the concentrations sampled during Event 3 using the grab sampling technique are not necessarily representative of the average suspended sediment concentration (Alexandrov et al. 2003). Evidence of this is shown by comparing the concentrations determined by the grab sampling technique and the depth-integrated sampler at the first grab sampling time during Event 3. The depth-integrated sampler recorded a suspended sediment concentration of 5.5 g L^{-1}, while the grab sampler recorded a concentration of only 3.4 g L^{-1}.

The relative lack of integrated profiling necessitated the exclusion of the grab sample results from the Event 3 hysteresis chart because the grab sample concentrations are likely smaller than the average concentrations. If the results from the SediMeter and the grab sampling techniques had both been used in the hysteresis chart, the SediMeter (sampling from the more concentrated bottom of the suspended sediment profile) would have shown higher suspended sediment concentrations at the beginning of the hydrograph (when it was correctly functioning), causing an artificial clockwise hysteresis, simply due to its bottom-of-the-profile sampling location. Because the primary purpose of the hysteresis chart is to display the relative relationship between concentration and flow rate; plotting only results obtained from one technique accurately

displayed any trends in the relationship, regardless of the sampling location in the water column.

5.4.2 Sediment Load Partitioning

Extensive rill and gully erosion in the SASW could cause error in the radionuclide tracer results. Because the activity of the upland soils decreases exponentially with depth, soil eroded from these areas would have lower activities than as theorized by the unmixing model (Wallbrink and Murray 1993; Yang et al. 2006). This would cause the upland soils to have radionuclide signatures resembling the channel sediments after the formation of rills and gullies. Thus, sediments originating in the uplands may be misinterpreted as having come from the channel.

Additionally, resuspended bed sediment could not be quantified using the radionuclide tracing technique. The technique requires the analysis of only the clay-sized fraction. Because the bed was comprised predominantly of sand-sized particles, the contributions resulting from this source were not identifiable.

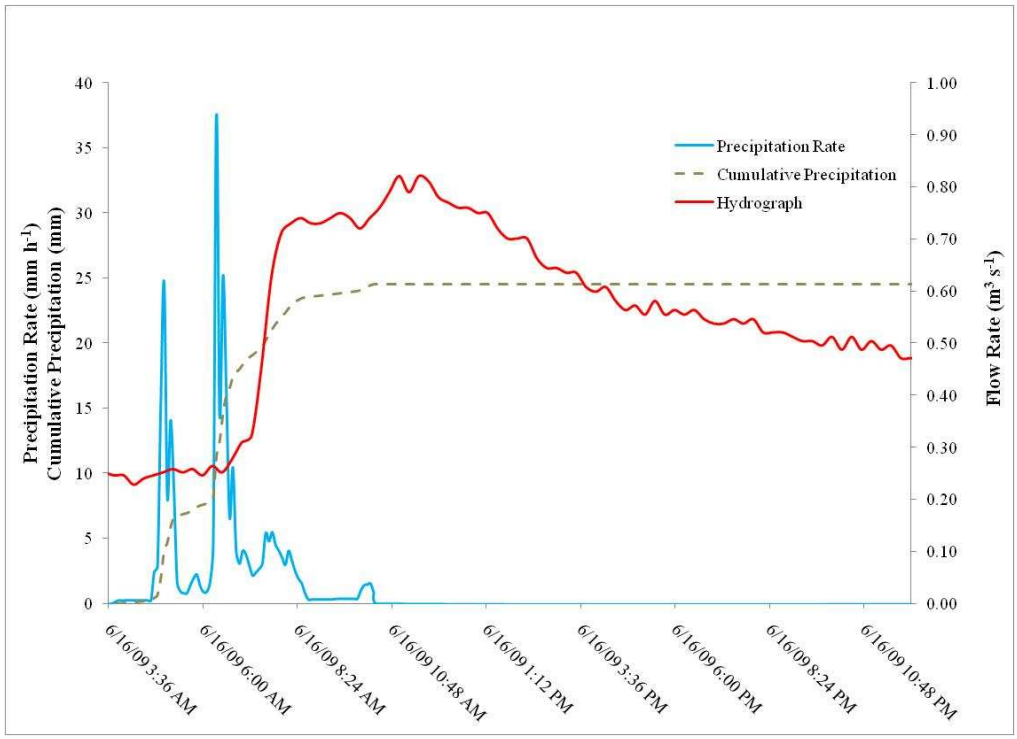

Figure 5.1. Precipitation and resulting hydrograph for June 16, 2009 event

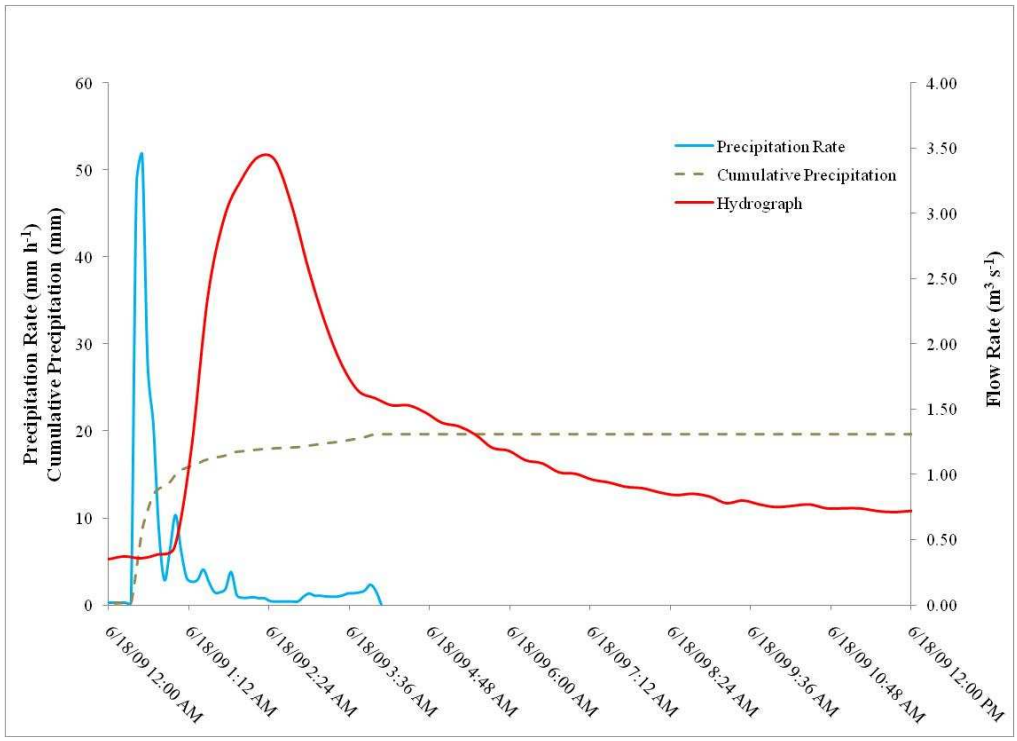

Figure 5.2. Precipitation and resulting hydrograph for June 18, 2009 event

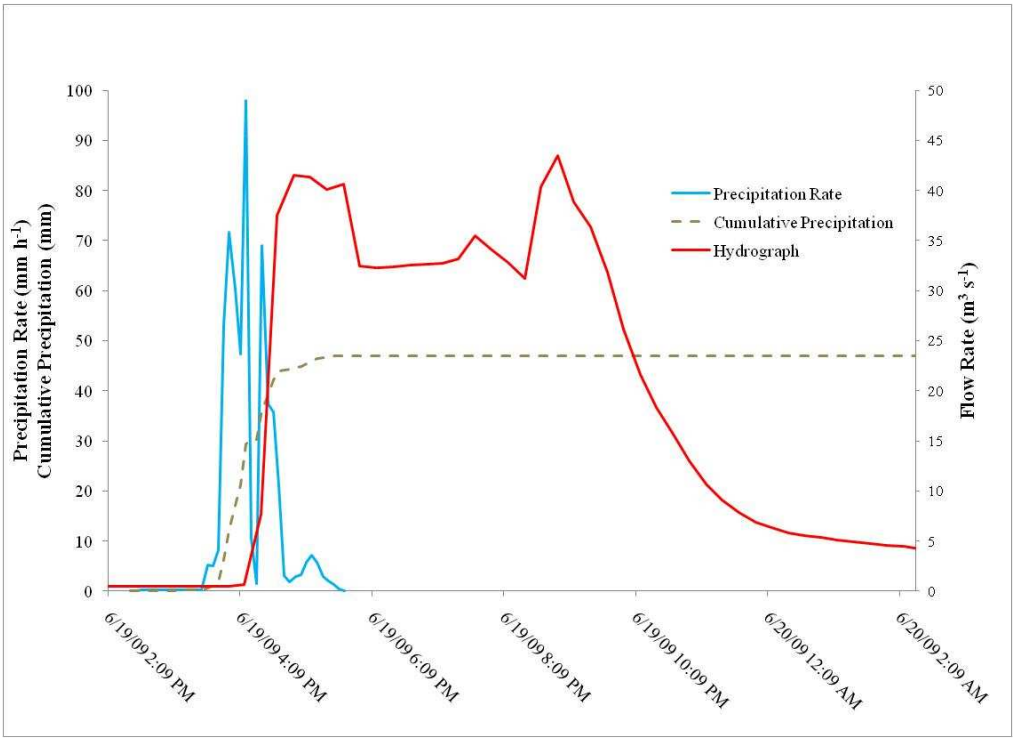

Figure 5.3. Precipitation and resulting hydrograph for June 19, 2009 event

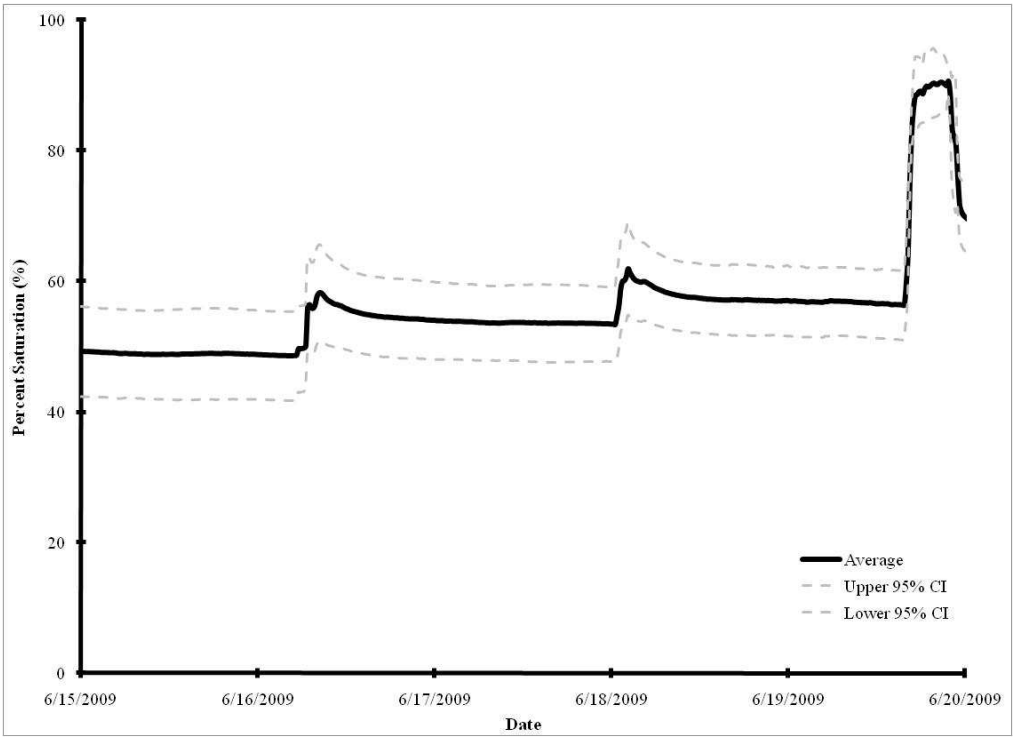

Figure 5.4. Average percent saturation over study period

Table 5.1. SCS Method variables

Event Date	Hydrologic Soil Group	Antecedent Moisture Condition	CN	S (mm)	R_D (mm)
June 16, 2009	B	I	64	143	0.1
June 18, 2009	B	I	64	143	0.6
June 19, 2009	B	II	81	60	13.0

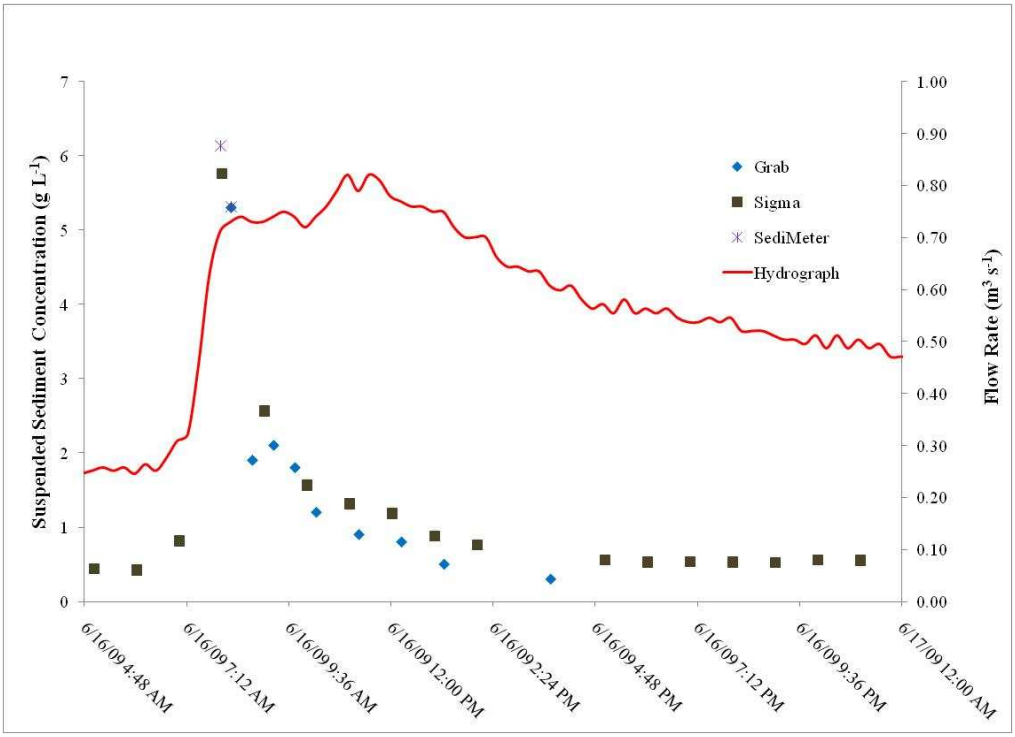

Figure 5.5. Sedigraph for June 16, 2009 event

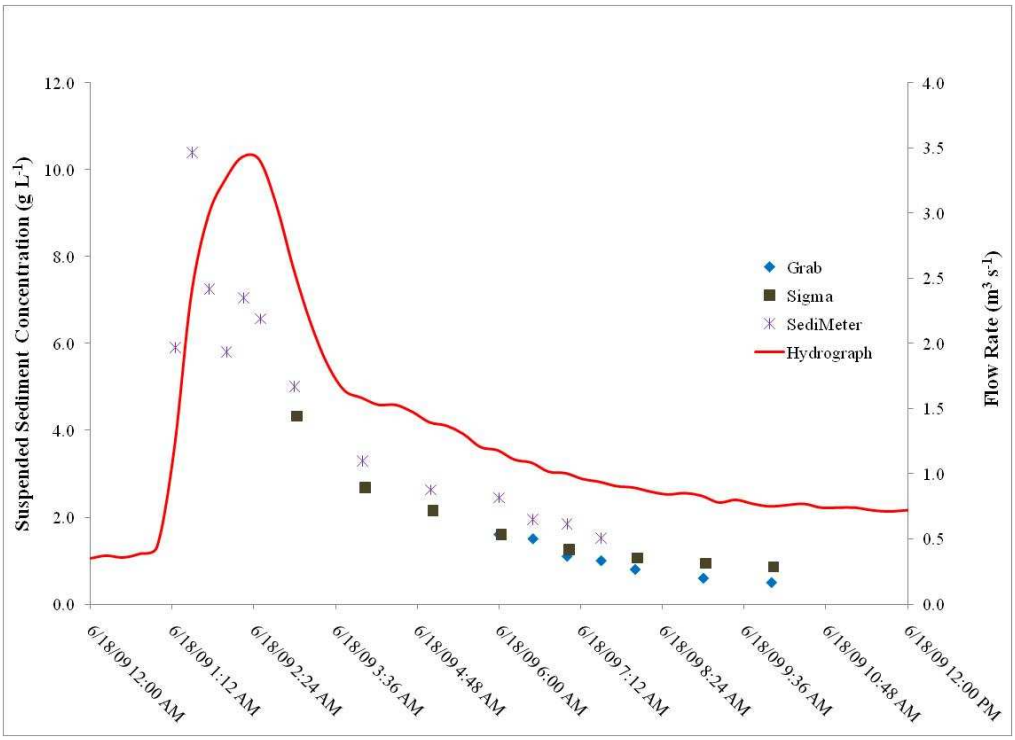

Figure 5.6. Sedigraph for June 18, 2009 event

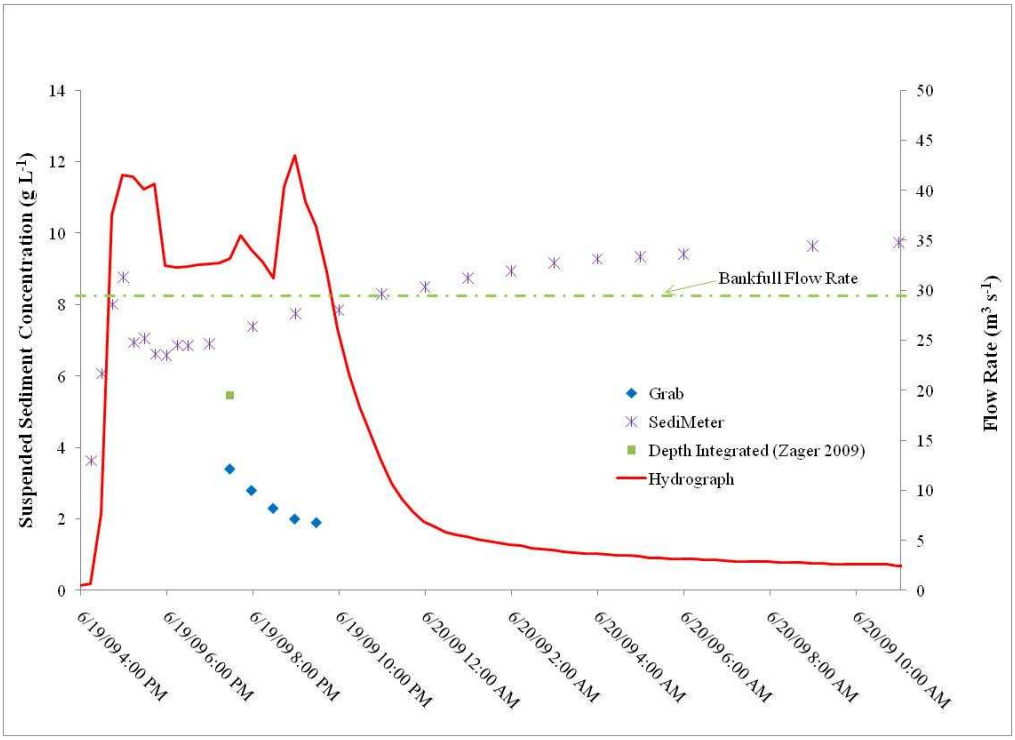

Figure 5.7. Sedigraph for June 19, 2009 event

Figure 5.8. Example of debris level experienced during June 19, 2009 event

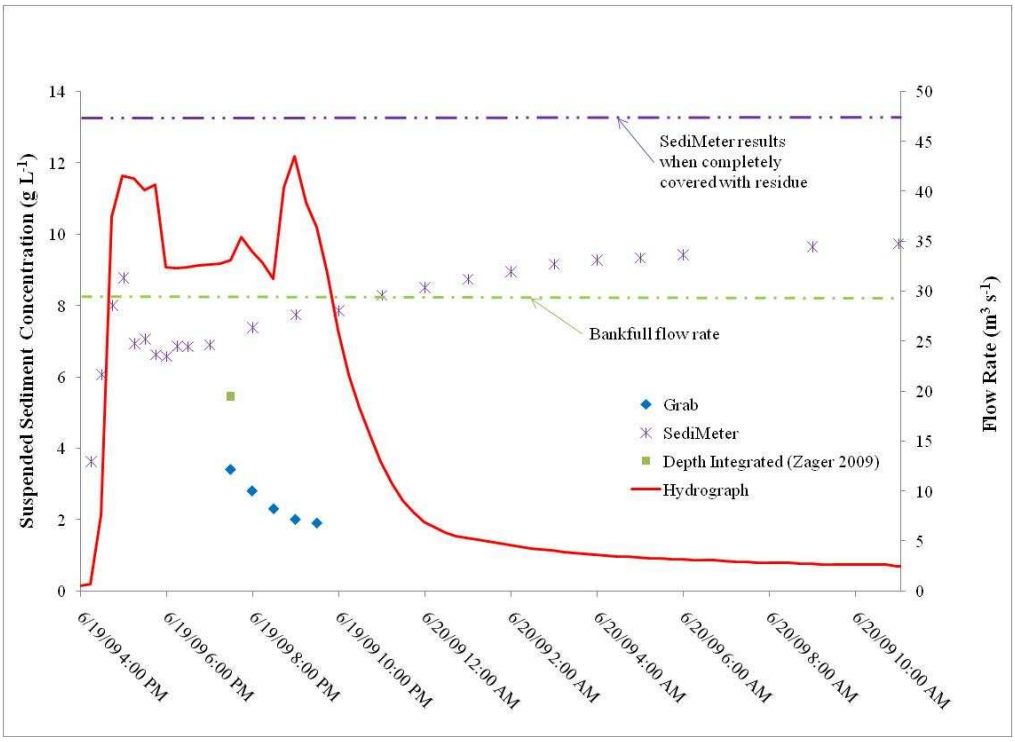

Figure 5.9. SediMeter biofouling results

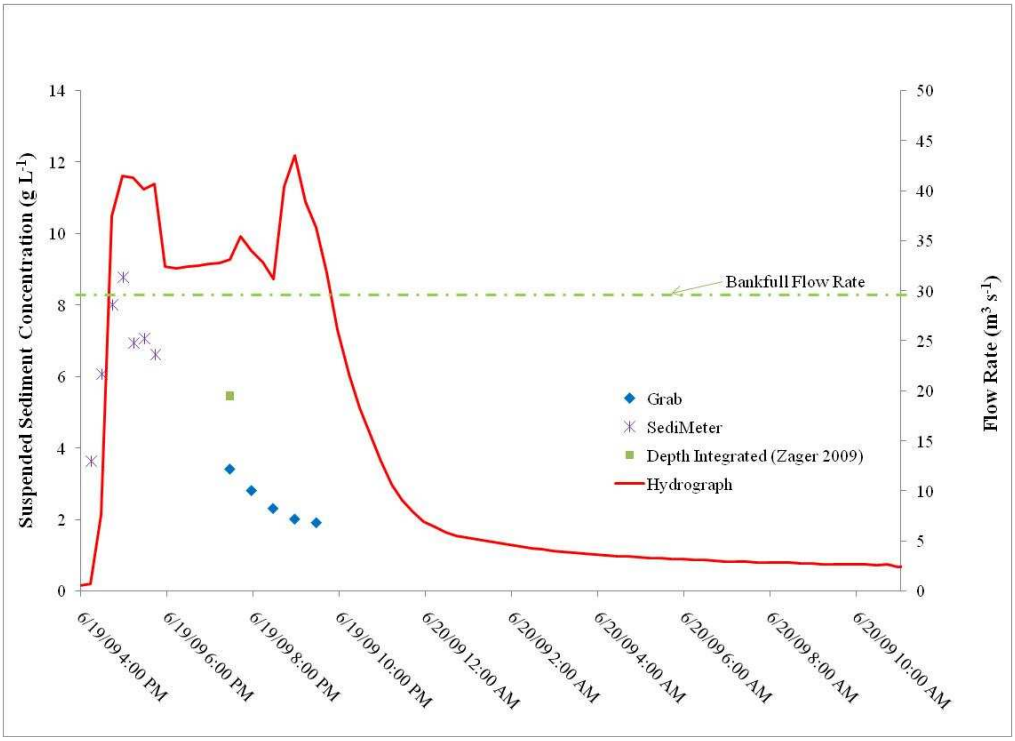

Figure 5.10. Unaffected sedigraph for the June 19, 2009 event

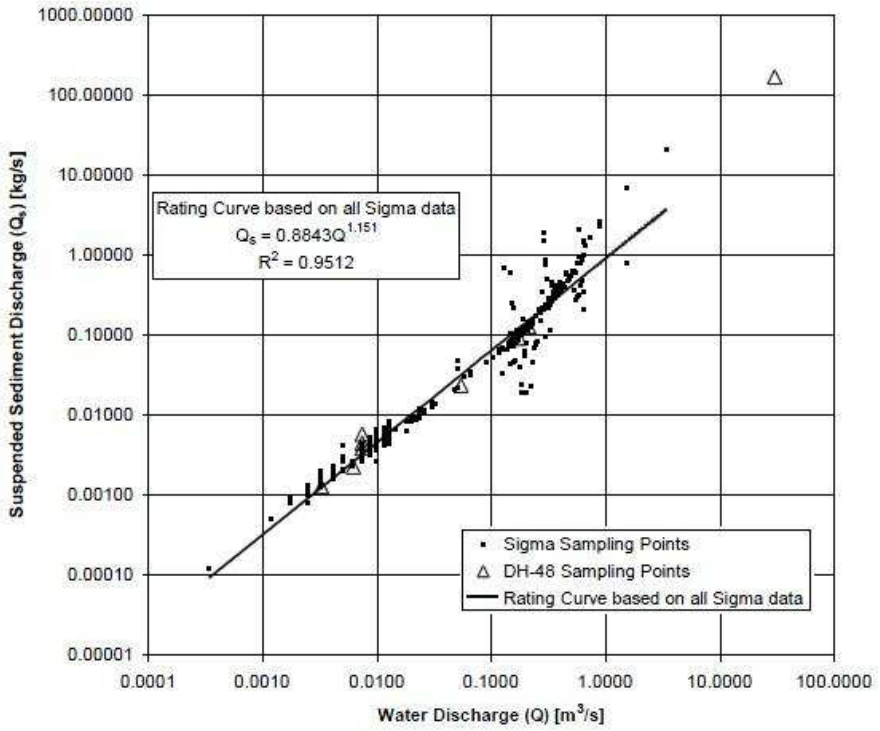

Figure 5.11. Sediment Rating Curve [in collaboration with Zager (2009)]

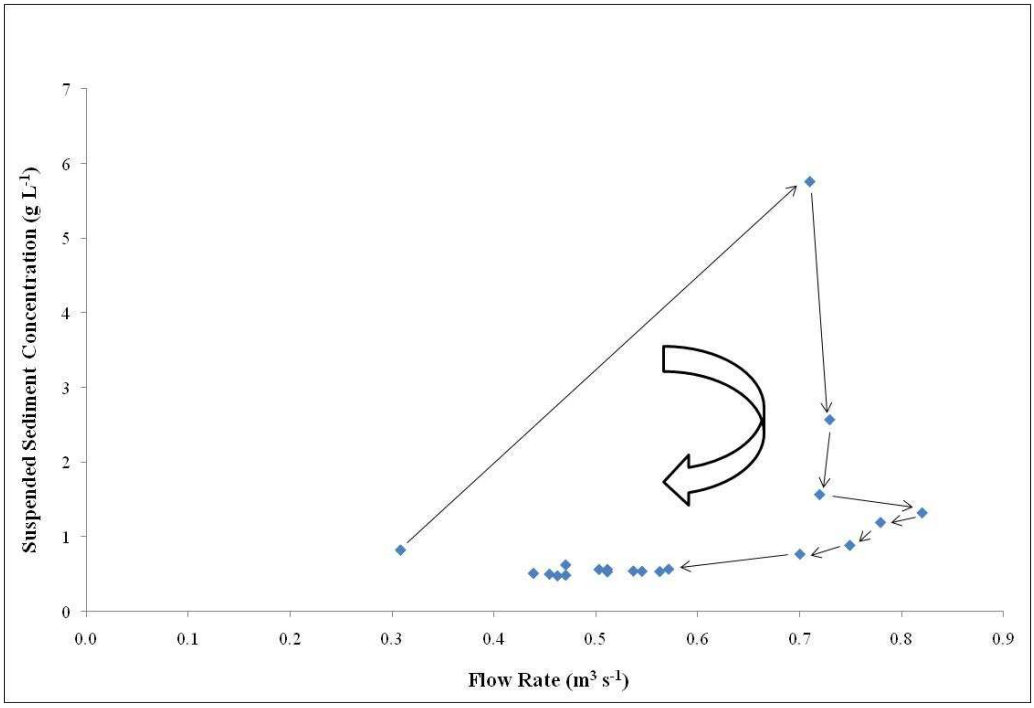

Figure 5.12. Clockwise hysteresis loop for June 16, 2009 event

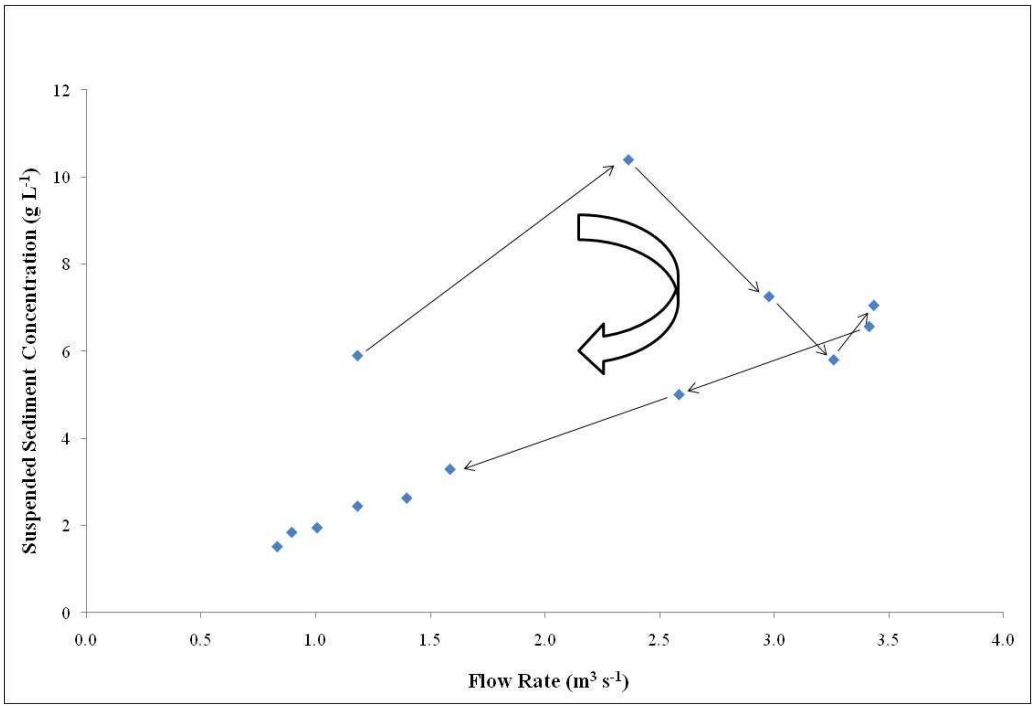

Figure 5.13. Clockwise hysteresis relationship for June 18, 2009 event

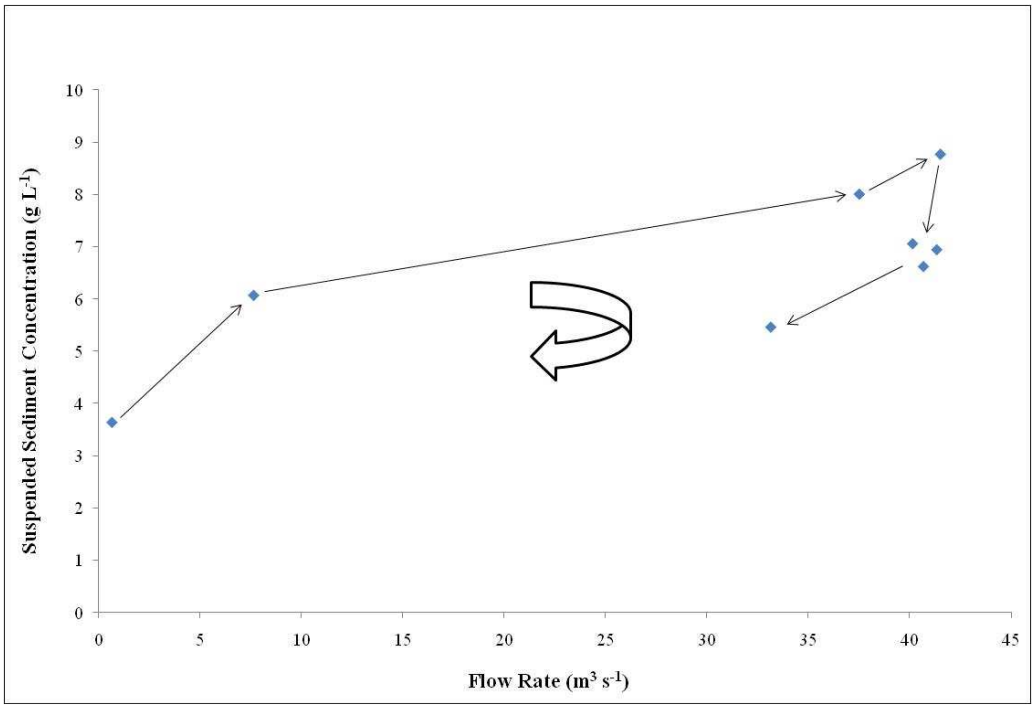

Figure 5.14. Clockwise hysteresis relationship for June 19, 2009 event

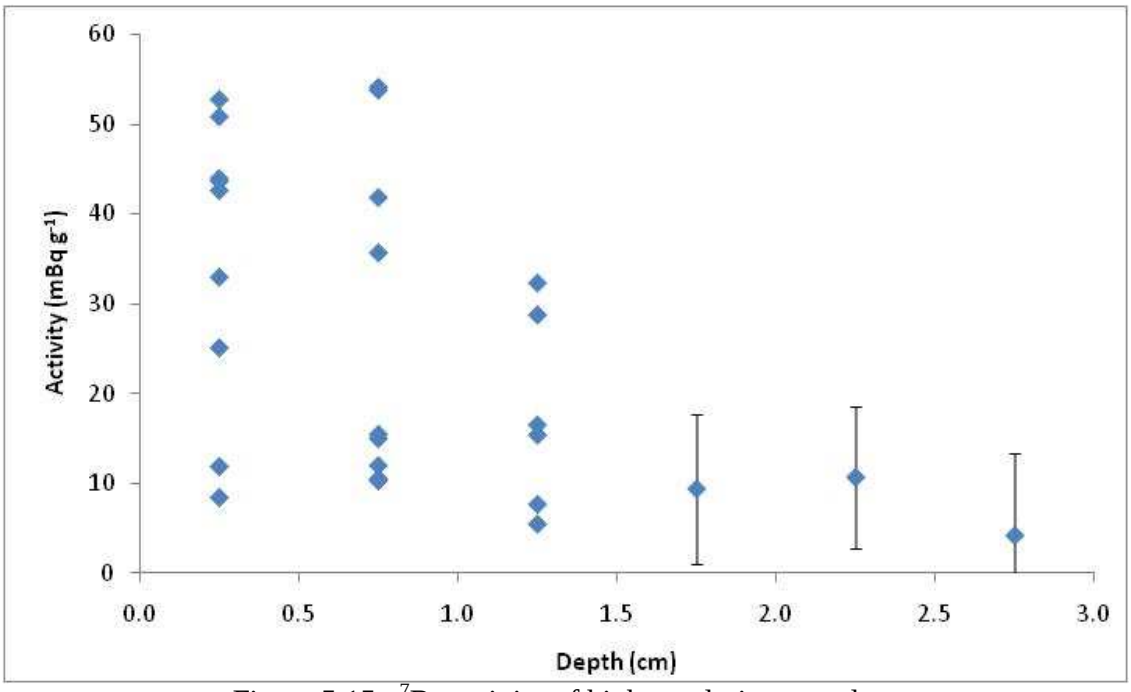

Figure 5.15. ^{7}Be activity of high-resolution samples

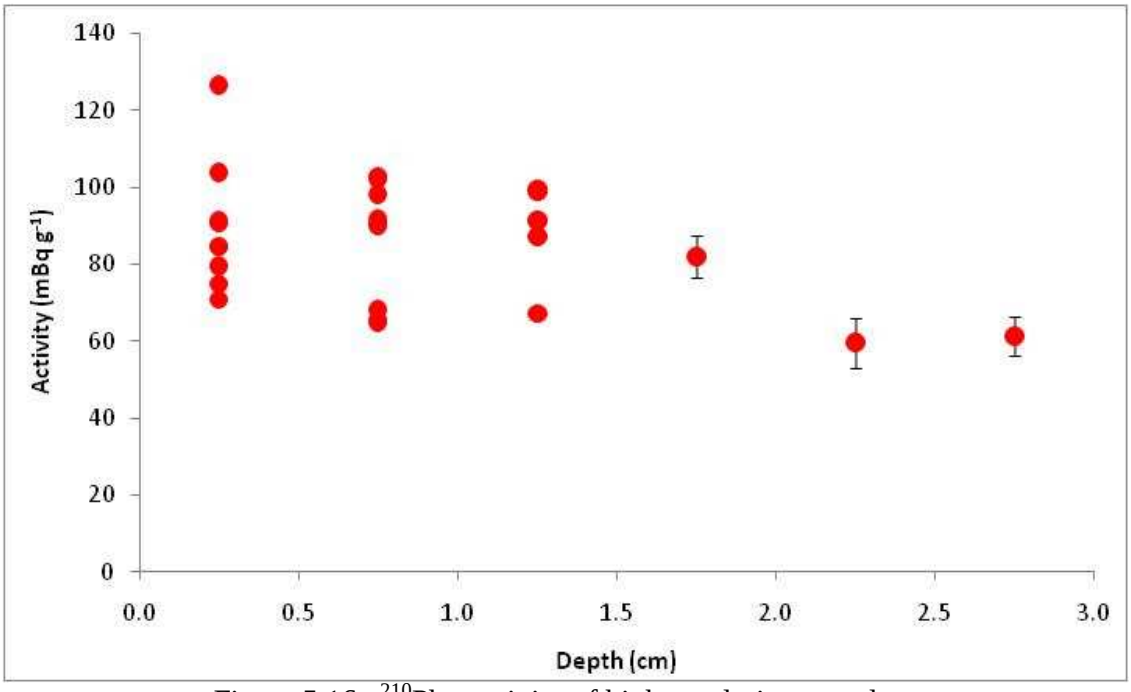

Figure 5.16. $^{210}Pb_{xs}$ activity of high-resolution samples

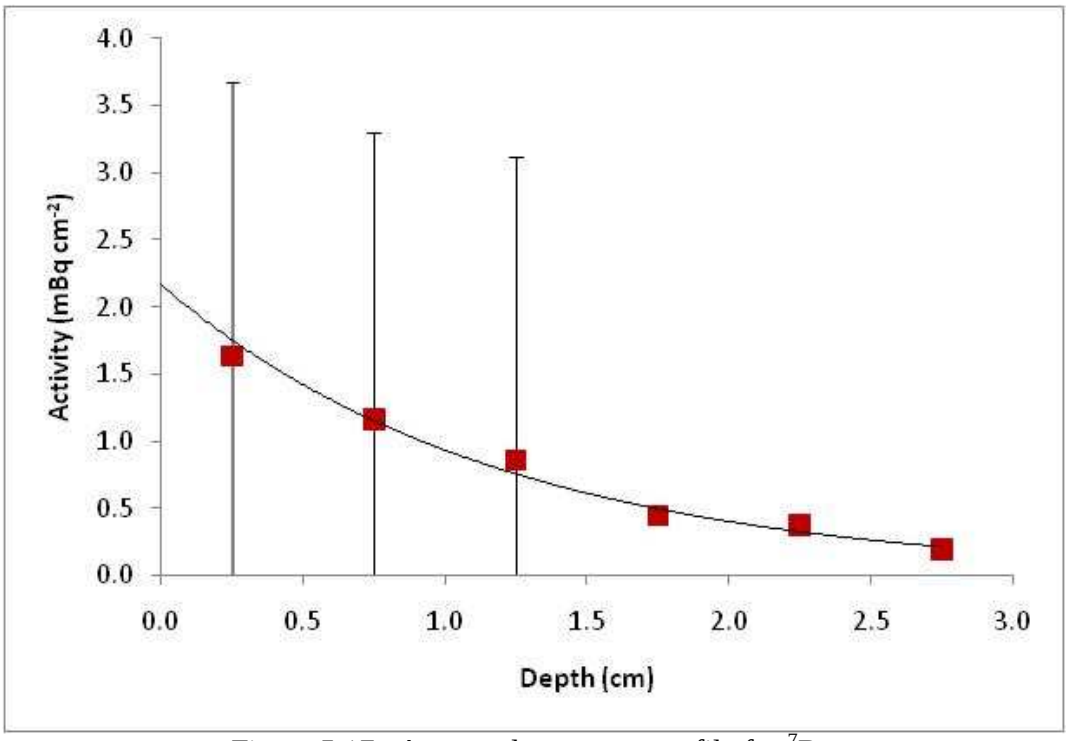

Figure 5.17. Averaged pre-event profile for ^{7}Be

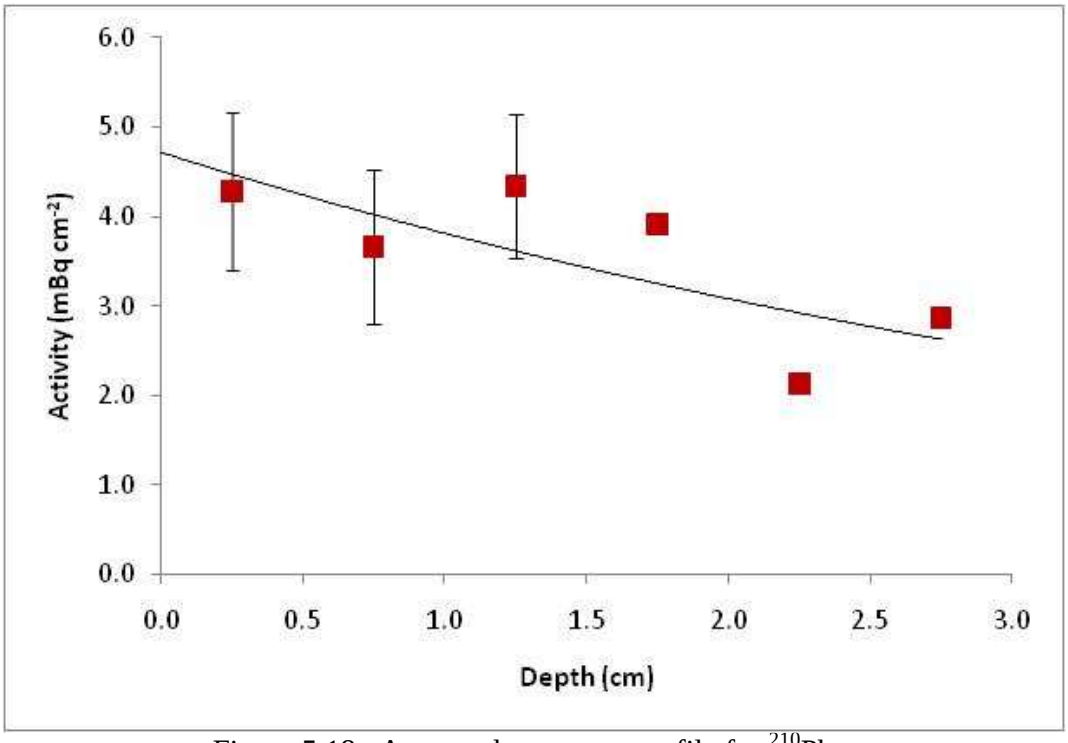

Figure 5.18. Averaged pre-event profile for $^{210}Pb_{xs}$

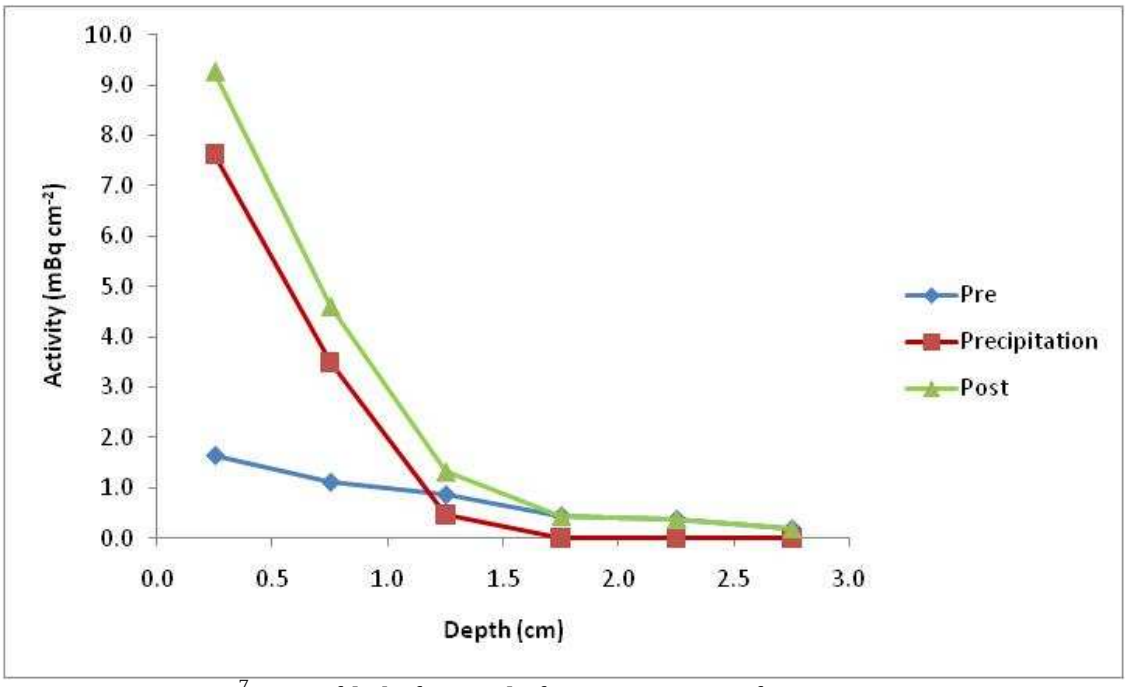

Figure 5.19. ^{7}Be profile before and after precipitation for June 16, 2009 event

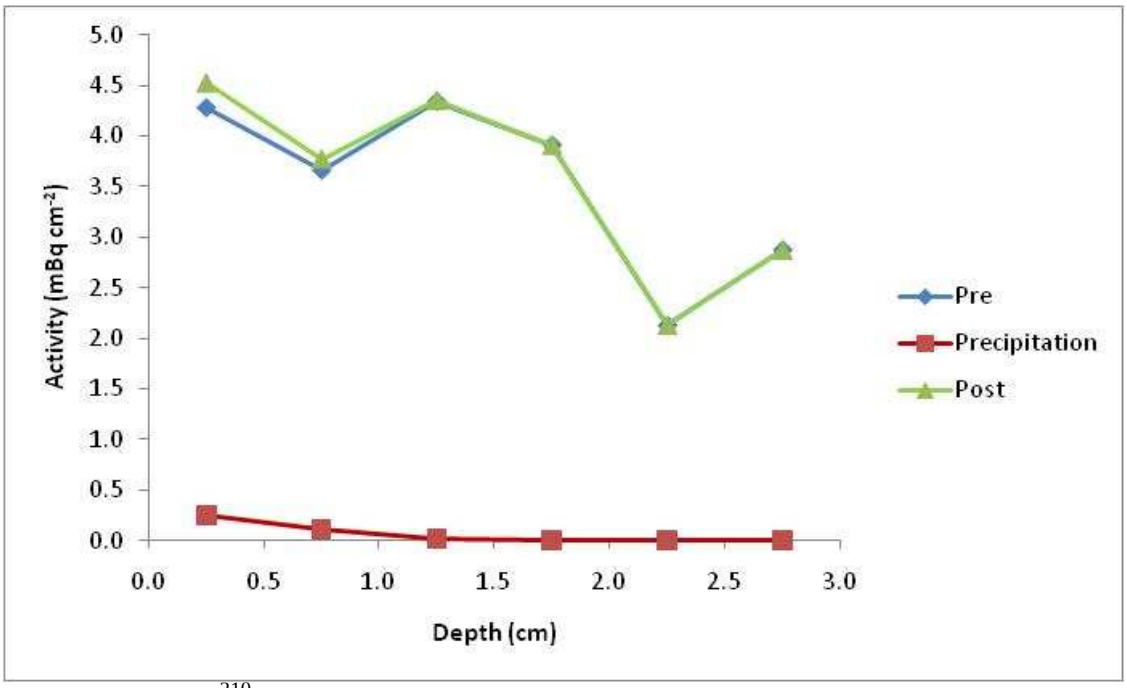

Figure 5.20. $^{210}Pb_{xs}$ profile before and after precipitation for June 16, 2009 event

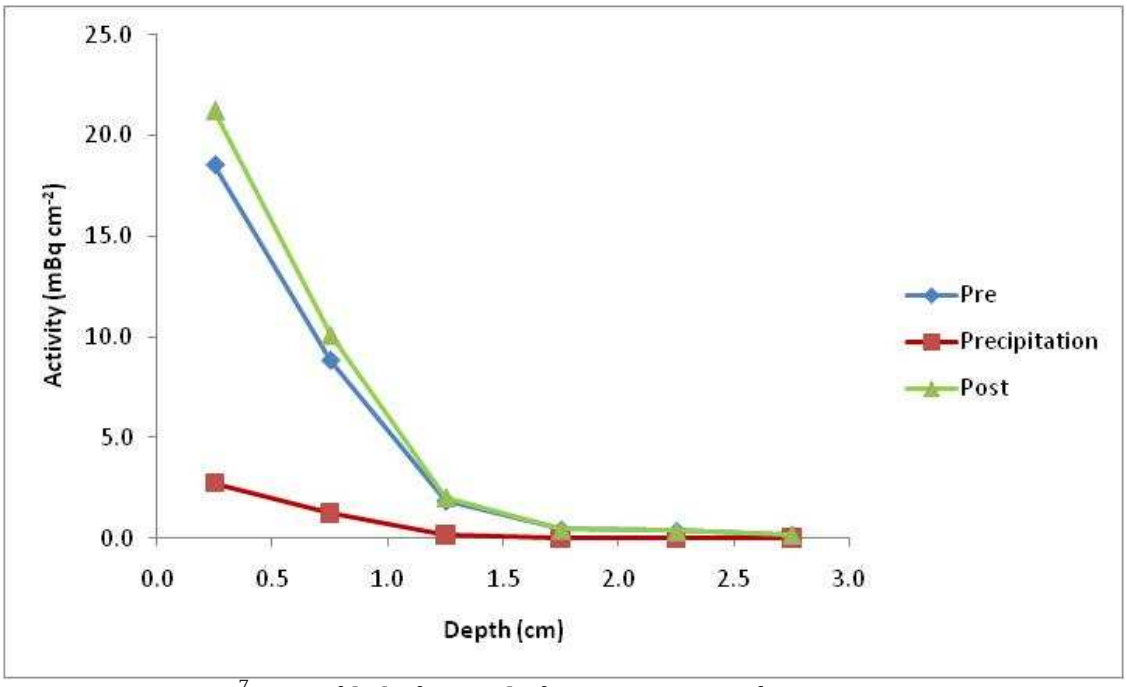

Figure 5.21. ^{7}Be profile before and after precipitation for June 19, 2009 event

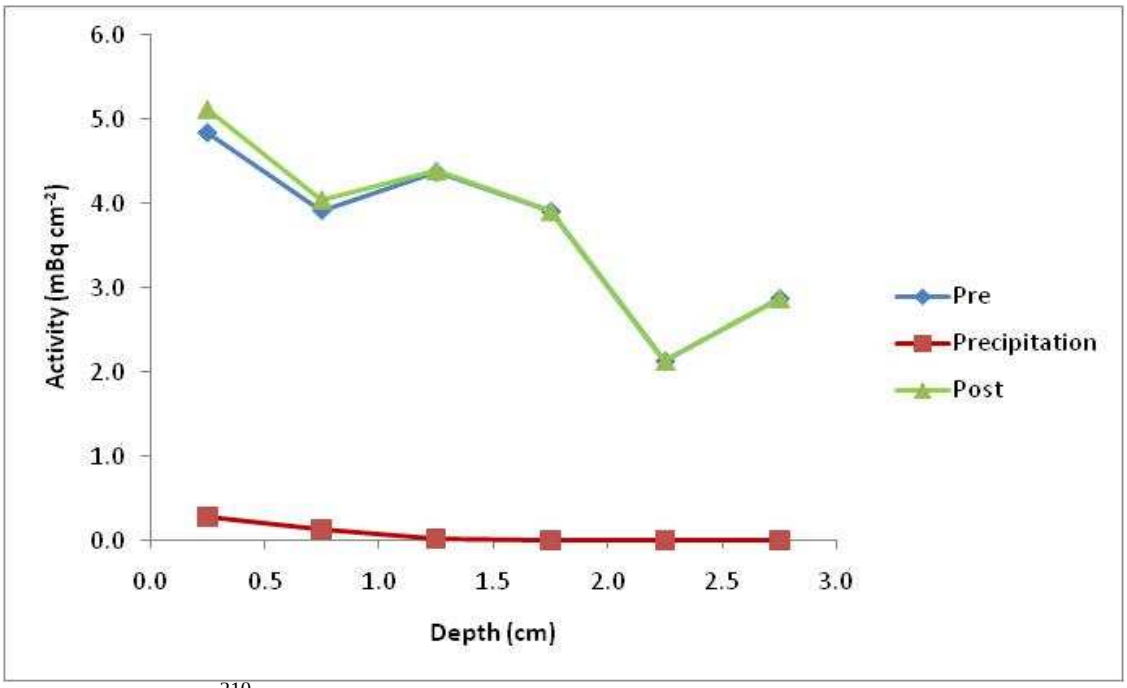

Figure 5.22. $^{210}Pb_{xs}$ profile before and after precipitation for June 19, 2009 event

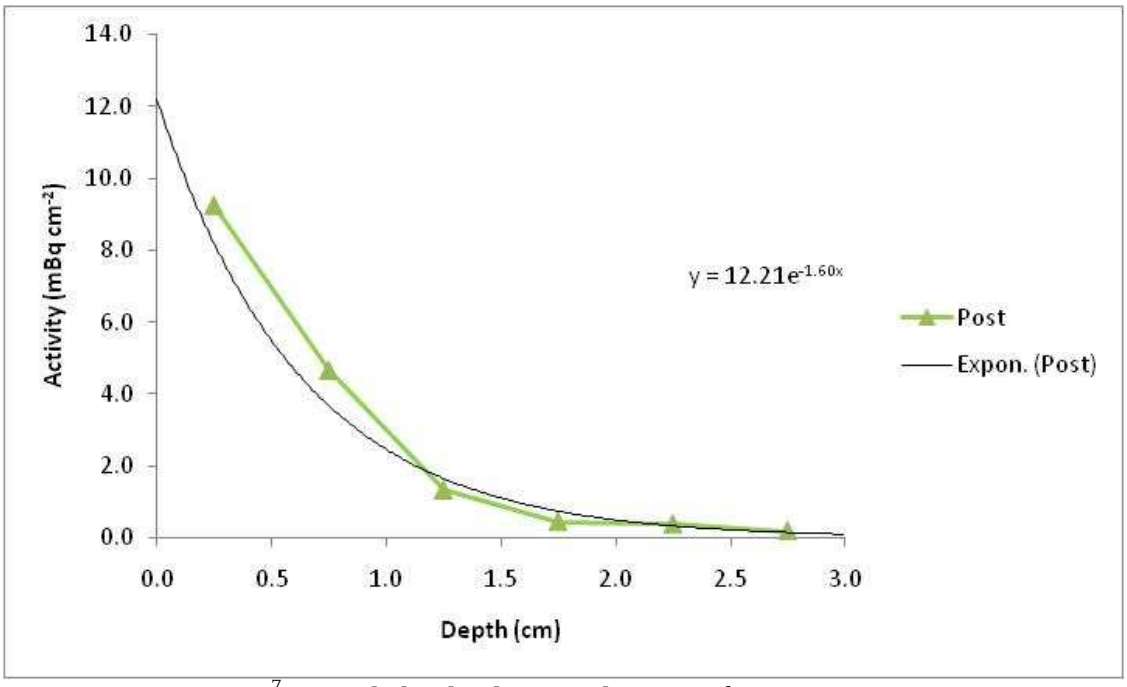

Figure 5.23. ^{7}Be eroded upland material activity for June 16, 2009 event

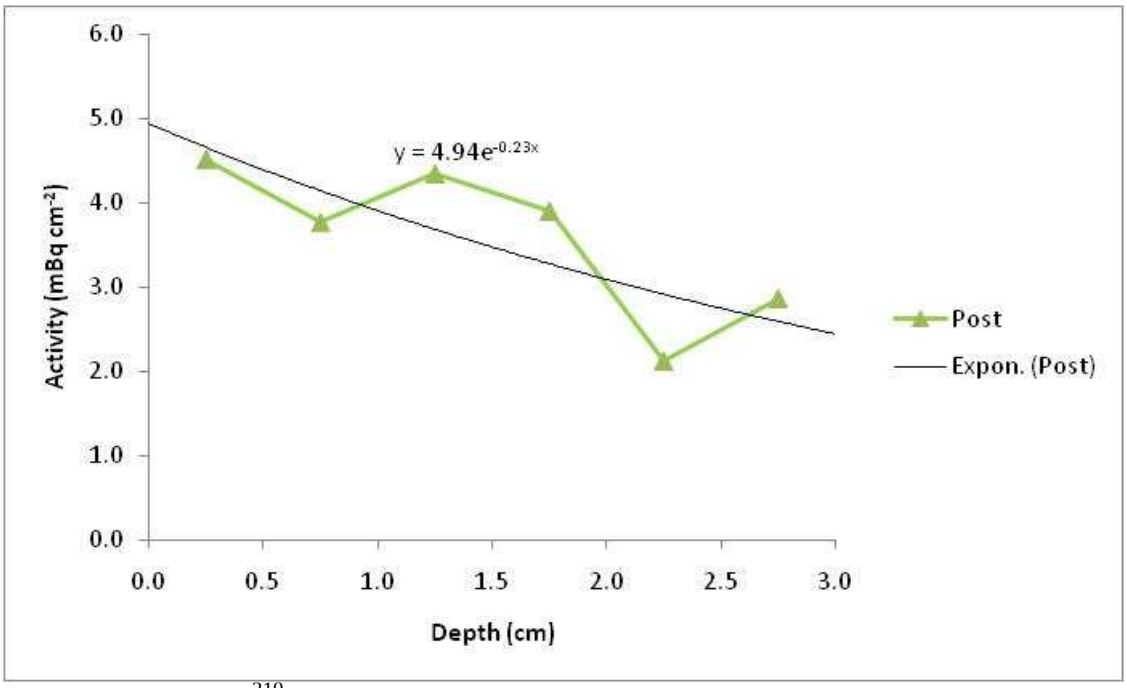

Figure 5.24. $^{210}Pb_{xs}$ eroded upland material activity for June 16, 2009 event

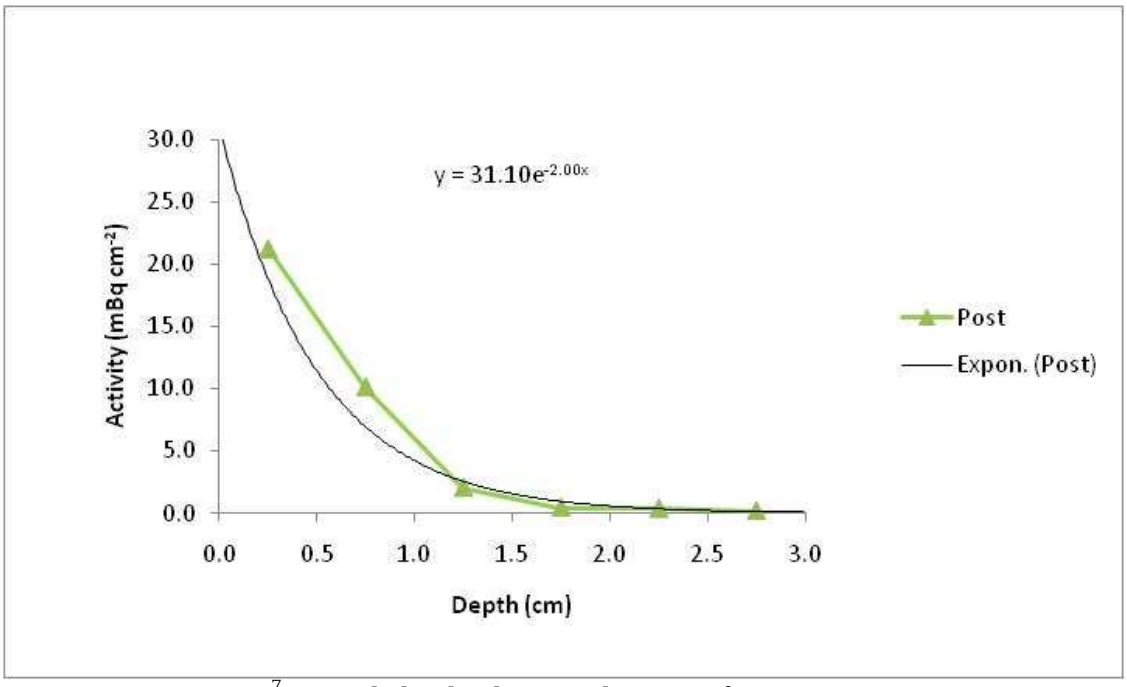

Figure 5.25. ^{7}Be eroded upland material activity for June 19, 2009 event

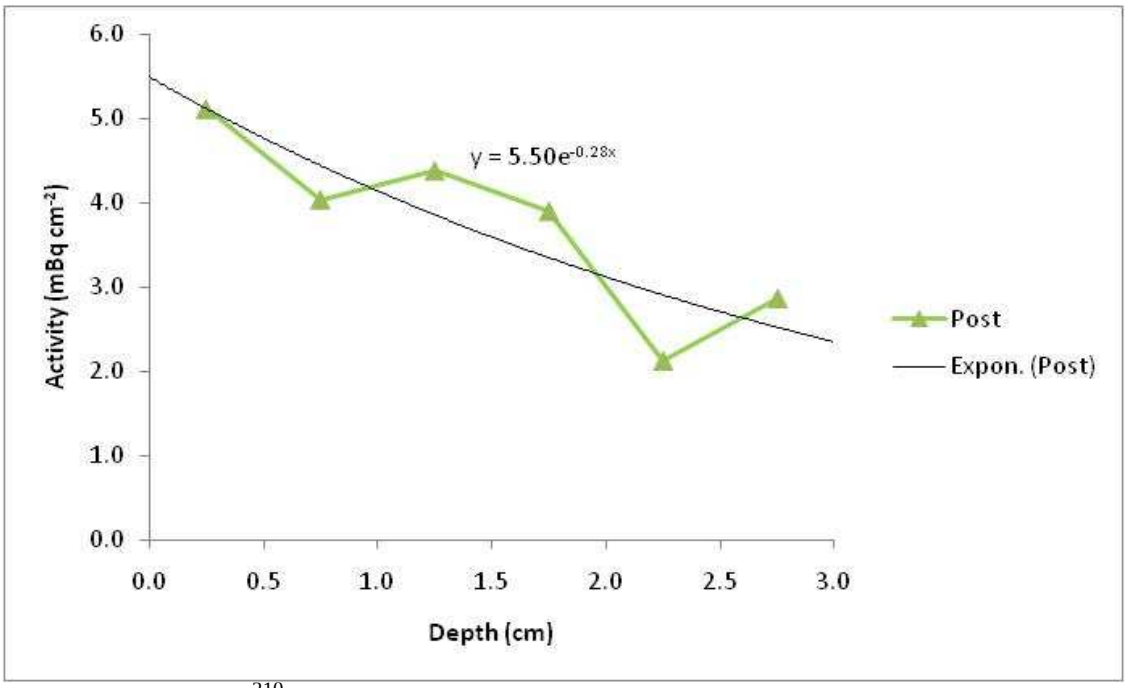

Figure 5.26. $^{210}Pb_{xs}$ eroded upland material activity for June 19, 2009 event

Table 5.2. Average activities of ^{7}Be and $^{210}Pb_{xs}$ in source sediments for Events 1 and 3

Date	Upland Sediments		Channel Sediments	
	^{7}Be Activity (mBq g^{-1})	$^{210}Pb_{xs}$ Activity (mBq g^{-1})	^{7}Be Activity (mBq g^{-1})	$^{210}Pb_{xs}$ Activity (mBq g^{-1})
June 16, 2009	268.1 ± 26.0	108.5 ± 7.9	2.3 ± 18.9	35.1 ± 6.5
June 19, 2009	682.8 ± 26.0	120.8 ± 7.9	2.3 ± 18.9	35.1 ± 6.5

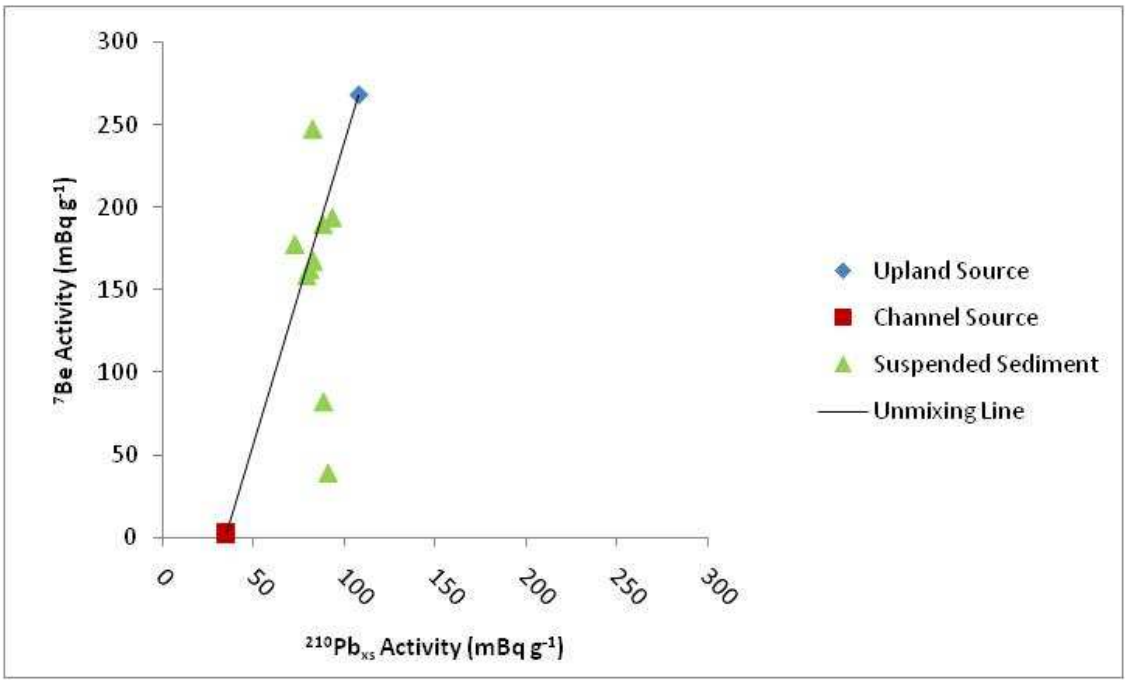

Figure 5.27. Unmixing model for June 16, 2009 event

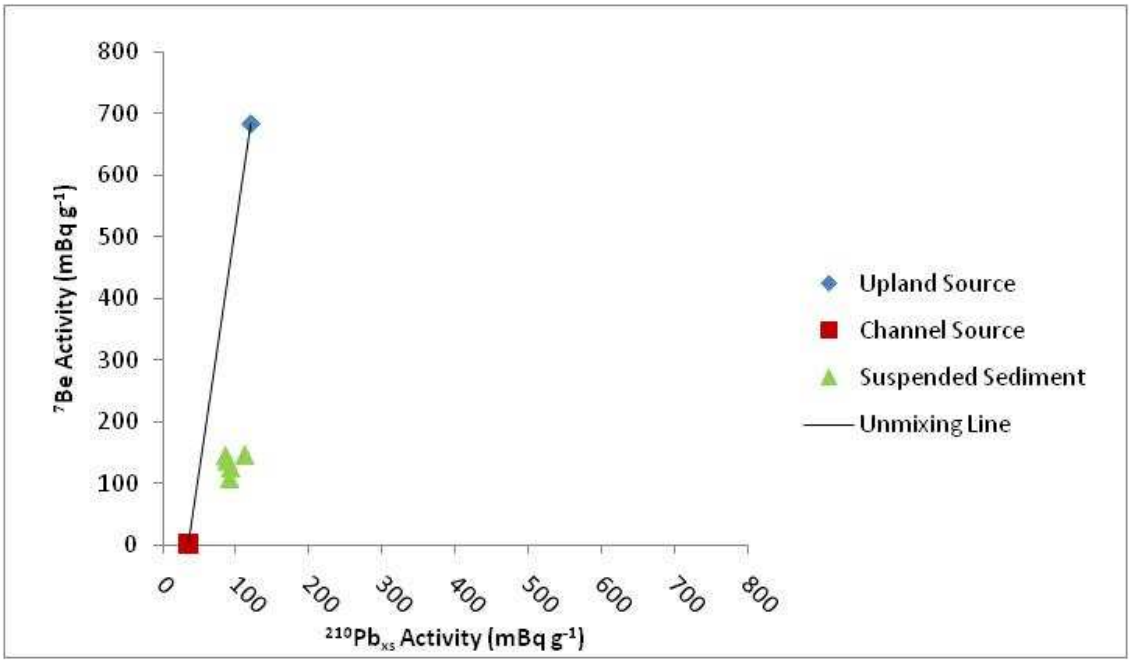

Figure 5.28. Unmixing model for June 19, 2009 event

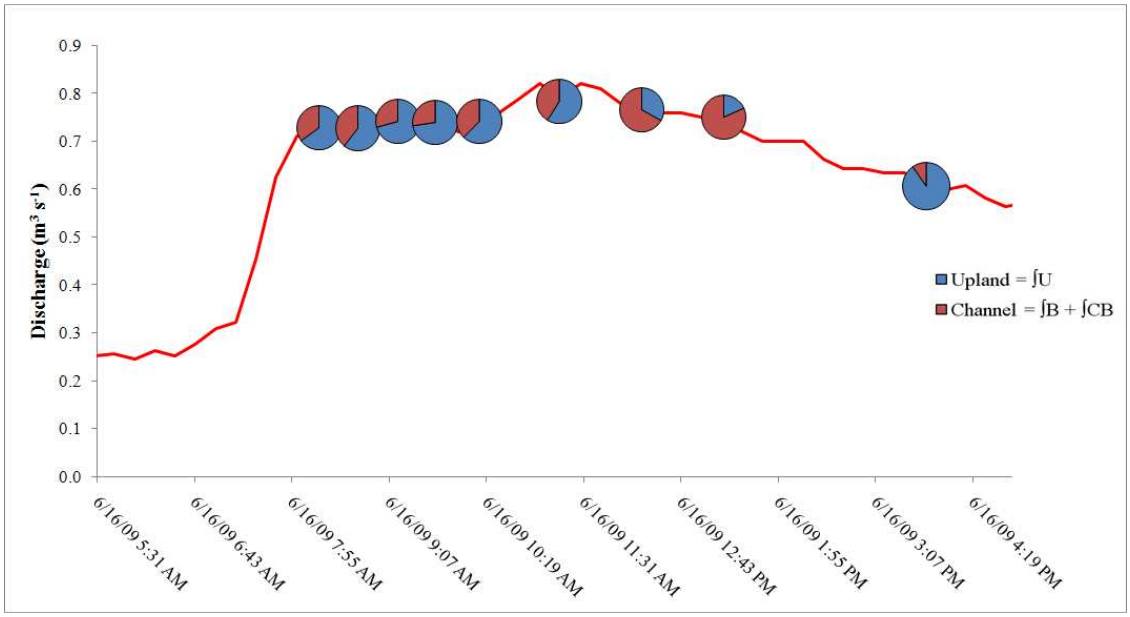

Figure 5.29. Result of the two end-member unmixing model for the June 16, 2009 event

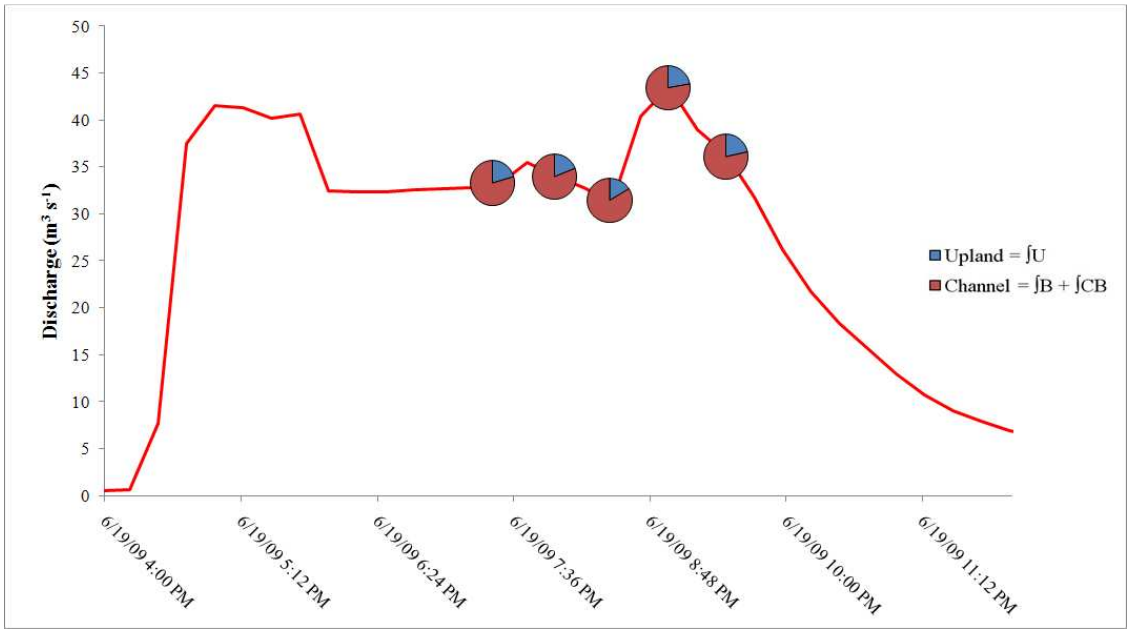

Figure 5.30. Result of the two end-member unmixing model for the June 19, 2009 event

Table 5.3. Proportioning of total load for June 16, 2009 event

Time	Time (s)	C_S (g L^{-1})	Q_W (L s^{-1})	Q_S (kg)	Uplands (U_C) Proportion	Channel (B_C + CB_C) Proportion	Upland Q_S (kg)	Channel Q_S (kg)
8:02		5.8	710					
8:13	720	5.3	730	2793	65%	35%	1816	977
8:43	1800	1.9	730	4728	60%	40%	2860	1868
9:13	1800	2.1	740	2645	71%	29%	1869	775
9:43	1800	1.8	740	2596	73%	27%	1886	710
10:13	1800	1.2	740	1997	62%	38%	1247	750
11:13	3600	0.9	789	2890	59%	41%	1706	1184
12:13	3600	0.8	769	2385	33%	67%	790	1594
Total	-	-	-	20032	61%	39%	12174	7858

Table 5.4. WEPP simulation results

Sediment Yield (g)	Runoff (L)	Concentration (g L^{-1})
3310100	424000	7.8

Table 5.5. Bank contribution results

Total Mass Lost (g)	Total Flow Through Reach (L)	Average B_C (g L^{-1})
3.98E+08	8.63E+08	0.5

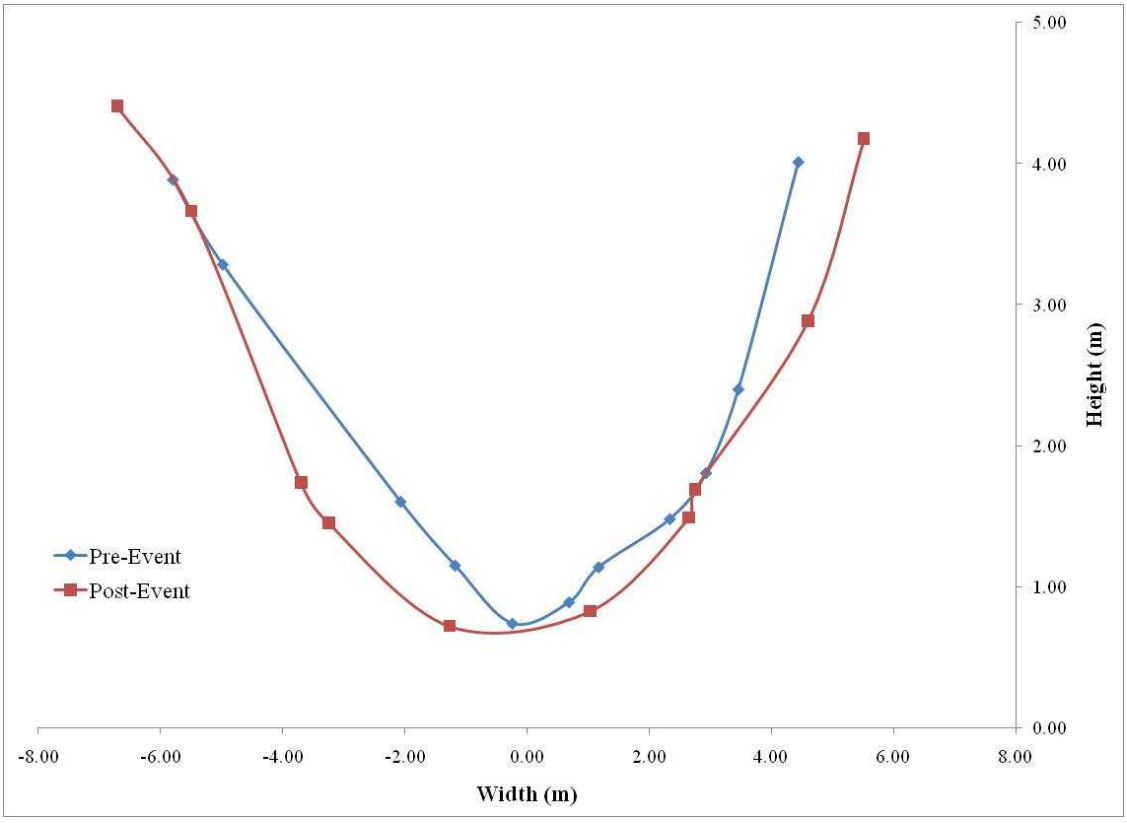

Figure 5.31. Comparison between pre-event and post-even surveys

Figure 5.32. Study reach prior to the June 19, 2009 event

Figure 5.33. Study reach after the June 19, 2009 event

Table 5.6. Variables used in bed resuspension calculation

Variable	Value	Units		Variable	Value	Units
H	2.9	m		ν (15°C)	1.139E-06	$m^2\ s^{-1}$
SG_S	2.65	-		γ_s	25975.7	$N\ m^{-3}$
d_{50}	0.00031	m		g	9.81	$m\ s^{-2}$
X	1.00	-		τ*	9.07	-
U_F	0.0327	$m\ s^{-1}$		q_b	0.0376	$kg\ s^{-1}$
I_1	62	-		d_{65}	0.00038	m
I_2	-98	-		U*	0.2134	$m\ s^{-1}$
Q_W	25.4	$m^3\ s^{-1}$		k_s/δ	30.52	-
AR	10.1	m^2		R	0.93	m
Per	10.9	m		Δ	3.80E-04	m
ρ_w	999.2	$kg\ m^{-3}$		L_a	6.20E-04	m
F	0.56	-		A	2.14E-04	-
S	0.0016	-		κ	0.41	-
τ_0	45.5	Pa		z*	0.374	-
γ	9802.2	$N\ m^{-3}$		C_S	0.3	$g\ L^{-1}$

CHAPTER 6 CONCLUSIONS AND RECOMMENDATIONS

6.1 Conclusions

For this study, the primary objective was to close the sediment budgets for three consecutive high flow events occurring in the South Amana Sub-Watershed (SASW) during June of 2009. Quantitative measurements of suspended sediment concentrations (C_S) and flow rate (Q_W) were collected during the three events to calculate the total sediment flux (Q_S). The suspended sediment load for two of these events were partitioned into sediment contributed from the uplands and sediment contributed from the channel using activities of ^{7}Be and $^{210}Pb_{xs}$, as well as a two end member mixing model.

Events 1 (June 16, 2009) and 2 (June 18, 2009) were moderate in terms of intensity and magnitude for the SASW. Despite the rainfall magnitudes and intensities being similar for the two events, the later event produced higher runoff volumes due to higher antecedent moisture levels in the upland soils. For Event 3 (June 19, 2009), the cumulative rainfall for the event was not extraordinary; however, precipitation intensities for the event were extreme (**sixth** highest 5-minute intensity and the **second** highest 60-minute intensity on record). The excessive rainfall intensities during the event coupled with high antecedent moisture conditions produced a flash flood of Clear Creek in the SASW with flows increasing approximately 4 m in less than1 hour.

Suspended sediment concentrations during the three events were measured using the following three techniques: i) grab samples from the center of the bridge over the SASW outlet during each event, ii) Sigma autosamplers with sampling inlets at 10 and 70 above the stream bed that collected daily measurements during baseflow conditions and hourly during the runoff events, and iii) a SediMeter that collected turbidity

measurements every 15 minutes. Concentration values from the three techniques agreed well despite the differences in operating principles with a maximum percent difference between any of the two techniques for a single sample of only 19%. The SediMeter proved a reliable means of providing continuous measurements during the study period with respect to accuracy. However, biofouling due to the excessive corn stalk debris mobilized during Event 3 produced erroneous suspended sediment measurements.

The total sediment fluxes for Events 1 and 2 were calculated by multiplying the measured values of C_S and flow rate collected during each event. Event 1 produced a total sediment flux of 20,000 kg, while Event 2 produced 200,400 kg. Due to the invalidation of a majority of the suspended sediment measurements for Event 3 (i.e., the SediMeter and the Sigma samples), an accurate estimation of the total sediment load could not be made.

Sediment loads for the three events were also calculated using a sediment rating curve for the SASW outlet (Zager 2009) . The total sediment fluxes for Events 1, 2, and 3 were estimated to be 9,600 kg, 45,700 kg, 1,364,500 kg, respectively. In comparison to the measured values for Events 1 and 2, the sediment rating curve underestimated Q_S due primarily to the non-linear relationship between Q_S and Q_W during high events. Sediment rating curves assume a linear relationship between the variables.

The non-linear relationships between Q_S and Q_W during the three events were displayed through a clockwise hysteresis observed at the SASW outlet. Clockwise hysteresis is often explained as resulting from source material exhaustion. The clockwise hysteresis during Event 3 had a less pronounced discrepancy between the rising and falling limb C_S at the same Q_W (i.e., the hysteresis effect was dampened). The

dampening of the clockwise hysteresis for Event 3 is suggested to result from entrainment of additional upland (specifically floodplain) sediment by overbank flow. Few studies provide data to support the role of overbank flow on the relationship between C_S and Q_W, making this finding unique.

The suspended sediment loads for Events 1 and 3 were further partitioned to determine the relative contributions from the uplands and the channels using the activities of ^{7}Be and $^{210}Pb_{xs}$ using a two end-member unmixing model. The average activities of ^{7}Be and $^{210}Pb_{xs}$ for the eroded upland soils and channel sediment, which were considered the two source end members, plotted at different ends of a graph with the radionuclide activities on separate axes.

The upland source activity was determined from high resolution (0.5-cm intervals) soil profiles collected in four fields in the SASW. The primary mechanisms of erosion in the uplands are sheet and rill erosion, which removes a fine layer of high activity soil. Large spatial variability was exhibited between upland sampling sites; therefore, inventories of each depth interval were pooled to create average radionuclide profiles (Wilson et al. 2003). This variability is a potential source of error. The source activities of the channel sediments were considered to be the integrated activities of the 1-m cores collected along the study reach. Radionuclide contributions from the bed were considered negligible because the bed was comprised mostly of sand particles. Moreover, the atmospheric influxes of the radionuclides varied considerably between the three events, prompting the use of a separate two end-member unmixing model for each event.

The relative contribution of each source (upland and channel) was determined for the suspended sediment of the grab samples collected during Events 1 and 3 using a two end-member unmixing model. The proportion of eroded upland soils was high during the beginning stages of Event 1, while the channel became the dominant contributor to the suspended load near the peak of the hydrograph for Event 1 and on the falling limb of the hydrograph, similar to previous studies (e.g., Wilson et al. 2008). The primary reason for this change in the dominant sediment source was that the upland source quickly became exhausted, as shown with the clockwise hysteresis phenomenon.

Based on field measurements, the total sediment transported during the event (Q_S) was 20,000 kg. Combining the quantitative suspended sediment measurements with the quantitative load partitioning analysis revealed that 61% (12,200 kg) of the total sediment transported during the event was derived from the uplands. The channel source contributed 39% (7,900 kg) with the majority of the channel sediment transported during the falling limb of the hydrograph.

The above quantitative analysis cannot be conducted for Event 3 because no grab samples were collected during the rising limb of the event and the Sigma samples were compromised by overbank flow. However, a qualitative statement in regards to the suspended sediment load partitioning can be made by incorporating the results from event 1 and other studies (Wilson et al. 2008) into the analysis.

The clockwise hysteresis phenomenon that occurred in event 1 also occurred during Event 3. Moreover, similar studies throughout the country have shown that upland contributions are dominant during the rising limb of the hydrograph (Wilson et al. 2008). Thus, it was assumed that the upland was the dominant contributor to the

suspended load during the rising limb of event 3. Further supporting the conclusion that upland contributions remained significant during the later stages of the event was that the overbank flow provided additional upland sediment to the suspended load, as exhibited by the dampened hysteresis phenomenon.

Verification of this conclusion was completed using a variety of methods unique to each component. The upland component was established using the Water Erosion Prediction Project (WEPP) model; the channel bank component was determined using cross-sectional surveys; the channel bed component was computed using the Einstein approach (Einstein 1950). The average suspended sediment concentration of material eroding from the uplands was predicted to be 7.8 g L^{-1} by WEPP, which was greater than the average bank and bed contributions over the course of the event, which were 0.5 g L^{-1} and 0.3 g L^{-1}, respectively.

The knowledge gained from this study provides three principal benefits to watershed managers. Firstly, an important consideration for watershed managers is the prediction of annual sediment loadings. This study revealed that rating curves can vastly under-predict sediment loadings during high-flow events, in which a majority of the annual sediment load is transported. Secondly, this study also showed that the uplands were the dominant contributor of sediment to the total event suspended sediment load in the headwaters of an agricultural watershed. Therefore, watershed managers maintaining watersheds similar to the SASW should focus on enacting conservation practices aimed at reducing erosion from the uplands. Thirdly, the methods used in this study can be utilized by watershed managers to close sediment budgets in their watershed. The sampling techniques used in this study are relatively inexpensive and easy to operate. In

addition, the radionuclide tracing method has been shown to effectively differentiate sediment from multiple source areas.

Ultimately, this study has demonstrated the complimentary use of tracing methods with intra-event C_S and Q_W measurements to close the sediment budget. This approach advances existing sediment budget studies by partitioning the source of transported sediment and accounting for the role of hysteresis on sediment flux variability.

6.2 Recommendations

This study showed that the uplands were the dominant contributor to the suspended load in the early stages of the sampled runoff events. However, more quantitative conclusions were not made due to gaps in the data resulting primarily from sampling deficiencies. Two specific recommendations, stated below, are made to correct for these deficiencies.

Firstly, an improved version of the SediMeter sampler is needed. This improved version should incorporate a self-cleaning attachment to limit the effects of biofouling. Had biofouling of the sampler not occurred during the June 19, 2009 flash flood event, additional rare data could have been collected.

Secondly, future studies should sample from more than one depth in order to quantify suspended sediment transport more accurately. This is important in the determination of both suspended sediment flux and in the tracer study. Sampling only a small fraction of the water column, especially during extreme events, may misrepresent depth-averaged suspended sediment concentrations. Point sampling may also selectively sample suspended material originating from one source, resulting in erroneous source identifications.

APPENDIX A SEDIMETER

The SediMeter by Lindorm (Figure 4.4) is designed to provide an *in situ* suspended sediment concentration profile for aquatic environments. The SediMeter consists of 36 laser emitting diodes (LED), spaced at 10-mm intervals along a vertical rod (Figure 4.5). Each LED emits a pulse of near infrared (NIR) light into the flow; light is reflected back to the LEDs by sediment particles in suspension. The amount of light reflected back to the LED relates to the turbidity of the water, which in turn relates to suspended sediment concentrations (Pruitt 2003). This measurement technique is known as optical backscatterance.

The optical backscatterance technique used by the SediMeter requires that the instrument undergo a calibration process in order to record suspended sediment measurements accurately. Calibration of the SediMeter is a two-step process, which involves: i) determining the appropriate coefficients to convert the reflectance (in volts) to a turbidity value (Formazin Backscatter Units, FBU) and ii) converting the turbidity value to a suspended sediment concentration. The goal of this Appendix is to detail the calibration process for the instrument. In addition, this Appendix will outline the installation process of the instrument into riverine environments.

A.1 SediMeter Calibration

Understanding the underlying calculations used by the SediMeter software is the first step in the SediMeter calibration. The software solves six formulas that utilize five different calibration-determined coefficients to convert the reflectance (in volts) to turbidity (in FBU). The following generic equation is used to determine the turbidity of the water column in any situation (dark or light, turbid or clear water):

$$FBU = K_{sm}(U_{on} - A_{sm} - U_{adj}) \quad \text{A.1}$$

where K_{sm} is the factor used to convert a corrected voltage (RAW) to FBU and is found using Equation A.2, U_{on} is the voltage recorded by the SediMeter sensor when the NIR light is emitted, A_{sm} is the voltage recorded by the SediMeter when the LED is on and the instrument is deployed in clear water, with no ambient infrared (IR) light and no reflector within several decimeters, and U_{adj} is the adjusted voltage and found using Equation A.3.

$$K_{sm} = \frac{T_b}{RAW} \quad \text{A.2}$$

where T_b is the turbidity of calibration solution used to determine K_{sm} and RAW is the signal after correction for internal reflections and background light (see Section A.1.2 for further information).

$$U_{adj} = B_{sm}(U_{amb}) - C_{sm}(U_{amb})^2 \quad \text{A.3}$$

where $B_{sm} = 1$ and $C_{sm} = 0$ as recommended by the SediMeter Software Manual, and U_{amb} is the voltage added by the ambient light and is equal to:

$$U_{amb} = U_{off} - U_{dark} \quad \text{A.4}$$

where U_{off} is the voltage recorded when the SediMeter sensor is not emitting light and D_{sm} is the voltage recorded by the SediMeter when the LED is off and no ambient IR light present (e.g., the background voltage in darkness).

Therefore, Equation A.3 simplifies to:

$$U_{adj} = U_{off} - D_{sm} \quad \text{A.5}$$

Substitution of Equation A.5 into Equation A.1 yields Equation A.6, which is used by the SediMeter software to convert the U_{on} and U_{off} measurements to FBU:

$$FBU = K_{sm}[U_{on} - A_{sm} - (U_{off} - D_{sm})] \quad \text{A.6}$$

The calibration coefficients in Equation A.6 are determined through a systematic calibration process. The following subsections outline the steps necessary to determine coefficients A_{sm}, D_{sm}, and K_{sm} and validate the B_{sm} and C_{sm} assumptions.

A.1.1 Systematic Determination of Coefficients A_{sm} & D_{sm}

Coefficients A_{sm} and D_{sm} are used to determine the voltage returned to each sensor while the LED light is and is not on, respectively. Thus, subtraction of D_{sm} from A_{sm} removes the effect of ambient light on the readings. Each of the 36 sensors must be manually calibrated due to minor variations sensor sensitivity. The graphical user interfaces for SediMeter control (Figure A.1) and data analysis (Figure A.2) were used to complete this process. The following list outlines the methods used to determine A_{sm} and D_{sm} for each sensor.

1) Fill a container with deionized water. The container should be large enough that when the LED light on the SediMeter flashes, reflections will be minimal. A 30-gallon trashcan, filled with about 100 liters of water is sufficient.

2) Connect the SediMeter to a computer using the USB cord.

3) Select the correct Serial Port to which the SediMeter was connected in the Connection tab.

4) Click the button under the title ‘Open Connection’.

5) Specify the time at which to begin logging data and the interval at which data should be collected in the Setup tab. Note that the time is in GMT when setting the logging time and that the minimum interval is one minute. Any interval entered into the program that is less than one minute will still record data only once per minute. Click the ‘Set’ button once finished to transfer the settings to the SediMeter.

6) Change the mode in which the SediMeter is set to LOG mode in the Special tab. Click the ‘Set’ button once finished.

7) Close the connection by clicking on the button below the ‘Open Connection’ title in the Connection tab.

8) Unplug the USB cord from the SediMeter and insert the cap back into the

SediMeter.

9) Insert the SediMeter sensor into the protective tube. Tighten the yellow screw to fix the protective tube on the SediMeter.

10) Insert the SediMeter into the water in the trashcan.

11) Shut all lights in the room off and minimize ambient light.

12) Let the SediMeter record a few measurements (3 to 4) before turning the lights back on and removing the SediMeter from the trashcan.

13) Connect the SediMeter to the computer.

14) Change the mode in which the SediMeter is set to SLEEP in the Special tab. This will stop the SediMeter from recording any more measurements. Click the 'Set' button once finished.

15) Specify the file path to which the data will be downloaded in the Download tab. Click 'Get New' to download all new records, or 'Get All' to download both new and old records. Close the window that pops up (or Ctrl+W); for this procedure, the window only confirms that the data was downloaded.

16) Select 'Analyze Logged' from the Data dropdown menu (or Ctrl+A).

17) Select the SediMeter network identifier number from the SediMeter NetAddr drop down box on the right side of the SediMeter Data window. This must be done to refresh the graphs to display the downloaded data.

18) Select U_{on} from the SediMeter Variable drop down list.

19) Right click on the green cursor on the upper yellow box on the right side of the SediMeter Data Window. Click 'Bring to Center'. This will bring the cursor into the center of the SediMeter Backscatter Intensity plot. The upper yellow box is used for the SediMeter Backscatter Intensity graph, while the lower yellow box is used for the Data Plot graph.

20) Move the mouse pointer over the cursor on the SediMeter Backscatter Intensity graph. Click on the cursor and while holding the button down, drag the mouse. This will allow for adjustment of the (x,y) position of the cursor. Note that when moving the SediMeter Backscatter Intensity graph cursor, the numbers in the upper yellow box change.

21) Line the cursor up with the time that will be used as the calibration time. The author randomly used data from the second measurement as the calibration time.

22) In the upper yellow box, edit the detector number from which you wish to obtain the U_{on} value by changing the number from 0 to 35. Detector 1 corresponds to 0 in the yellow box, detector 2 corresponds to 1 in the yellow box, etc. Please note that time cannot be edited. If attempting to edit the time, an error will occur and the program will close.

23) Record the U_{on} values from each sensor in a spreadsheet. Thirty-six different numbers should be recorded. When the turbidity of the solution is zero (the case in this situation), the value of the A_{sm} coefficient is equal to the U_{on} value.

24) Ensure the correct values for the A_{sm} coefficient have been obtained by repeating Steps 2 - 23 two or three additional times and taking the average of the U_{on} (i.e., A_{sm}) values for each detector.

25) Select U_{off} from the SediMeter Variable drop down list.

26) Record the U_{off} values from each detector in a spreadsheet. The values should be small (approximately 0.001). When the turbidity of the solution is zero (the case in this situation), the value of the D_{sm} coefficient is equal to the U_{off} value.

27) Table A.1 displays the A_{sm} and D_{sm} coefficient values obtained by the author when completing this portion of the calibration.

28) Create a .txt document in which the A_{sm} values are incorporated into the document. This document, called a KABC table, will be used in Section A.1.2. The document should have 36 rows (one for each detector) and be formatted in the following format: Column 1 = K_{sm} value (for this step, and only this step, set all K_{sm}values equal to the default value of 6820), Column 2 = A_{sm} (insert values obtained from Step 24), Column 3 = B_{sm} (set equal to 1, see discussion in Section A.1.3 for details), and Column 4 = C_{sm} (set equal to 0, see discussion in Section A.1.3 for details). Table A.2 displays the tab-delimited file used by the author.

A.1.2 Systematic Determination of Coefficient K_{sm}

Coefficient K_{sm} is the factor used to convert RAW to FBU; K_{sm} is inversely proportional to the RAW value (see Equation A.2). RAW is affected by the A_{sm} coefficient; therefore, A_{sm} must be determined as stated in Section A.1.1 before finding RAW. The graphical user interfaces for SediMeter control (Figure A.1) and data analysis (Figure A.2) were used to find RAW. The following steps are used to determine K_{sm}.

1) Obtain a 2-foot long, 3-inch inside diameter PVC tubing (with an end cap sealed on one end). The interior of the tubing must be painted black.

2) Place the tubing in a bucket and fill around the tube with sand or some other material to keep the tube vertical.

3) Fill the tubing with 2.5 L of formazin solution. If using the protective outer tube on the SediMeter, ensure that the concentration of the formazin solution is at least 1000 NTU. The author created this solution by adding1.5 L of deionized water to 1 L of 4000 NTU formazin solution. This diluted formazin solution had a turbidity of 1600 NTU.

4) Connect the SediMeter to a computer using the USB cord.

5) Select the correct Serial Port to which the SediMeter was connected in the Connection tab.

6) Click the button under the title 'Open Connection'.

7) Specify the time at which to begin logging data and the interval at which data should be collected in the setup tab. Note that the time is in GMT when setting the logging time and that the minimum interval is one minute. Any interval entered into the program that is less than one minute will still record data only once per minute. Click the 'Set' button once finished to transfer the settings to the SediMeter.

8) Change the mode in which the SediMeter is set to LOG mode in the Special tab. Click the 'Set' button once finished.

9) Close the connection by clicking on the button below the 'Open Connection' title in the Connection tab.

10) Unplug the USB cord from the SediMeter and insert the cap back into the SediMeter.

11) Insert the SediMeter sensor into the protective tube. Tighten the yellow screw to fix the protective tube on the SediMeter.

12) Insert the SediMeter into the water in the PVC tube.

13) Shut all lights in the room off and minimize ambient light.

14) Let the SediMeter record a few measurements (3 to 4) before turning the lights back on and removing the SediMeter from the PVC tube.

15) Connect the SediMeter to the computer.

16) Change the mode in which the SediMeter is set to SLEEP in the Special tab. This will stop the SediMeter from recording any more measurements. Click the 'Set'

button once finished.

17) Specify the file path to which the data will be downloaded in the Download tab. Click ‘Get New’ to download all new records, or ‘Get All’ to download both new and old records. Close the window that pops up (or Ctrl+W); for this procedure, the window only confirms that the data was downloaded.

18) Select ‘Calibration Coefficients’ from the Edit drop down menu of the SediMeter Control window.

19) Select ‘Import KABC table’ from the File drop down menu of the newly opened SediMeter Calibration Coefficients window (Figure A.3).

20) Navigate to the KABC table saved in Section A.1.1, Step 28. Select the KABC file and click OK.

21) Click the arrow symbol >> to load the calibration coefficients into the software program.

22) Ensure that the coefficients were loaded by clicking the << symbol. If the numbers in the KABC table stay the same, the coefficients were successfully loaded.

23) Edit the D_{sm} Calibration Coefficient on the right side of the SediMeter Calibration Coefficients window. For the author, all D_{sm} coefficient values equaled 0.001. Therefore, 0.001 was entered into all (0 through 5) of the six options. Navigate through the six options by clicking the up and down arrows.

24) Click the ‘Close’ button located on the bottom right of the SediMeter Calibration Coefficients window. The coefficients are now incorporated into the data that will be viewed in the SediMeter Data window.

25) Select ‘Analyze Logged’ from the Data dropdown menu (or Ctrl+A).

26) Select the SediMeter network identifier number from the SediMeter NetAddr drop down box on the right side of the SediMeter Data window. This number is typically 1. This must be done to refresh the graphs to display the downloaded data.

27) Select RAW from the SediMeter variable drop down list.

28) Right click on the green cursor on the upper yellow box on the right side of the SediMeter Data Window. Click ‘Bring to Center’. This will bring the cursor into the center of the SediMeter Backscatter Intensity plot. The upper yellow box is used for the SediMeter Backscatter Intensity graph, while the lower yellow box is used for the Data Plot graph.

29) Move the mouse pointer over the cursor on the SediMeter Backscatter Intensity graph. Click on the cursor and while holding the button down, drag the mouse. This will allow for adjustment of the (x,y) position of the cursor. Note that when moving the SediMeter Backscatter Intensity graph cursor, the numbers in the upper yellow box change.

30) Line the cursor up with the time that will be used as the calibration time. The author randomly used data from the second measurement as the calibration time.

31) In the upper yellow box, edit the detector number from which you wish to obtain the RAW value by changing the number from 0 to 35. Detector 1 corresponds to 0 in the yellow box, detector 2 corresponds to 1 in the yellow box, and so forth. Please note that time cannot be edited. If attempting to edit the time, an error will occur and the program will close.

32) Record the RAW values from each detector in a spreadsheet. Thirty-six different numbers should be recorded. Table A.3 displays the RAW values obtained by the author when completing this portion of the calibration.

33) Ensure the correct RAW values have been obtained by repeating the Steps 2 – 32 two or three additional times and taking the average of the RAW values for each detector.

34) Coefficient K_{sm} can be calculated for each sensor using Equation A.2. The average RAW values determined in Step 33 and the turbidity of the solution used in Step 3 should be the values used for RAW and T_b, respectively. Insert the new K_{sm} values into the KABC table. This new KABC table should be used for analyzing all subsequent data.

A.1.3 Note on Coefficients B_{sm} & C_{sm}

The SediMeter manufacturer was contacted to obtain methodologies that can be used to validate the assumption made by the SediMeter Software Manual of $B_{sm} = 1$ and $C_{sm} = 0$. Lindorm recommended the completion of numerous tests to analyze the U_{off} values (which record the ambient light intensity) to determine if the B_{sm} coefficient could be set to 1. The U_{off} value was measured for four different SediMeter setups: in deionized water in darkness, in deionized water with light, in the open air in darkness, and in the open air with ambient light. The average U_{off} value when the SediMeter was placed in these situations was 0.001, 0.003, 0.002, and 0.037 V, respectively. This last

U_{off} value is an order-of-magnitude larger than the other values. This indicates that as ambient light enters the water, it is dissipated to the point that it is negligible. Therefore, the B_{sm} coefficient can be set to 1. Secondly, Lindorm recommended that $C_{sm} = 0$, but to flag any values with $U_{on} > 2.1$ V as minimum FBU values (e.g., the FBU values are potentially higher). U_{on} values were not larger than 2.1 V during the study, therefore, the assumption of $C_{sm} = 0$ is valid.

A.1.4 Conversion to Suspended Sediment Concentration

A relationship needs to be developed between turbidity and suspended sediment using sediment obtained from the study site in order to convert turbidity values to suspended sediment concentrations. To do this, five different solutions with known suspended sediment concentrations were prepared. The turbidity (in FBU) of the solutions was measured using a laboratory turbidimeter. The known concentrations, C_s, were plotted against the FBU values. A relationship in the form of Equation A.7 was determined:

$$C_s = a(FBU)^q \qquad \text{A.7}$$

where a and q are coefficients determined by plotting a power trend line on the data. Table A.4 and Figure A.4 display the results of the turbidity and suspended sediment relationship developed for the Tama soil type, which is the dominant soil type in this study.

A.2 SediMeter Installation

The installation procedure for the SediMeter is outlined in the following paragraphs. An anchor was installed in the bed by screwing it in a clockwise motion until only the tip of the anchor was visible. The protective acrylic tube was screwed onto the anchor tip so that it was positioned vertically. Deionized water was poured into the acrylic tube in an effort to mimic the calibration setup and minimize the entrance of polluted stream water into the tube. The SediMeter was then inserted into the acrylic tube with the sensors pointed downstream. The yellow screw was tightened to fix the protective tube on the SediMeter.

A small U-post was hammered into the stream bed directly upstream of the SediMeter. This post served to protect and further secure the SediMeter. The SediMeter was connected to the U-post using zip ties and fishing wire. Three T-posts also serving as protection for the SediMeter were hammered into the stream bed in a triangular pattern (Figure 4.6). The T-posts were attached to the SediMeter using fishing wire. These steps were completed in an effort to ensure the SediMeter would not be lost during high flow events.

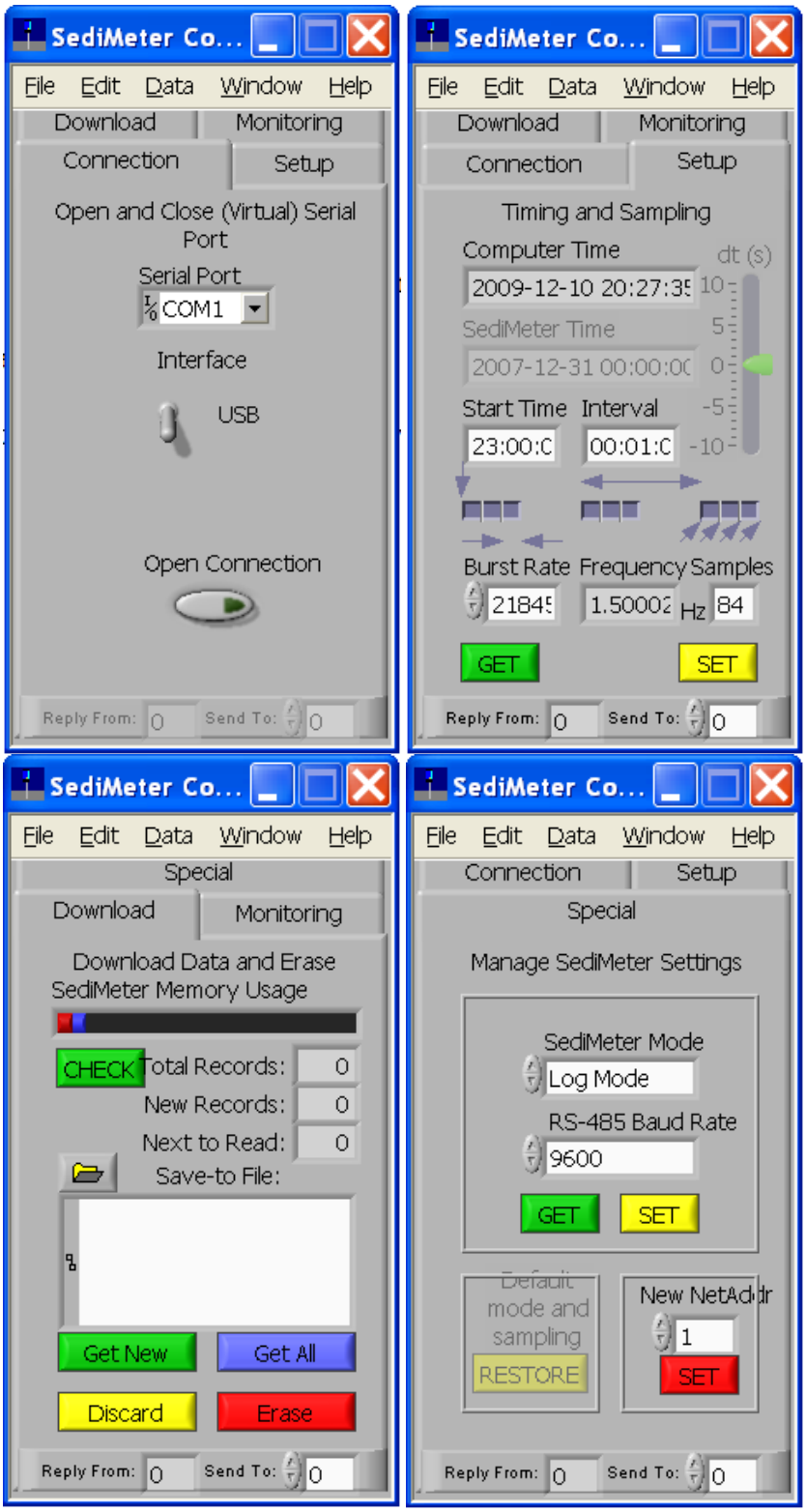

Figure A.1. Graphical user interface for SediMeter control

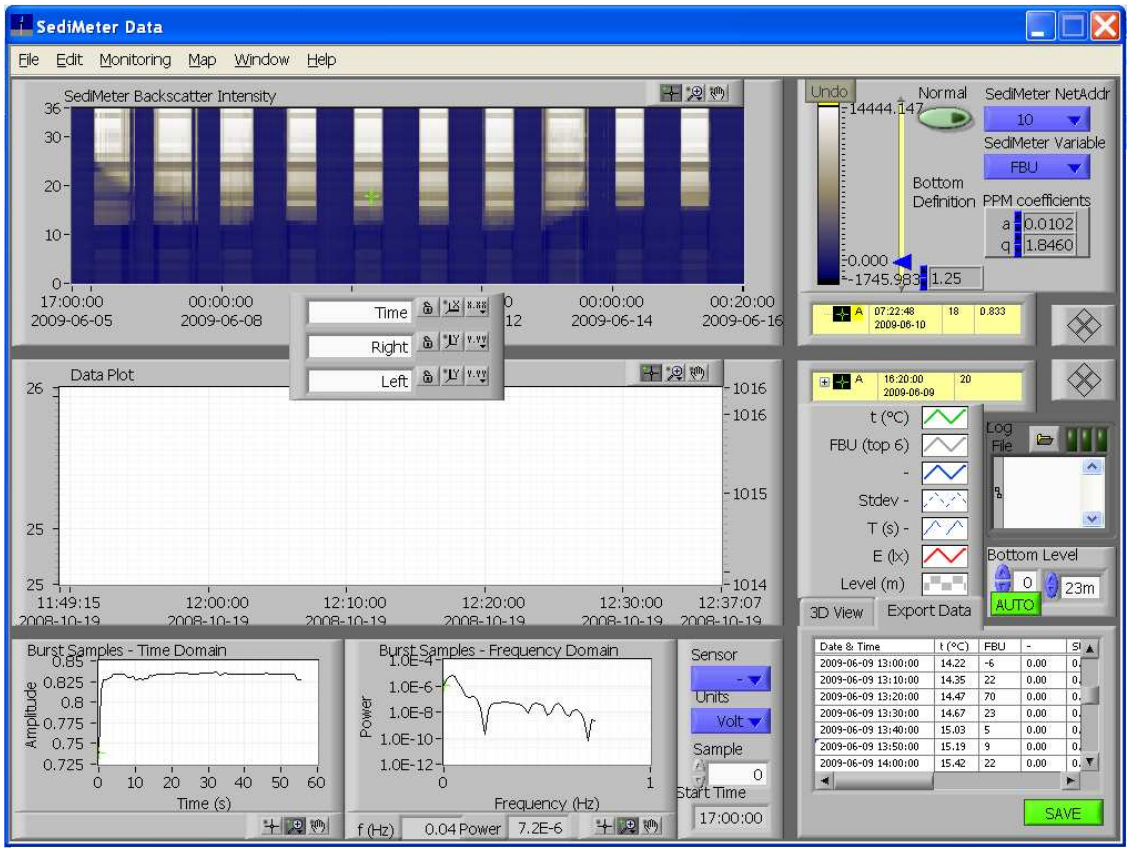

Figure A.2. Graphical user interface for data analysis

Table A.1: Coefficients A_{sm} and D_{sm} results

Sensor	Uon1	Uon2	Uon3	UonAvg	A	D
1	0.314	0.314	0.316	0.315	0.315	0.001
2	0.290	0.292	0.290	0.291	0.291	0.001
3	0.259	0.261	0.257	0.259	0.259	0.001
4	0.255	0.255	0.251	0.254	0.254	0.001
5	0.285	0.288	0.290	0.288	0.288	0.001
6	0.344	0.345	0.346	0.345	0.345	0.001
7	0.337	0.339	0.340	0.339	0.339	0.001
8	0.255	0.252	0.251	0.253	0.253	0.001
9	0.260	0.260	0.259	0.260	0.260	0.001
10	0.273	0.271	0.268	0.271	0.271	0.001
11	0.265	0.261	0.260	0.262	0.262	0.001
12	0.293	0.290	0.288	0.290	0.290	0.001
13	0.281	0.277	0.276	0.278	0.278	0.001
14	0.325	0.324	0.321	0.323	0.323	0.001
15	0.343	0.342	0.341	0.342	0.342	0.001
16	0.238	0.237	0.236	0.237	0.237	0.001
17	0.335	0.332	0.330	0.332	0.332	0.001
18	0.207	0.206	0.205	0.206	0.206	0.001
19	0.209	0.210	0.209	0.209	0.209	0.001
20	0.283	0.284	0.283	0.283	0.283	0.001
21	0.294	0.295	0.289	0.293	0.293	0.001
22	0.304	0.305	0.300	0.303	0.303	0.001
23	0.323	0.325	0.324	0.324	0.324	0.001
24	0.247	0.249	0.249	0.248	0.248	0.001
25	0.183	0.182	0.182	0.182	0.182	0.001
26	0.305	0.304	0.298	0.302	0.302	0.001
27	0.253	0.255	0.253	0.254	0.254	0.001
28	0.305	0.309	0.305	0.306	0.306	0.001
29	0.335	0.337	0.329	0.334	0.334	0.001
30	0.317	0.318	0.312	0.316	0.316	0.001
31	0.327	0.331	0.329	0.329	0.329	0.001
32	0.340	0.342	0.337	0.340	0.340	0.001
33	0.293	0.294	0.294	0.294	0.294	0.001
34	0.336	0.330	0.335	0.334	0.334	0.001
35	0.218	0.217	0.220	0.218	0.218	0.001
36	0.292	0.295	0.292	0.293	0.293	0.001

Table A.2: Coefficient KABC results

K	A	B	C
6820	0.315	1	0
6820	0.291	1	0
6820	0.259	1	0
6820	0.254	1	0
6820	0.288	1	0
6820	0.345	1	0
6820	0.339	1	0
6820	0.253	1	0
6820	0.26	1	0
6820	0.271	1	0
6820	0.262	1	0
6820	0.29	1	0
6820	0.278	1	0
6820	0.323	1	0
6820	0.342	1	0
6820	0.237	1	0
6820	0.332	1	0
6820	0.206	1	0
6820	0.209	1	0
6820	0.283	1	0
6820	0.293	1	0
6820	0.303	1	0
6820	0.324	1	0
6820	0.248	1	0
6820	0.182	1	0
6820	0.302	1	0
6820	0.254	1	0
6820	0.306	1	0
6820	0.334	1	0
6820	0.316	1	0
6820	0.329	1	0
6820	0.34	1	0
6820	0.294	1	0
6820	0.334	1	0
6820	0.218	1	0
6820	0.293	1	0

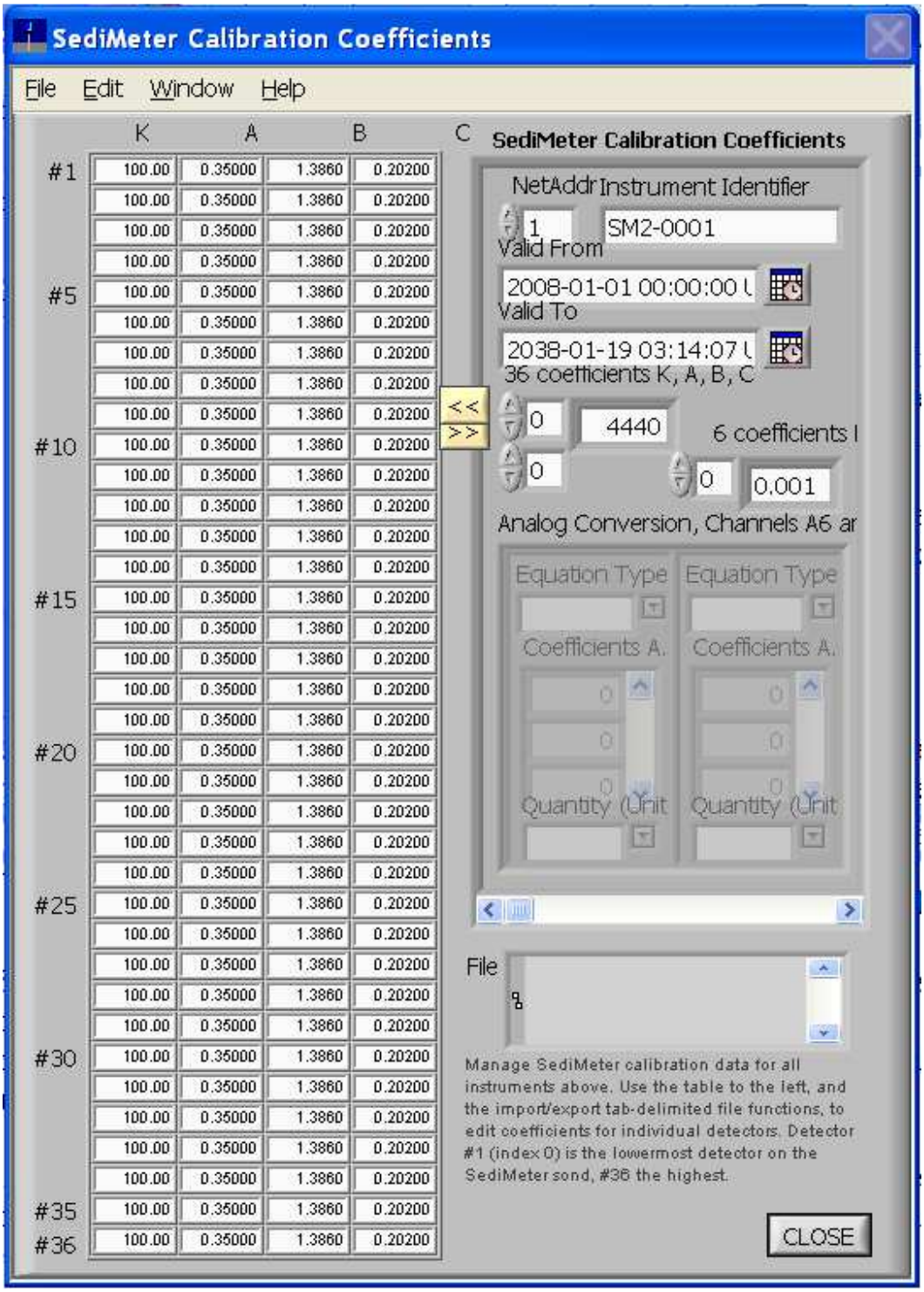

Figure A.3. Calibration coefficients window

Table A.3: Calibration coefficient K_{sm} results

RAW1 (V)	RAW2 (V)	RAW3 (V)	RAWAvg (V)	Conc. (FTU)	K_{sm}
0.361	0.354	0.366	0.360	1600.0	4440
0.392	0.370	0.382	0.381	1600.0	4196
0.383	0.355	0.408	0.382	1600.0	4188
0.420	0.392	0.402	0.405	1600.0	3954
0.384	0.393	0.382	0.386	1600.0	4142
0.355	0.404	0.362	0.374	1600.0	4282
0.369	0.399	0.370	0.379	1600.0	4218
0.238	0.241	0.239	0.239	1600.0	6685
0.254	0.271	0.262	0.262	1600.0	6099
0.288	0.292	0.288	0.289	1600.0	5530
0.254	0.270	0.264	0.263	1600.0	6091
0.235	0.259	0.255	0.250	1600.0	6409
0.254	0.279	0.262	0.265	1600.0	6038
0.214	0.252	0.267	0.244	1600.0	6548
0.223	0.242	0.261	0.242	1600.0	6612
0.210	0.233	0.225	0.223	1600.0	7186
0.246	0.269	0.269	0.261	1600.0	6122
0.142	0.159	0.164	0.155	1600.0	10323
0.176	0.180	0.196	0.184	1600.0	8696
0.210	0.232	0.240	0.227	1600.0	7038
0.270	0.278	0.278	0.275	1600.0	5811
0.285	0.284	0.284	0.284	1600.0	5627
0.202	0.204	0.260	0.222	1600.0	7207
0.072	0.089	0.090	0.084	1600.0	19124
0.163	0.170	0.152	0.162	1600.0	9897
0.247	0.258	0.274	0.260	1600.0	6162
0.170	0.183	0.196	0.183	1600.0	8743
0.264	0.274	0.310	0.283	1600.0	5660
0.236	0.261	0.263	0.253	1600.0	6316
0.218	0.245	0.205	0.223	1600.0	7186
0.228	0.252	0.274	0.251	1600.0	6366
0.226	0.256	0.248	0.243	1600.0	6575
0.272	0.243	0.283	0.266	1600.0	6015
0.294	0.293	0.312	0.300	1600.0	5339
0.202	0.207	0.215	0.208	1600.0	7692
0.271	0.292	0.294	0.286	1600.0	5601

Table A.4: ppm data

Concentration (g/L)	Concentration (ppm)	Turbidity (NTU)
0	0	0.7
2.5	2500	510
5	5000	1194
7.5	7500	2247
10	10000	3328
12.5	12500	4193

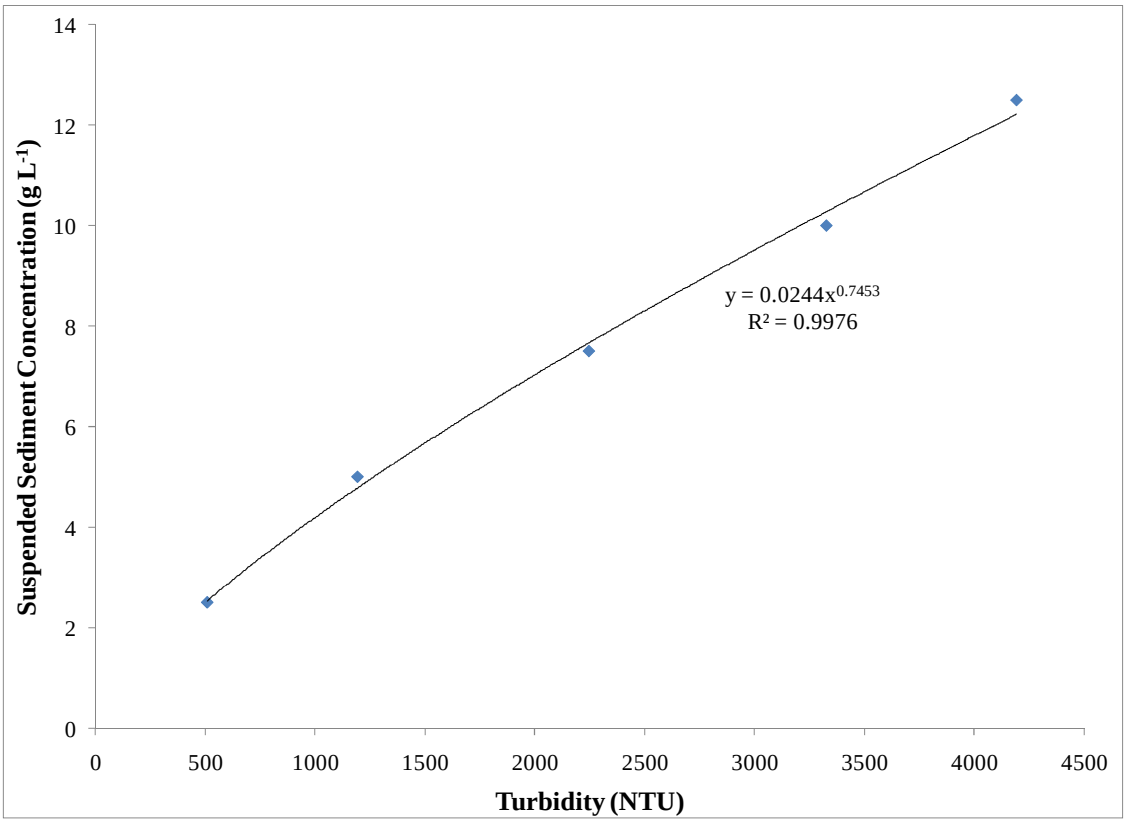

Figure A.4: Association between turbidity and suspended sediment concentration

APPENDIX B RADIONUCLIDE ANALYSIS

The radionuclide activities of source, suspended sediment, and precipitation samples were analyzed using gamma analysis. Gamma analysis is the capture of gamma particles emitted from a sample. Gamma particles are emitted from samples during the decay of radionuclides. The number of gamma particles captured is dependent on the concentration of radionuclides in the sample. Each sample must be collected and prepared using uniform methodologies. Additionally, the efficiency of the gamma analysis technique must be determined to allow for standardization of reported values. The collection and preparation procedures and efficiency determinations are outlined in the following sections.

B.1 Systematic Sample Collection and Preparation Procedures

Source samples from the uplands, channel banks, and channel bed were gathered to determine the pre-existing radionuclide activities of these sediments. Precipitation samples were collected to measure the radionuclide inputs into the SASW. These samples were collected using a systematic method to ensure sample uniformity. The source and suspended sediment samples were then prepared for analysis by isolating the clay-sized fraction. This was necessary due to the proclivity of the radionuclides to attach to this fraction. The precipitation samples were also prepared for analysis by forcing radionuclide adsorption to a flocculent.

B.1.1 High-Resolution Upland Sample Collection

Upland samples were collected using a method that allowed for the differentiation of radionuclide activities at 5-mm depth intervals. Sampling the upland source in 5-mm intervals was necessary because radionuclide activities diminish as depths increase.

Using this methodology, a high-resolution radionuclide profile could be developed. The following steps outline the high-resolution upland sample collection procedure.

1) Record the geographic coordinates of the sampling location in the field book.

2) Take a picture of the sampling location and record the picture number in the field book. Be sure to capture any residue cover present.

3) Drive the three-sided sampling frame into the ground with the open end of the sampler facing downslope.

4) Dig a pit downslope of the sampler being sure not to disturb any portion of the sample contained within the sampler. The pit should be deeper than the frame so that a shovel can be leveraged beneath the frame to assist in the removal of the soil block from the ground.

5) Remove the sample in the ground by leveraging it out of the ground with a shovel, being sure to not to disturb the sample during the process.

6) Cut the excess soil outside of the sampler volume away with a knife.

7) Insert a blade into the first groove (located at the portion of the sampler containing the topmost layer of soil) in the sampler. This will section the sample into a sample containing the soil within the 0-5 mm depth.

8) Put the soil cut by the blade into a baggie.

9) Label the baggie appropriately.

10) Continue sectioning the sample in 5 mm intervals until the top 30 mm have been sampled and bagged.

B.1.2 Bank Sample Collection

Bank samples were collected using a method that collected samples deep into the soil profile. This was necessary because bank collapse contributes large amounts of sediment, oftentimes from deep in the soil profile. The following steps outline the bank sample collection procedure.

1) Record the geographic coordinates of the sampling location in the field book.

2) Insert the 33-cm long plastic tube into the coring tubing.

3) Attach the coring device to the slide hammer.

4) Pound the hammer on the sampling tube until it is driven into the ground to the point that the entire plastic sleeve is below the ground surface.

5) Pull the sampling tube carefully out of the ground.

6) Remove the plastic sleeve from the sampling tube using pliers to grab and pull the plastic sleeve.

7) Mark a baggie with the sample coordinates and depth.

8) Remove the soil from the plastic sleeve by pushing it out with an erosion pin.

9) Place the soil into the plastic baggie.

10) Continue with the bank sample collection in the same location until three repetitions of the bank coring have been completed (totaling 99 cm in depth). Each different sampling depth (0-33, 33-66, and 66-99 cm) should be placed into separate baggies.

B.1.3 Clay Separation

Radionuclides preferentially attach to the clay-sized fraction of sediments. Therefore, the source and suspended sediment samples were prepared for analysis by isolating the clay-sized fraction. The following steps outline the clay separation procedure.

1) Clean all supplies to be used with HCl before commencing clay separation.

2) Remove the sample from the baggie and place it into a pre-tared aluminum tin.

3) Record the tin number, tin tare weight, and sample name on a data sheet.

4) Allow the sample to air dry for at least 24 hours.

5) Place the aluminum tin containing the sample into an oven that is set at approximately 60°C. As many aluminum tins as possible may be placed into the oven.

6) Allow the sample to oven dry for at least 48 hours to remove all water.

7) Weigh the oven-dried sample (after allowing the sample and tin to cool to room temperature) and record the weight on data sheet.

8) Pour the sample from the tin back into the baggie from which it was removed.

9) Crush the sample lightly using a rolling pin. Roll the rolling pin across the baggie containing the sample as many times as necessary to break up the soil clumps. If any holes are punched into the baggie during this process, seal the holes using duct tape or masking tape.

10) Sieve the sample using a 2-mm sieve to remove any material that is larger than a sand particle.

11) Tare three 125-mL Nalgene bottles after appropriately labeling each bottle with the sample name and subsample number (e.g., A6-1, A6-2, and A6-3).

12) Add approximately 30 g of the sample to each Nalgene bottle. Record the exact weight of soil added to each bottle on a data sheet.

13) Add $Na(PO_6)_3$ (created by adding 40 g of sodium metaphosphate to 1000 mL of water) to the subsample in a 1 mL of $Na(PO_6)_3$ to 1 g of subsample ratio to disaggregate the particles.

14) Add 20-mL of deionized (DI) water to each subsample (or enough DI water to ensure that the Nalgene bottle is over half full). Record the amount of water added to the subsample.

15) Place each Nalgene bottle onto the shaker apparatus. Shake overnight at 225 rpm.

16) Write the sample name on a piece of masking tape, then place the tape onto a clean, dry 7.5 L bucket that is specially marked for the clay/silt separation process. This bucket can be identified by looking at the inside of the bucket for a dashed line that is 15.24 cm from the bottom of the bucket.

17) Complete the wet sieve process by flushing each subsample through a 63-µm sieve with DI water into the pre-labeled bucket. Each of the three subsamples may be flushed into the same pre-labeled bucket so that the subsamples are recombined into one sample.

18) Place the portion of the sample that has been retained on the 63-µm sieve into a 125-mL Nalgene bottle.

19) Move the bucket containing the silt/clay suspension onto a table.

20) Add DI water to the silt/clay suspension bucket until the water level reaches the markings on the inside of the bucket.

21) Mix the silt/clay suspension for two minutes using a drill that has been fitted with a mixing attachment.

22) Allow the suspension to settle for 7 hours, 40 minutes, with the time beginning at the end of the mixing.

23) Place a 20 L bucket on the floor below the silt/clay suspension bucket and label the bucket with the sample name.

24) Begin the siphoning process by briefly sucking on the tubing until the suspension begins to flow through the tubing and into the bucket.

25) Allow the clayey solution to flow through the tubing and into the 20 L bucket until it stops flowing because of the water level reaching the bottom of the tubing apparatus.

26) Repeat Steps 20 - 25 two more times so that three total siphoning processes have been completed.

27) Discard the suspension that remains in the 7.5 L bucket.

28) Add 140 mL of an aluminum sulfate solution (created by adding 30.22 g of aluminum sulfate to 1000 mL of deionized water) to the suspension in the 20 L bucket.

29) Siphon water from the 20 L bucket after allowing the clayey suspension to settle overnight. The amount of water siphoned depends on the height of the settled clayey material. Do not siphon clay particles off the bottom of the bucket when siphoning the water.

30) Discard the siphoned water.

31) Label the glass jars with the appropriate sample name.

32) Pour the clayey suspension from the 20 L bucket into the pre-labeled glass jars. Use as many glass jars as necessary to accommodate the entire suspension. Ensure that all of the clayey material has been removed from the bucket by washing the bucket down with a DI water squirt bottle.

33) Allow the suspension in the glass jars to settle overnight.

34) Siphon water out of the glass jars while ensuring that clay particles are not sucked out of the jar.

35) Place the glass jars into the oven and heat at approximately 60°C.

36) Remove the glass jars from the oven whenever the water has been evaporated from the jars. This will typically take anywhere from 2 to 4 days.

37) Tare and label one Petri dish (48 mm diameter, 8 mm height) per sample in the oven. Record the tare weight and the sample number on a data sheet.

38) Scrape the clay particles from the glass jars. For each of the glass jars that contain the same sample, combine the contents of the jars into one jar.

39) Fill the pre-labeled Petri dish with the appropriate clay-sized fraction of the sample. Only fill one Petri dish. If excess material remains, place the excess material into a plastic cup that has been appropriately labeled and move the cup to storage.

40) Weigh the soil and Petri dish and record the combined weight on the data sheet.

B.1.4 Precipitation Collection

Precipitation samples were collected to measure the radionuclide inputs into the SASW. The following steps outline the precipitation collection procedure.

1) Clean each 20 L bucket to be used with HCl before installation.

2) Record the geographic coordinates of the sampling location in the field book.

3) Place a 20 L bucket upright at the sampling location.

4) Secure the 20 L bucket by taping the bucket to a t-post.

5) Cap the bucket after the storm has finished.

B.1.5 Precipitation Flocculent Preparation

The precipitation samples were prepared for analysis by forcing radionuclide adsorption to a flocculent. The following steps outline the precipitation flocculation procedure.

1) Lower the pH of the sample to ~2 by adding 50 mL of 10% HCl (to prevent radionuclide sorption to the container or any particulate matter).

2) Pour the sample through a sieve to remove any particulates.

3) Add 10 mL of a 10% $FeCl_3$ solution to the sample.

4) Raise the pH of the sample to ~8.2 to precipitate $Fe(OH)_3$, which will have radionuclides sorbed to it.

5) Allow the resulting flocculent to settle overnight.

6) Siphon the water, ensuring that no flocculent is removed during the siphoning process.

7) Once the volume of the flocculent has been reduced to a sufficiently small volume, collect the flocculent in a 120 mL polyethylene specimen cup.

B.2 Gamma Spectroscopy

Samples were analyzed using the gamma spectroscopy analysis technique. The efficiency of the gamma detector and the sample geometry were determined by creating and analyzing samples with known radionuclide activities; these were termed standards. The activities were interpreted using the gamma spectroscopy software GammaVision.

B.2.1 Gamma Spectroscopy Setup

An Ortec High-Purity Germanium (HPGe) Coaxial Detector System was used to complete the gamma analysis of samples. Figure B.1 displays the detector setup. The primary points of interest are the detector (model GEM-FX7025-S, Figure B.2), the cooling rod (model LB-GEM-SV-C-S), and the dewar (model DWR-30, Figure B.3). The portion of the system that receives the emitted photon energy from the soil sample is the detector, which is housed inside of a vertical carbon fiber cryostat. A metal cooling rod extending from the detector is immersed in a liquid nitrogen bath contained within the dewar. The dewar has a capacity of 30 L and was filled every week with liquid nitrogen to ensure temperature regulation. The reason behind the immersion of the rod is to regulate the temperature of the detector. If not immersed in liquid nitrogen, the detector would overheat due to the high voltages (and subsequent heat generation) that pass through the detector. External interference was muted by a lead shield that encompassed the detector assembly (Figure B.3).

B.2.2 Efficiency Determinations

The efficiency of the detector, sample geometry, and sample mass was determined using two Standard Reference Materials (SRMs), two geometries, and five masses. The first SRM (Nuclitec RBZB44) contained only ^{210}Pb. The second SRM (Nuclitec QCY44) contained several radionuclides with energies spanning a range of nearly 1800 keV. The radionuclides contained in the SRMs are listed in Table B.1. The first sample geometry was a Petri dish having a diameter of 48 mm and a height of 8 mm. The second sample geometry was a polyethylene specimen cup having a volume of 120 mL. Five different inactive soil masses were used in the Petri dishes: 1, 3, 5, 10, and 15 g. The standards were then added to the soil by placing 0.1 mL drops into the standard solution in concentric circles. The soil masses and standard solution volumes are listed in Table B.2. The soil was allowed to air dry, and then the Petri dish was sealed with electrical tape. All standards were analyzed for 7200 seconds.

Using the energy range of the QCY44, a relationship was developed between energy and detector efficiency for each radionuclide. The detector efficiency for other radionuclides not in the second SRM (e.g., ^{7}Be) was interpolated from the data points. The efficiencies of the radionuclides used in this study are displayed in Table B.3. For further information on this topic, please see the report by Wilson and Kuhnle (2006).

The efficiency of various masses was also tested during calibration. Figure B.4, Figure B.5, and Figure B.6 show the efficiency of the detector for capturing gamma emissions of ^{210}Pb, ^{214}Bi, and ^{7}Be, respectively, at various masses. The efficiency of the detector is approximately the same for all masses. Thus, the sample mass efficiency was determined to be constant.

B.2.3 Systematic Standard Solution Preparation

The efficiency of the gamma analysis technique was determined by testing the activity recorded by the setup and comparing the activity to the known activity of the analyzed standard. A standard solution with a known activity was created as the first step towards determining the efficiency of the gamma analysis setup. The solution was created using the following calculations and steps.

Calculations were performed to determine the amount of N441 inactive dilutent to add to the QCY44 SRM to create the standard solution. The mass of the SRM was listed as 5.3479 g. The density of the SRM was listed as 1.068 g mL^{-1}. Thus, dividing the mass by the density gave the volume of the SRM, 5.007397 mL. The carriers in the standard solution must be in a 25 μg mL^{-1} ratio. Typically, 100 mL of stock solution is required. Thus, 2500 μg of carriers (25*100) are required in the 100 mL standard solution. The SRM has carriers in the 25 μg mL^{-1} ratio. Thus, the SRM has 125.1849 μg of carriers. Therefore, 2500 – 125.1849, or 2374.8151 μg of carriers are needed from the dilutent. The N441 inactive dilutent has carriers in a 225 μg mL^{-1} ratio. Thus, 2374.8151/225, or 10.55473 mL of dilutent are needed.

Calculations were also performed to determine the amount of NQB2392 inactive dilutent to add to the RBZB44 SRM to create the standard solution. The volume of the SRM was listed as 0.005 L. The carriers in this standard solution must be in a 20 mg L^{-1} ratio. Typically, 0.1 L of stock solution is required. Thus, 2 mg of carriers (20*0.1) are required in the 100 mL standard solution. The SRM has carriers in the 20 mg L^{-1} ratio. Thus, the SRM has 0.1 mg of carriers. Therefore, 2.0 – 0.1, or 1.9 mg of carriers are needed from the dilutent. The NQB2392 inactive dilutent has carriers in a 4 mg mL^{-1} ratio. Thus, 1.9/4, or 0.475 mL of dilutent are needed.

1) Clean all applicable supplies with the acid that will touch these supplies (i.e., 1.2 M HCl or 4 M HNO_3).

2) Set up the ring stand and clamp to securely hold the volumetric flask.

3) Place the funnel in the top of the flask.

4) Carefully saw open the vial of the SRM. The saw should have come with the SRM. Be sure to not spill ANY of the solution.

5) Pour the vial into the funnel. If surface tension prevents flow from the vial, tap the vial gently until liquid begins pouring out.

6) Fill the vial with acid 5 times, each time emptying the acid from the vial into the funnel. The acid needs to be the same as that listed in the packaging used to mix with the original SRM (e.g., 1.2 M HCl or 4 M HNO_3).

7) Add the appropriate amount of inactive dilutent (calculated in the paragraphs above).

8) Fill the vial with acid 5 more times, each time emptying the acid from the vial into the funnel. Again, the acid needs to be the same as that listed in the packaging used to mix with the SRM (e.g., 1.2 M HCl or 4 M HNO_3).

9) Fill the volumetric flask with the appropriate acid to the 100 mL line. Do not over or under fill the flask.

10) Pour the solution from the volumetric to a Qorpak bottle. Do not rinse the volumetric flask into the Qorpak bottle. It is ok to have a small amount of liquid left in the volumetric flask.

11) Seal the Qorpak bottle.

B.2.4 Systematic Standard Geometry Preparation

The standard solution created in the previous section is added to an inactive soil medium to create the final standard that will be used to determine the gamma analysis efficiency. The solution is added according to the following steps.

1) Add the amount of the inactive medium (‘old’ soil) you are using to the Petri dish. For the 10 g and 15 g standard, only add approximately half (i.e., 5 g or 7.5 g) of the total soil amount initially.

2) Program the precise dropper to remove 0.1 mL by setting the dropper to read 100|0. This value is 100.0 µL, which is equal to 0.1 mL.

3) Put the tip onto the dropper by pushing the dropper into the tip.

4) Prime the precise dropper to withdraw 0.1 mL by sucking the QCY44 standard solution into the dropper then pushing the solution back into the Qorpak bottle three times.

5) Using the precise dropper, add the QCY44 standard solution in 0.1 mL increments to the soil in concentric circles until the total standard solution volume required has been added. For the 10 g and 15 g standard, only add half (i.e., 1 mL) of the total solution amount initially.

6) Discard the previously used tip and put a new one on the dropper.

7) Add the RBZ44 standard in 0.1 mL increments using a precise dropper until the appropriate volume has been added. For the 10 g and 15 g standard, only add half (i.e., 1 mL) of the total solution amount initially.

8) Add the rest of the soil to the 10 g and 15 g sample.

9) Add the rest of the standard solutions to the 10 g and 15 g sample following the same procedures until the final 1 mL has been added to each sample.

10) The soil matrix should be completely saturated after the entire volume has been added.

11) Allow the soil to air dry.

12) Seal the dish with electrical tape.

13) Analyze the standard using the gamma setup.

B.2.5 Use of GammaVision Software

The software package GammaVision is used to begin gamma particle emission counting and to analyze the spectrum resulting from the counting. The following steps outline the GammaVision procedure used to begin gamma particle emission counting. Additionally, the properties of GammaVision used in the analysis of the spectrum are listed.

1) Place the sample to be analyzed on the detector.

2) Insert the USB connection from the DSPEC jr into the computer.

3) Open GammaVision.

4) Choose the detector to be used by selecting the Display dropdown menu then clicking Detector.

5) Double click on the detector to be used.

6) Enter the analysis time by selecting the Acquire dropdown menu then clicking MCB Properties.

7) Select the Presets tab in the new dialogue box.

8) Enter the desired live time in seconds to be used.

9) Click Close.

10) Begin the analysis process by first pressing Alt+1.

11) Enter in the sample description and continue.

12) Enter in the sample weight and press OK. Sample analysis has begun.

13) If stopping the analysis is necessary, press Alt+2.

14) Once the sample has been counted for the preset live time, save the sample by selecting the File dropdown menu then Save.

15) Save the spectrum to the desired location with the desired sample name.

16) Once the spectrum has been saved, clear the software and DSPEC jr by pressing Alt+3. A new sample can now be analyzed using the same process.

B.2.6 GammaVision Properties

The MCB properties of the GammaVision program used to determine the gamma emission rates for each sample were set to the following:

Amplifier Tab
Gain: 1.76
Fine: 0.8816
Coarse: X2
Baseline Restore: Auto
Preamplifier Type: Resistor Feedback
Pole Zero: 2778
Input Polarity: +

Amplifier 2 Tab
Rise Time: 12.00
Flattop Width: 1.00
Flattop Tilt: -0.05469

ADC Tab
Gate: Off
ZDT Mode: Off
Conversion Gain: 8192
Lower Level Disc: 25
Upper Level Disc: 8191

Stabilizer Tab
Neither gain stabilization nor zero stabilization was enabled.

High Voltage Tab
Target: 2500 V

Presets Tab
Live Time: 82800
Uncertainty (Start Chan): 0
Uncertainty (Width): 1

B.2.7 Activity Determination

After the sample was counted, the collected spectrum was analyzed. The location of the range of influence of the $^{210}Pb_{xs}$ peak was determined to be consistently between marker 223 and 241 when using the University of Iowa setup. The location of the range of influence of the ^{7}Be peak was determined to be consistently between marker 2372 and 2387. The location of the ^{214}Bi peak was determined to be located at approximately marker 3038. The range of influence was variable, as was the peak. Visual interpretation of the ^{214}Bi peak was conducted to ensure that the most correct range of influence was used in obtaining the final ^{214}Bi activity.

The activities of the peaks were determined using the software presets. The software provided the net area of each peak range of influence, along with the associated

standard deviation. The net area divided by the count time was used as the relative activity of the sample.

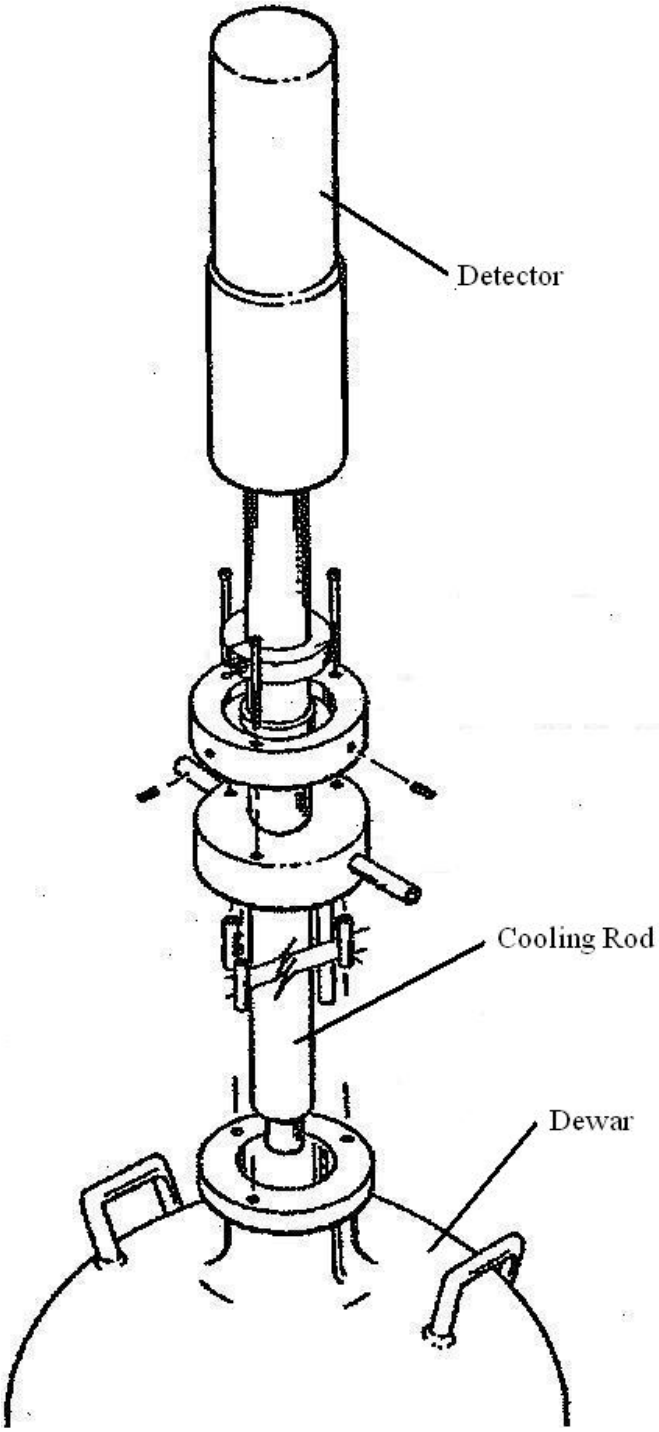

Figure B.1. Detector setup (Ortec 2008)

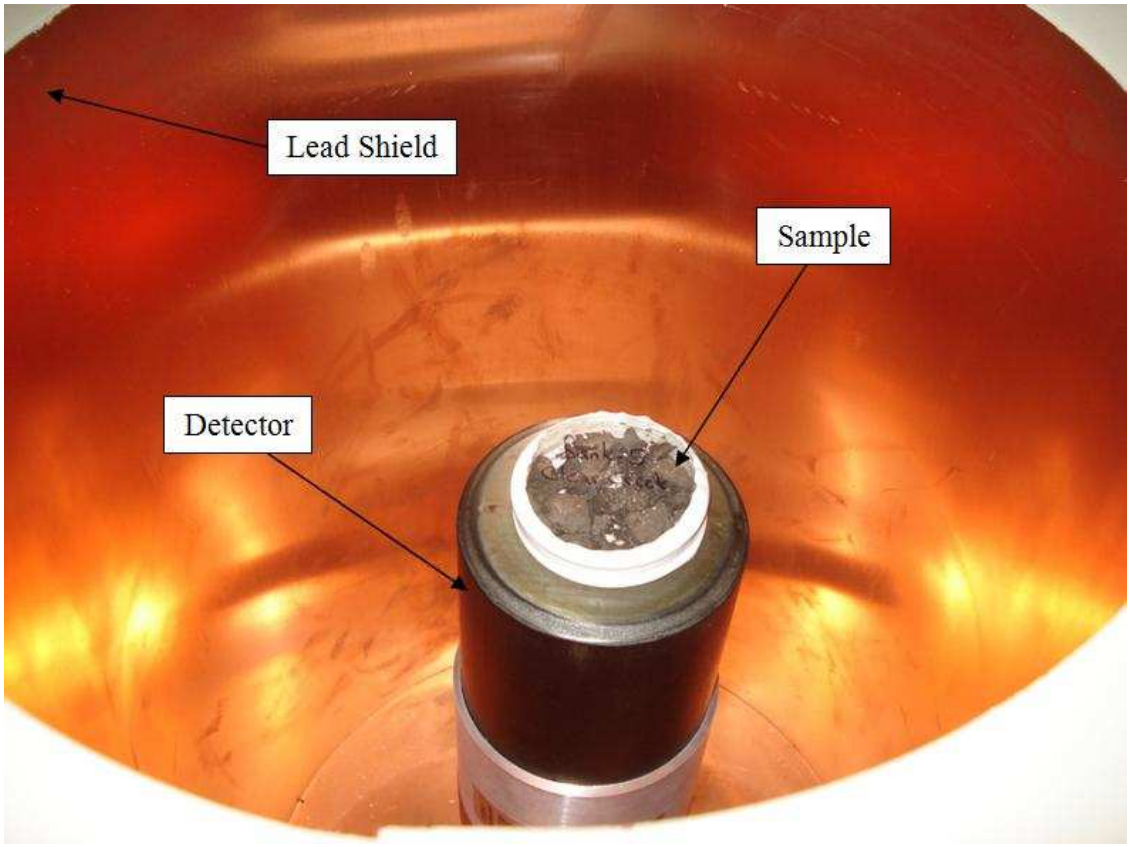

Figure B.2. Detector

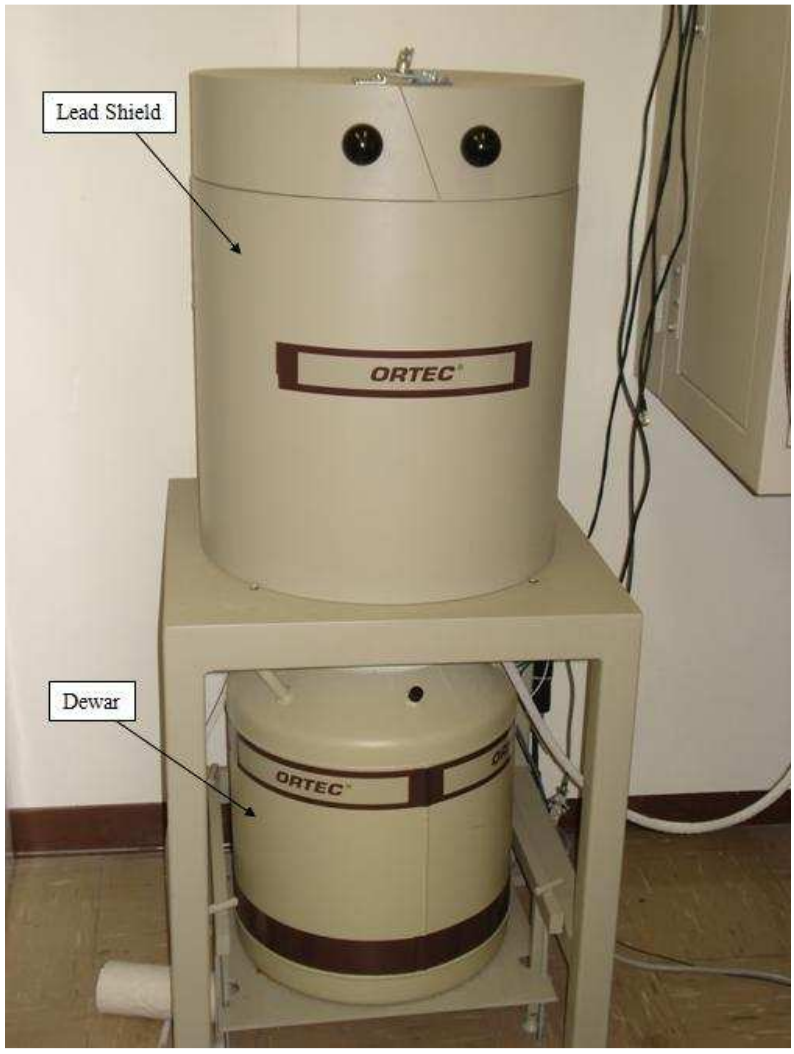

Figure B.3. Gamma spectroscopy setup

Table B.1. SRM radionuclide contents

Parent Radionuclide	Gamma-ray energy (keV)	Branching Ratio (%)
Lead-210	46.52	4.00
Cadmium-109	88.03	3.61
Cobalt-57	122.1	85.60
Cerium-139	165.9	79.95
Mercury-203	279.2	81.50
Tin-113	391.7	64.16
Strontium-85	514.0	99.28
Caesium-137	661.6	85.21
Yttrium-88	898.0	95.00
Cobalt-60	1173	99.86
Cobalt-60	1333	99.98
Yttrium-88	1836	99.35

Table B.2. Petri dish standards

Standard	Matrix Weight (g)	Volume QCY44 (mL)	Volume RBZB44 (mL)
1g	0.992	0.25	0.25
3g	2.989	0.50	0.50
5g	4.983	1.00	1.00
10g	9.984	2.00	2.00
15g	14.979	2.00	2.00

Table B.3. Calculated efficiencies

Parent Radionuclide	Gamma-ray energy (keV)	Petri Dish Efficiency (%)	Specimen Cup Efficiency (%)
Lead-210	46.52	28.6	22.6
Beryllium-7	477.6	5.7	1.9
Bismuth-210	609.3	4.4	1.4

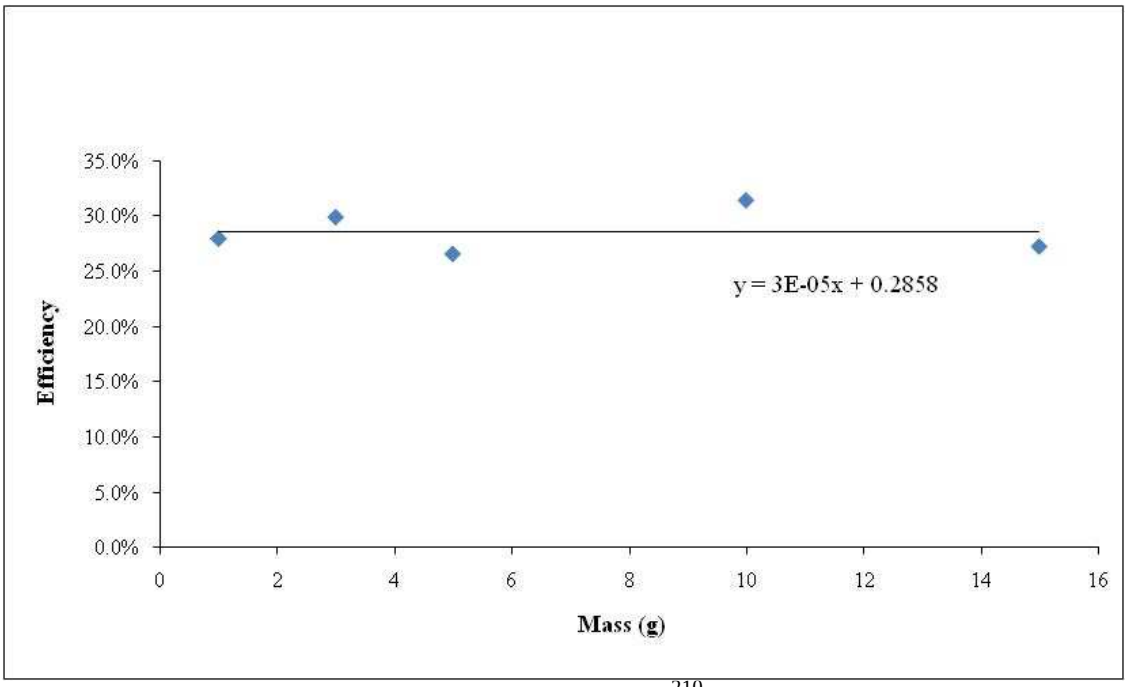

Figure B.4. Mass efficiency for the ^{210}Pb radionuclide

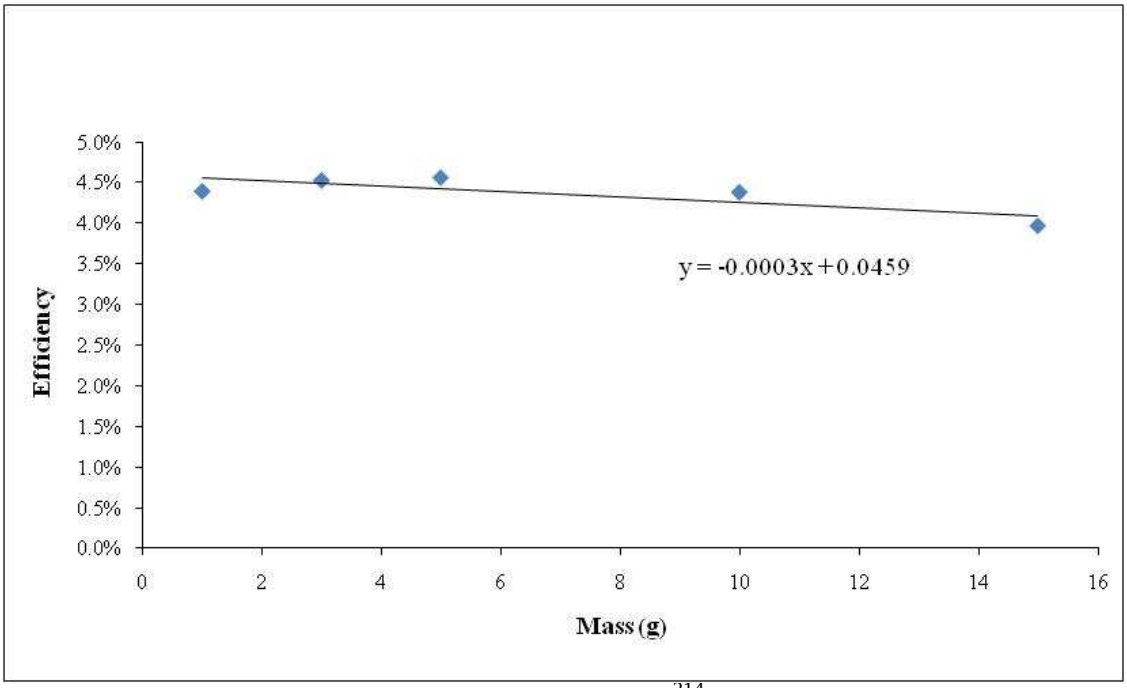

Figure B.5. Mass efficiency for the ^{214}Bi radionuclide

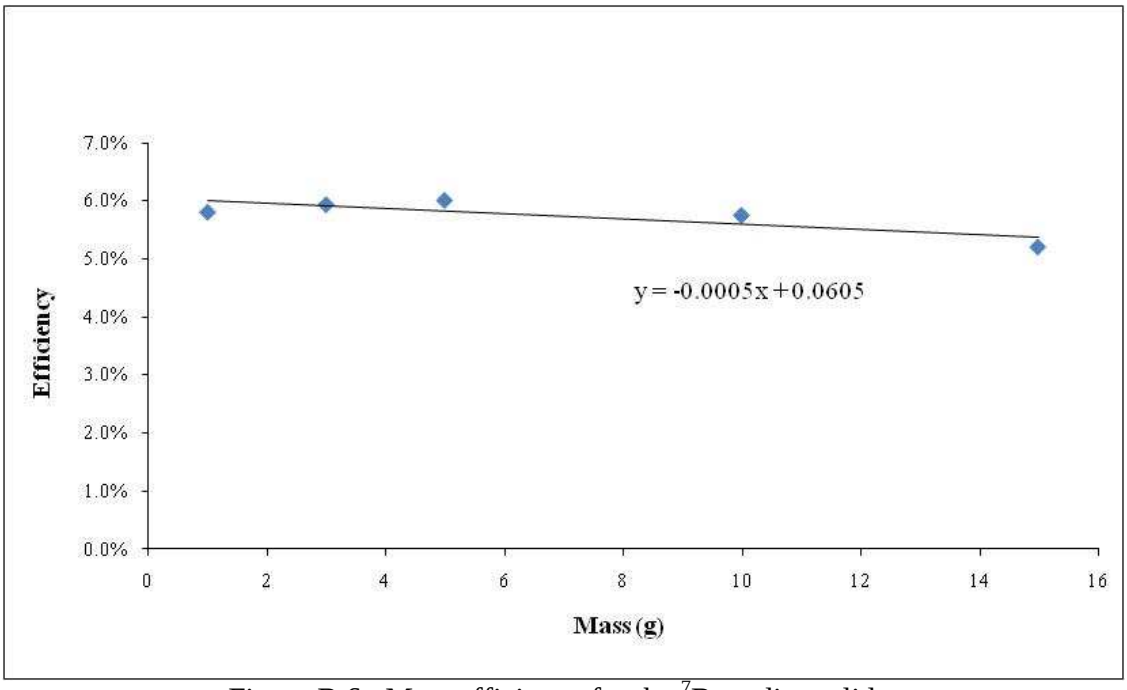

Figure B.6. Mass efficiency for the ^{7}Be radionuclide

REFERENCES

Abaci, O., and Papanicolaou, A. N. T. (2009). "Long-term effects of management practices on water-driven soil erosion in an intense agricultural sub-watershed: monitoring and modelling." *Hydrological Processes*, 23(19), 2818-2837.

Ahanger, M. A., Asawa, G. L., and Lone, M. A. (2008). "Experimental study of sediment transport hysteresis." *Journal of Hydraulic Research*, 46(5), 628-635.

Aksoy, H., and Kavvas, M. L. (2005). "A review of hillslope and watershed scale erosion and sediment transport models." *Catena*, 64(2-3), 247-271.

Al-Kaisi, M. M., and Yin, X. H. (2003). "Effects of nitrogen rate, irrigation rate, and plant population on corn yield and water use efficiency." *Agronomy Journal*, 95(6), 1475-1482.

Alexandrov, Y., Laronne, J. B., and Reid, I. (2003). "Suspended sediment concentration and its variation with water discharge in a dryland ephemeral channel, northern Negev, Israel." *Journal of Arid Environments*, 53(1), 73-84.

Alexandrov, Y., Laronne, J. B., and Reid, I. (2007). "Intra-event and inter-seasonal behaviour of suspended sediment in flash floods of the semi-arid northern Negev, Israel." *Geomorphology*, 85(1-2), 85-97.

Allmendinger, N. E., Pizzuto, J. E., Moglen, G. E., and Lewicki, M. (2007). "A sediment budget for an urbanizing watershed, 1951-1996, Montgomery County, Maryland, U. S. A." *Journal of the American Water Resources Association*, 43(6), 1483-1498.

Ametek. (2008). "DSPEC jr 2.0." Oak Ridge, TN.

Ascough, J. C., Baffaut, C., Nearing, M. A., and Liu, B. Y. (1997). "The WEPP watershed model .1. Hydrology and erosion." *Transactions of the Asae*, 40(4), 921-933.

Baca, P. (2008). "Hysteresis effect in suspended sediment concentration in the Rybarik basin, Slovakia." *Hydrological Sciences Journal-Journal Des Sciences Hydrologiques*, 53(1), 224-235.

Blake, W. H., Walling, D. E., and He, Q. (1999). "Fallout beryllium-7 as a tracer in soil erosion investigations." *Applied Radiation and Isotopes*, 51(5), 599-605.

Bonniwell, E. C., Matisoff, G., and Whiting, P. J. (1999). "Determining the times and distances of particle transit in a mountain stream using fallout radionuclides." *Geomorphology*, 27(1-2), 75-92.

Bracmort, K. S., Engel, B. A., and Frankenberger, J. R. (2004). "Evaluation of structural best management practices 20 years after installation: Black Creek watershed, Indiana." *Journal of Soil and Water Conservation*, 59(5), 191-196.

Chang, H. H. (2002). *Fluvial Processes in River Engineering*, Krieger Publishing Company, Malabar, Florida.

Ciach, G. J. (2003). "Local random errors in tipping-bucket rain gauge measurements." *Journal of Atmospheric and Oceanic Technology*, 20, 752-759.

Collins, A. L., Walling, D. E., and Leeks, G. J. L. (1998). "Use of composite fingerprints to determine the provenance of the contemporary suspended sediment load transported by rivers." *Earth Surface Processes and Landforms*, 23(1), 31-52.

Cutshall, N. H., Larsen, I. L., and Olsen, C. R. (1983). "Direct analysis of Pb-210 in sediment samples - self-absorptoin corrections." *Nuclear Instruments & Methods in Physics Research*, 206(1-2), 309-312.

Dibb, J. E. (1989). "Atmospheric deposition of beryllium 7 in the Chesapeak Bay region." *Journal of Geophysical Research*, 94(D2), 2261-2265.

Doomen, A. M. C., Wijma, E., Zwolsman, J. J. G., and Middelkoop, H. (2008). "Predicting suspended sediment concentrations in the Meuse River using a supply-based rating curve." *Hydrological Processes*, 22(12), 1846-1856.

Edwards, T. K., and Glysson, G. D. (1999). "Field methods for measurement of fluvial sediment." U. S. G. Survey, ed., Reston, Virginia.

Einstein, H. A. (1950). "The bed-load function for sediment transportation in open channel flows." S. C. S. United States Department of Agriculture, ed., Washington, D.C., 78.

Elhakeem, M., and Papanicolaou, A. N. (2009). "Estimation of the Runoff Curve Number via Direct Rainfall Simulator Measurements in the State of Iowa, USA." *Water Resources Management*, 23(12), 2455-2473.

Ellis, P. A. (2009). "Non-point source pollution in an agricultural watershed: uplands soil erosion and instream sediment transport," The University of Iowa, Iowa City, IA.

Fiener, P., and Auerswald, K. (2006). "Influence of scale and land use pattern on the efficacy of grassed waterways to control runoff." *Ecological Engineering*, 27(3), 208-218.

Flanagan, D. C., and Nearing, M. A. (1995). "Water Erosion Prediction Project: Hillslope profile and watershed model documentation - NSERL Report No. 10." U.-A. N. S. E. R. Laboratory, ed., West Lafayette, IN.

Fox, J. F., and Papanicolaou, A. N. (2008). "Application of the spatial distribution of nitrogen stable isotopes for sediment tracing at the watershed scale." *Journal of Hydrology*, 358(1-2), 46-55.

Ghadiri, H., Rose, C. W., and Hogarth, W. L. (2001). "The influence of grass and porous barrier strips on runoff hydrology and sediment transport." *Transactions of the Asae*, 44(2), 259-268.

Gibbs, R. J. (1985). "Settling velocity, diameter, and density for flocs of illite, kaolinite, and montmorillonite." *Journal of Sedimentary Petrology*, 55(1), 65-68.

Global Water Instrumentation, I. (2009). "WL16 Water Level Loggers." Gold River, CA.

Gray, J. R. (2003). "Proceedings of the federal interagency sediment monitoring instrument and analysis research workshop." *Federal interagency sediment monitoring instrument and analysis research workshop*, Flagstaff, AZ.

Gray, J. R., and Gartner, J. W. (2009). "Technological advances in suspended-sediment surrogate monitoring." *Water Resources Research*, 45.

Green, T. R., Beavis, S. G., Dietrich, C. R., and Jakeman, A. J. (1999). "Relating stream-bank erosion to in-stream transport of suspended sediment." *Hydrological Processes*, 13(5), 777-787.

He, Q., and Walling, D. E. (1996). "Interpreting particle size effects in the adsorption of Cs-137 and unsupported Pb-210 by mineral soils and sediments." *Journal of Environmental Radioactivity*, 30(2), 117-137.

Huang, C., Wells, L. K., and Norton, L. D. (1999). "Sediment transport capacity and erosion processes: Model concepts and reality." *Earth Surface Processes and Landforms*, 24(6), 503-516.

Ioannidou, A., and Papastefanou, C. (2006). "Precipitation scavenging of Be-7 and (CS)-C-137 radionuclides in air." *Journal of Environmental Radioactivity*, 85(1), 121-136.

Julian, J. P., and Torres, R. (2006). "Hydraulic erosion of cohesive riverbanks." *Geomorphology*, 76(1-2), 193-206.

Kennedy, E. J. (1984). "Discharge ratings at gauging stations." U. S. G. Survey, ed., United States Government Printing Office, Washington, D.C., 59.

Klein, M. (1984). "Anti clockwise hysteresis in suspended sediment concentration during individual storms - Holbeck Catchment - Yorkshire, England." *Catena*, 11(2-3), 251-257.

Kuhnle, R. A., Bingner, R. L., Alonso, C. V., Wilson, C. G., and Simon, A. (2008). "Conservation practice effects on sediment load in the Goodwin Creek Experimental Watershed." *Journal of Soil and Water Conservation*, 63(6), 496-503.

Lane, S. N., Richards, K. S., and Chandler, J. H. (1995). "Morphological estimation of the time-integrated bed-load transport rate." *Water Resources Research*, 31(3), 761-772.

Lefrancois, J., Grimaldi, C., Gascuel-Odoux, C., and Gilliet, N. (2007). "Suspended sediment and discharge relationships to identify bank degradation as a main sediment source on small agricultural catchments." *Hydrological Processes*, 21(21), 2923-2933.

Leithold, E. L., and Blair, N. E. (2001). "Watershed control on the carbon loading of marine sedimentary particles." *Geochimica Et Cosmochimica Acta*, 65(14), 2231-2240.

Lenzi, M. A., Mao, L., and Comiti, F. (2003). "Interannual variation of suspended sediment load and sediment yield in an alpine catchment." *Hydrological Sciences Journal-Journal Des Sciences Hydrologiques*, 48(6), 899-915.

Lenzi, M. A., and Marchi, L. (2000). "Suspended sediment load during floods in a small stream of the Dolomites (northeastern Italy)." *Catena*, 39(4), 267-282.

Lindorm. (2009a). "SediMeter." Miami Springs, FL.

Lindorm. (2009b). "SediMeter User Reference Manual." 42.

Mabit, L., Benmansour, M., and Walling, D. E. (2008). "Comparative advantages and limitations of the fallout radionuclides Cs-137, Pb-210, and Be-7 for assessing soil erosion and sedimentation." *Journal of Environmental Radioactivity*, 99, 1799-1807.

Mabit, L., Bernard, C., Laverdiere, M. R., and Wicherek, S. (1999). "Assessment of soil erosion in a small agricultural basin of the St. Lawrence River watershed." *Hydrobiologia*, 410, 263-268.

Mano, V., Nemery, J., Belleudy, P., and Poirel, A. (2009). "Assessment of suspended sediment transport in four alpine watersheds (France): influence of the climatic regime." *Hydrological Processes*, 23(5), 777-792.

Markus, M., and Demissie, M. (2006). "Predictability of annual sediment loads based on flood events." *Journal of Hydrologic Engineering*, 11(4), 354-361.

Martz, L. W., and Dejong, E. (1991). "Using cesium-137 and landform classification to develop a net soil-erosion budget for a small Canadian prairie watershed." *Catena*, 18(3-4), 289-308.

Matisoff, G., Wilson, C. G., and Whiting, P. J. (2005). "The Be-7/Pb-210(xs) ratio as an indicator of suspended sediment age or fraction new sediment in suspension." *Earth Surface Processes and Landforms*, 30(9), 1191-1201.

Nearing, M. A., Foster, G. R., Lane, L. J., and Finkner, S. C. (1989). "A process-based soil-erosion model for USDA-Water Erosion Prediction Project technology." *Transactions of the Asae*, 32(5), 1587-1593.

NRCS, U. (2003). "National Resources Inventory: 2003 Annual NRI." N. R. C. S. United States Department of Agriculture, ed., 24.

Nyssen, J., Clymans, W., Poesen, J., Vandecasteele, I., De Raets, S., Haregeweyn, N., Naudts, J., Hadera, A., Moeyersons, J., Haile, M., and Deckers, J. (2009). "How soil conservation affects the catchment sediment budget - a comprehensive study in the north Ethiopian highlands." *Earth Surface Processes and Landforms*, 34(9), 1216-1233.

Olley, J., and Caitcheon, G. (2000). "Major element chemistry of sediments from the Darling-Barwon River and its tributaries: implications for sediment and phosphorus sources." *Hydrological Processes*, 14(7), 1159-1175.

Olsen, C. R., Larsen, I. L., Lowry, P. D., Cutshall, N. H., and Nichols, M. M. (1986). "Geochemistry and deposition of Be-7 in river-estuarine and coastal waters." *Journal of Geophysical Research*, 91(C1), 896-908.

Ortega, J. A., and Heydt, G. G. (2009). "Geomorphological and sedimentological analysis of flash-flood deposits: The case of the 1997 Rivillas flood (Spain)." *Geomorphology*, 112, 1-14.

Owens, P. N., Walling, D. E., and He, Q. P. (1996). "The behaviour of bomb-derived caesium-137 fallout in catchment soils." *Journal of Environmental Radioactivity*, 32(3), 169-191.

Papanicolaou, A. N., Elhakeem, M., and Hilldale, R. (2007). "Secondary current effects on cohesive river bank erosion." *Water Resources Research*, 43(12).

Papanicolaou, A. N., Fox, J. F., and Marshall, J. (2003). "Soil fingerprinting in the Palouse Basin, USA using stable carbon and nitrogen isotopes." *International Journal of Sediment Research*, 18(2), 278-284.

Pimentel, D., Harvey, C., Resosudarmo, P., Sinclair, K., Kurz, D., McNair, M., Crist, S., Shpritz, L., Fitton, L., Saffouri, R., and Blair, R. (1995). "Environmental and Economic Costs of Soil Erosion and Conservation Benefits." *Science*, 267(5201), 1117-1123.

Polyakov, V. O., Nearing, M. A., and Shipitalo, M. J. (2004). "Tracking sediment redistribution in a small watershed: Implications for agro-landscape evolution." *Earth Surface Processes and Landforms*, 29(10), 1275-1291.

Poulenard, J., Perrette, Y., Fanget, B., Quetin, P., Trevisan, D., and Dorioz, J. M. (2009). "Infrared spectroscopy tracing of sediment sources in a small rural watershed (French Alps)." *Science of the Total Environment*, 407(8), 2808-2819.

Pruitt, B. A. (2003). "Uses of turbidity by states and tribes." *Federal Interagency Workshop on Turbidity and other Sediment Surrogates*, Reno, NV, 31-46.

Rayburn, A. P., and Schulte, L. A. (2006). "Clear Creek Watershed: 150 years of landscape change." Iowa State University, Ames, IA.

Ridd, P., and Larcombe, P. (1994). "Biofouling control for optical backscatter suspended sediment sensors." *Marine Geology*, 116(3-4), 255-258.

Ruhe, R. V. (1956). "Geomorphic surfaces and the nature of soils." *Soil Science*, 82, 441-445.

Salant, N. L., Hassan, M. A., and Alonso, C. V. (2008). "Suspended sediment dynamics at high and low storm flows in two small watersheds." *Hydrological Processes*, 22(11), 1573-1587.

Seeger, M., Errea, M. P., Begueria, S., Arnaez, J., Marti, C., and Garcia-Ruiz, J. M. (2004). "Catchment soil moisture and rainfall characteristics as determinant factors for discharge/suspended sediment hysteretic loops in a small headwater catchment in the Spanish pyrenees." *Journal of Hydrology*, 288(3-4), 299-311.

Simon, A., and Rinaldi, M. (2006). "Disturbance, stream incision, and channel evolution: The roles of excess transport capacity and boundary materials in controlling channel response." *Geomorphology*, 79(3-4), 361-383.

Smith, B. P. G., Naden, P. S., Leeks, G. J. L., and Wass, P. D. (2003). "The influence of storm events on fine sediment transport, erosion and deposition within a reach of the River Swale, Yorkshire, UK." 451-474.

Smith, H. G., and Dragovich, D. (2009). "Interpreting sediment delivery processes using suspended sediment-discharge hysteresis patterns from nested upland catchments, south-eastern Australia." *Hydrological Processes*, 23(17), 2415-2426.

Soil Conservation Service (1972). "National Engineering Handbook." United States Department of Agriculture, Washington, D.C.

Soulsby, C., Petry, J., Brewer, M. J., Dunn, S. M., Ott, B., and Malcolm, I. A. (2003). "Identifying and assessing uncertainty in hydrological pathways: a novel approach to end member mixing in a Scottish agricultural catchment." *Journal of Hydrology*, 274(1-4), 109-128.

Springer, F. M. J., Ullrich, C. R., and hagerty, D. J. (1985). "Streambank stability." *Journal of Geotechnical Engineering*, 111(5), 624-640.

Steegen, A., Govers, G., Nachtergaele, J., Takken, I., Beuselinck, L., and Poesen, J. (2000). "Sediment export by water from an agricultural catchment in the Loam Belt of central Belgium." *Geomorphology*, 33(1-2), 25-36.

Stubblefield, A. P., Reuter, J. E., and Goldman, C. R. (2009). "Sediment budget for subalpine watersheds, Lake Tahoe, California, USA." *Catena*, 76(3), 163-172.

Stutter, M. I., Langan, S. J., and Cooper, R. J. (2008). "Spatial contributions of diffuse inputs and within-channel processes to the form of stream water phosphorus over storm events." *Journal of Hydrology*, 350(3-4), 203-214.

Taylor, J. R. (1997). *An introduction to error analysis: the study of uncertainties in physical measurements*, University Science Books, Sausalito, CA.

Thorne, C. R. (1982). "Processes and mechanisms of river bank erosion." Gravel-bed Rivers, R. D. Hey and J. C. T. Bathurst, C.R., eds., John Wiley & Sons, Chichester, 227-271.

Todd, J. F., Wong, G. T. F., Olsen, C. R., and Larsen, I. L. (1989). "Atmospheric depositional characteristics of Beryllium-7 and Lead-210 along the southeastern Virginia coast." *Journal of Geophysical Research*, 94(D8), 11106-11116.

Valero-Garces, B. L., Navas, A., Machin, J., and Walling, D. (1999). "Sediment sources and siltation in mountain reservoirs: a case study from the Central Spanish Pyrenees." *Geomorphology*, 28(1-2), 23-41.

van der Perk, M., and Jetten, V. G. (2006). "The use of a simple sediment budget model to estimate long-term contaminant export from small catchments." 3-12.

Vandaele, K., and Poesen, J. (1995). "Spatial and temporal patterns of soil-erosion rates in an agricultural catchment, central Belgium." *Catena*, 25(1-4), 213-226.

Vanden Bygaart, A. J., and Protz, R. (2001). "Bomb-fallout Cs-137 as a marker of geomorphic stability in dune sands and soils, Pinery Provincial Park, Ontario, Canada." *Earth Surface Processes and Landforms*, 26(6), 689-700.

Visser, F., Roth, C. H., Wasson, R., and Govers, G. (2007). "A sediment budget for a cultivated floodplain in tropical North Queensland, Australia." *Earth Surface Processes and Landforms*, 32, 1475-1490.

Wallbrink, P. J., and Murray, A. S. (1993). "Use of fallout radionuclides as indicators of erosion processes." *Hydrological Processes*, 7(3), 297-304.

Wallbrink, P. J., and Murray, A. S. (1994). "Fallout of Be-7 in south eastern Australia." *Journal of Environmental Radioactivity*, 25(3), 213-228.

Wallbrink, P. J., and Murray, A. S. (1996). "Distribution and variability of Be-7 in soils under different surface cover conditions and its potential for describing soil redistribution processes." *Water Resources Research*, 32(2), 467-476.

Wallbrink, P. J., Murray, A. S., and Olley, J. M. (1999). "Relating suspended sediment to its original soil depth using fallout radionuclides." *Soil Science Society of America Journal*, 63(2), 369-378.

Walling, D. E., and Amos, C. M. (1999). "Source, storage and mobilisation of fine sediment in a chalk stream system." *Hydrological Processes*, 13(3), 323-340.

Walling, D. E., He, Q., and Blake, W. (1999). "Use of Be-7 and Cs-137 measurements to document short- and medium-term rates of water-induced soil erosion on agricultural land." *Water Resources Research*, 35(12), 3865-3874.

Walling, D. E., Russell, M. A., Hodgkinson, R. A., and Zhang, Y. (2002). "Establishing sediment budgets for two small lowland agricultural catchments in the UK." *Catena*, 47(4), 323-353.

Wasson, R. J., Caitcheon, G., Murray, A. S., McCulloch, M., and Quade, J. (2002). "Sourcing sediment using multiple tracers in the catchment of Lake Argyle, Northwestern Australia." *Environmental Management*, 29(5), 634-646.

Williams, G. P. (1989). "Sediment concentration versus water discharge during single hydrologic events in rivers." *Journal of Hydrology*, 111(1-4), 89-106.

Wilson, C. G., and Kuhnle, R. A. (2006). "Determining relative contributions of eroded landscape sediment to the suspended load of Goodwin Creek using Be-7 and Pb-210." United States Department of Agriculture, Agricultural Research Service.

Wilson, C. G., Kuhnle, R. A., Bosch, D. D., Steiner, J. L., Starks, P. J., Tomer, M. D., and Wilson, G. V. (2008). "Quantifying relative contributions from sediment sources in Conservation Effects Assessment Project watersheds." *Journal of Soil and Water Conservation*, 63(6), 523-532.

Wilson, C. G., Matisoff, G., and Whiting, P. J. (2003). "Short-term erosion rates from a Be-7 inventory balance." *Earth Surface Processes and Landforms*, 28(9), 967-977.

Winterwerp, J. C. (2001). "Stratification effects by cohesive and noncohesive sediment." *Journal of Geophysical Research-Oceans*, 106(C10), 22559-22574.

Yang, M. Y., Walling, D. E., Tian, J. L., and Liu, P. L. (2006). "Partitioning the contributions of sheet and rill erosion using beryllium-7 and cesium-137." *Soil Science Society of America Journal*, 70(5), 1579-1590.

Zager, M. (2009). "Establishing a suspended sediment rating curve for Clear Creek." The University of Iowa, Iowa City, IA, 13.